

# High-purity Oxygen Production using Silver-exchanged Titanosilicates (Ag-ETS-10)

by

Sayed Alireza Hosseinzadeh Hejazi

A thesis submitted in partial fulfillment of the requirements for the degree of

Doctor of Philosophy

in

CHEMICAL ENGINEERING

Department of Chemical and Materials Engineering

University of Alberta

© Sayed Alireza Hosseinzadeh Hejazi, 2017

# Abstract

High-purity oxygen above 99.0% is required in many medical and industrial applications such as the pharmaceutical and aerospace applications. Due to the similar physical properties of oxygen and argon, this separation is very challenging. Adsorption separation techniques are more preferable to conventional cryogenic distillation of O<sub>2</sub>/Ar for small and medium scale applications as they offer more favorable process economics. However, very few commercial adsorbents offer the ability to separate O<sub>2</sub> and Ar. Silver-exchanged titanosilicates (Ag-ETS-10) have shown the potential to separate these gases based on their thermodynamic affinities. This opens up the possibility of developing processes for high purity O<sub>2</sub> separations. In the second chapter of this study, adsorption isotherms of O<sub>2</sub>, Ar, and N<sub>2</sub> on Ag-ETS-10 extrudates were measured using the volumetric technique and described using a Langmuir isotherm. The large-scale performance of the adsorbent was verified by measuring single, binary, and ternary breakthrough profiles using a laboratory scale dynamic column breakthrough apparatus which was designed and constructed as a part of this study. These profiles were modeled by writing mass and energy balances that were discretized in space and solved in MATLAB using the finite volume technique. The model could predict the experimental profiles to a high level of precision. In the third chapter, a detailed study on the mass transfer dynamics of oxygen separation using Ag-ETS-10 was conducted. The effect of flow rate, temperature, pressure, and particle size on the breakthrough profiles of N<sub>2</sub>, O<sub>2</sub>, and Ar was studied. Influence of different mass transfer resistances and hydrodynamics of the separation were investigated based on these experimental results using fundamentals of mass transfer which confirmed the fast mass transfer nature of Ag-ETS-10.

In the fourth chapter, various vacuum swing adsorption (VSA) cycle configurations including the simple Skarstrom cycle and more complicated 6-step VSA cycles were simu-

lated using mathematical models. A mixture of 95.0%/5.0% O<sub>2</sub>/Ar was considered in the simulations and a rigorous multi-objective optimization was conducted to maximize O<sub>2</sub> purity and recovery. The simulations predicted 27.3% recovery for a product with 99.5% purity for a 6-step cycle with pressure equalization (PE) and light product pressurization (LPP) steps. The recovery for the same level of purity was improved significantly to 91.7% by implementing a heavy product pressurization (HPP) step. The effect of bed length on O<sub>2</sub> purity and recovery and the comparison of VSA with pressure swing adsorption (PSA) and pressure-vacuum swing adsorption (PVSA) for high-purity O<sub>2</sub> production were also presented. Rigorous multi-objective optimizations were conducted to maximize oxygen productivity and minimize energy consumption of the VSA cycles, while meeting different purity constraints, and significant improvement in the performance indicators was obtained through process optimization. In Chapters 4 and 5, the simple 3-step and Skarstrom cycle experiments with 95.0%/5.0% O<sub>2</sub>/Ar and dry air as the feed were performed. In order to verify the cycle simulations, values of experimental purity and recovery at cyclic steady state, transitional concentration and axial temperature profiles were compared with the modeling predictions. Moreover, in the fifth chapter, the cycles discussed in Chapter 4 were further explored by comparing single-stage and dual-stage VSA processes in terms of total energy consumption and O<sub>2</sub> productivity of the whole process including the N<sub>2</sub> removal stage. The simulations predicted 82.0% recovery for a product with 99.5% purity for a 6-step cycle with PE and HPP and dry air feed stream. The effect of bed length and nitrogen content in the feed on the performance indicators was also studied. Operating conditions for various cycle configurations were optimized through non-dominated sorting genetic algorithm technique to achieve lower total energy consumption and higher overall productivity and the Pareto fronts were compared against each other in order to choose the best possible design. The results indicated that the single-stage 6-step cycle with PE and HPP presents a better performance compared to the other single-stage and dual-stage approaches. A simple graphical scheduling study was also conducted in order to calculate the number of columns required for a continuous process using the better performing configurations.

# Preface

Some of the research conducted for this thesis forms part of an international research collaboration, led by Professor Steven Kuznicki at the University of Alberta, namely Helmholtz-Alberta initiative (HAI). The research conducted in this thesis was funded by NSERC (Industrial Research Chair in Molecular Sieve Nanomaterials, Discovery Grant RGPIN-2014-06164).

The technical apparatus referred to in chapter 2-5 was designed and constructed by the thesis author (Sayed Alireza Hosseinzadeh Hejazi) with the assistance of J. Sawada. The data acquisition hardware and software of the apparatus was built by the Instrument shop at the Department of Chemical and Materials Engineering, University of Alberta. The material used in this study was synthesized by Lan Wu and Tong Qiu at the University of Alberta. J. Sawada at the University of Alberta assisted in the isotherm measurements. This thesis is written on a paper-based format and there might be some minor overlaps between the chapters.

Chapter 2 of this thesis has been published as S. A. Hosseinzadeh Hejazi, A. Rajendran, J. A. Sawada, and S. M. Kuznicki, “Dynamic Column Breakthrough and Process Studies of High-Purity Oxygen Production Using Silver-Exchanged Titanosilicates”, *Industrial and Engineering Chemistry Research*, vol. 55, issue 20, 5993-6005. In this paper, Sayed Alireza Hosseinzadeh Hejazi was responsible for data collection and analysis as well as the manuscript composition. He was also responsible for the design of experiments and optimization runs. J. Sawada assisted in the isotherm measurements. A. Rajendran and S. M. Kuznicki were the supervisory authors and were involved with concept formation and manuscript composition.

Chapter 3 of this thesis will be submitted for publication as S. A. Hosseinzadeh Hejazi, L. Estupinan Perez, R. Teruo Maruyama, A. Rajendran, and S. M. Kuznicki, “Understanding the Dynamics of High Purity Oxygen Separation using Silver Exchanged Titanosilicates (Ag-ETS-10)”, to *Adsorption* journal. In this paper, Sayed Alireza Hosseinzadeh Hejazi was responsible for data collection and analysis as well as the manuscript composition. He

was also responsible for the design of experiments. L. Estupinan Perez assisted in writing the introduction. R. Teruo Maruyama, an undergraduate student, and L. Estupinan Perez assisted in conducting some of the experiments in this paper. A. Rajendran and S. M. Kuznicki were the supervisory authors and were involved with concept formation and manuscript composition.

Chapter 4 of this thesis has been submitted for publication as S. A. Hosseinzadeh Hejazi, L. Estupinan Perez, A. Rajendran, and S. M. Kuznicki, "Cycle Development and Process Optimization of High-purity Oxygen Production using Silver-Exchanged Titanosilicates (Ag-ETS-10)", to Industrial and Engineering Chemistry Research. In this paper, Sayed Alireza Hosseinzadeh Hejazi was responsible for data collection and analysis as well as the manuscript composition. He was also responsible for the design of experiments and optimization runs. L. Estupinan Perez assisted in conducting some of the experiments. A. Rajendran and S. M. Kuznicki were the supervisory authors and were involved with concept formation and manuscript composition.

Chapter 5 of this thesis will be submitted for publication as S. A. Hosseinzadeh Hejazi, K. N. Pai, L. Estupinan Perez, A. Rajendran, and S. M. Kuznicki, "Single-stage and Dual-stage High-purity Oxygen Production using Silver-Exchanged Titanosilicates (Ag-ETS-10)", to Industrial and Engineering Chemistry Research. In this paper, Sayed Alireza Hosseinzadeh Hejazi was responsible for data collection and analysis as well as the manuscript composition. He was also responsible for the design of experiments and optimization runs. K. N. Pai assisted in cycle scheduling analysis. L. Estupinan Perez assisted in conducting the experiments in this paper. A. Rajendran and S. M. Kuznicki were the supervisory authors and were involved with concept formation and manuscript composition.

To my wife, Shirin  
for her love and patience

# Acknowledgements

“Silence is the language of God, all else is poor translation.”

—Rumi

I would like to express my sincere gratitude to my supervisors, Prof. Steven Kuznicki and Dr. Arvind Rajendran, for their guidance, generous support and great encouragement during my studies. This dissertation would not have been possible without their kind attention and patience. I will never forget September 30th, 2009 when Prof. Kuznicki accepted me as a masters student and later giving me the opportunity to continue as a Ph.D. Student. I am grateful to have Arvind as my co-supervisor since January 2013. I acknowledge his great guidance and the hundreds of hours he has devoted to my research. I am very grateful for his insight, advice and valuable discussions. I learned a lot of things, not only about science, but also about professional life from him.

I would also like to thank my examining committee, Dr. Ronny Pini, Dr. Zaher Hashisho and Dr. Hongbo Zeng for their invaluable comments and suggestions. It is also my pleasure to thank Libardo, Ashwin, Nagesh, Nick, Gokul, Jim, Adolfo, Tanya, An, Lan, and all the current and past members of our research group for their valuable support.

My sincere gratitude goes to Libardo for his friendship and support over the past 4 years. He is a great friend and I will never forget the non-academic discussions we had. I would like to also thank my great friends in Edmonton, Mohammadhosein and Ashwin for their support and friendship over the past years. I place on record, my sincere gratitude to the Tasnim Society which I had the privilege of serving as the executive committee for five years.

I would like to express my deepest gratitude to my family: My parents, Naser and Zohreh, and my brother, Mohammadreza. Although I lost my father almost twelve years ago, I would never forget him and his memories will stay with me forever. I am indebted to my mother for her patience, blessings and love. She is the hero of my life. I would like to also thank my parents-in-law, Ali and Maryam, for their kind support.

My sincere gratitude goes to our little boy Sadra, who brought happiness, love, and encouragement to our family with his birth in August 2015. Finally, and most importantly,

I would like to thank my beloved wife, Shirin. Her support, patience, and priceless love over the past five years have undeniably paved the way during the time of my studies. Therefore, this thesis is dedicated with love and respect to her.

Financial support from the Helmholtz-Alberta initiative (HAI) and NSERC for their sponsorship of the industrial research chair in molecular sieve nanomaterials are also gratefully acknowledged.

# Contents

<b>1</b>	<b>Introduction</b>	<b>1</b>
1.1	Air separation . . . . .	2
1.1.1	Cryogenic distillation . . . . .	2
1.1.2	Membrane-based separation . . . . .	3
1.1.3	Adsorption-based separation . . . . .	3
1.1.4	Choice of adsorbent . . . . .	4
1.1.5	Cycles for oxygen purification . . . . .	5
1.1.6	Thermodynamics and kinetics of adsorption . . . . .	6
1.1.7	Pressure swing adsorption (PSA) . . . . .	8
1.1.8	Modeling and simulation of adsorption . . . . .	10
1.1.9	Optimization of adsorption processes . . . . .	12
1.2	Challenges in high-purity oxygen production . . . . .	14
1.3	Objectives and structure of the thesis . . . . .	14
<b>2</b>	<b>Characterization of Ag-ETS-10</b>	<b>17</b>
2.1	Introduction . . . . .	18
2.2	Materials and methods . . . . .	19
2.2.1	Materials . . . . .	19
2.2.2	Isotherm measurements . . . . .	20
2.3	Dynamic column breakthrough experiments . . . . .	20
2.4	Modeling . . . . .	22
2.4.1	Modeling column dynamics . . . . .	22
2.4.2	Mass balance calculations . . . . .	25
2.5	Results and discussion . . . . .	26
2.5.1	Isotherm measurements . . . . .	26
2.5.2	Breakthrough measurements . . . . .	27
2.5.3	Single-component breakthrough measurements . . . . .	27
2.5.4	Binary breakthrough measurements . . . . .	29
2.5.5	Ternary breakthrough measurements . . . . .	33

2.6	Vacuum swing adsorption process for oxygen purification . . . . .	36
2.7	Conclusions . . . . .	40
<b>3</b>	<b>Dynamics of oxygen purification</b>	<b>41</b>
3.1	Introduction . . . . .	42
3.2	Materials and methods . . . . .	43
3.2.1	Materials . . . . .	43
3.2.2	Isotherm measurements . . . . .	43
3.2.3	Model . . . . .	45
3.3	Results and discussion . . . . .	45
3.3.1	Effect of flow rate . . . . .	45
3.3.2	Effect of temperature . . . . .	49
3.3.3	Effect of pressure . . . . .	52
3.3.4	Effect of particle size . . . . .	53
3.4	Conclusions . . . . .	54
<b>4</b>	<b>Cycle development and process optimization</b>	<b>56</b>
4.1	Introduction . . . . .	57
4.2	Materials and methods . . . . .	58
4.2.1	Materials . . . . .	58
4.2.2	Isotherm measurements . . . . .	58
4.2.3	Vacuum swing adsorption cycles . . . . .	59
4.2.4	Constituent steps . . . . .	60
4.2.5	Cycle optimization . . . . .	61
4.3	Results and discussion . . . . .	63
4.3.1	Experimental cycle demonstration . . . . .	63
4.3.2	Purity-Recovery optimization . . . . .	68
4.3.3	Energy-Productivity optimization . . . . .	75
4.4	Conclusions . . . . .	78
<b>5</b>	<b>Optimal process design: single-stage vs. dual-stage</b>	<b>79</b>
5.1	Introduction . . . . .	80
5.2	Materials and methods . . . . .	83
5.2.1	Materials . . . . .	83
5.2.2	Cycle configurations . . . . .	83
5.2.3	Cycle optimization . . . . .	84
5.3	Results and discussion . . . . .	84
5.3.1	Single-stage production of high-purity oxygen . . . . .	84

5.3.2	Dual-stage production of high-purity oxygen . . . . .	91
5.3.3	Cycle scheduling . . . . .	97
5.4	Conclusions . . . . .	100
<b>6</b>	<b>Concluding remarks</b>	<b>101</b>
6.1	Conclusions . . . . .	101
6.2	Outlook . . . . .	104
	<b>Bibliography</b>	<b>106</b>

# List of Figures

- 1.1 Pressure dependency of adsorption explored in pressure swing adsorption processes.  $\Delta q$  represent working capacity between the adsorption and desorption pressures,  $P_{\text{Ads}}$  and  $P_{\text{Des}}$ , respectively.
- 1.2 Schematic representation of a basic 3-step PSA cycle.
- 1.3 Typical work-flow of the PSA optimization routine in this study.
  
- 2.1 Schematic diagram of dynamic-column breakthrough apparatus. Picture at the bottom shows Ag-ETS-10 extrudates along with a ruler (units in cm)
- 2.2 Single component adsorption isotherms of a)N<sub>2</sub>, b)Ar, and c)O<sub>2</sub> on Ag-ETS-10 extrudates. Symbols are experimental values and lines are fitted Langmuir model. (d) compares the isotherms of three gases at 303.15 K. Closed symbols in (d) are experimental loadings calculated from breakthrough experiments.
- 2.3 Adsorption breakthrough profiles for N<sub>2</sub>, Ar, 95% O<sub>2</sub>/5% Ar using He as the purge gas. Figure (a) shows breakthrough profiles measured at the column outlet; (b) shows corresponding temperature profiles measured by thermocouples 1 and 2 ( $T_1$  and  $T_2$ ). Symbols and lines correspond to experimental and simulation data, respectively. Experimental conditions:  $P_{\text{avg}}=95$  kPa,  $T_{\text{bath}}=303.15$  K,  $F_{\text{in}}=150$  ccm.
- 2.4 Breakthrough profiles with various compositions of O<sub>2</sub>/Ar mixture using He as the purge gas. Profiles on the left column depict adsorption experiments while those on the right depict desorption experiments. Figures (a) and (b) show O<sub>2</sub> profiles at the column outlet; (c) and (d) show corresponding Ar profiles; (e) and (f) show the temperature profile measured by thermocouple 2 ( $T_2$ ). Symbols and lines correspond to experimental and simulation data, respectively. Experimental conditions:  $P_{\text{avg}}=95$  kPa,  $T_{\text{bath}}=303.15$  K,  $F_{\text{in}}=150$  ccm.

- 2.5 Binary O<sub>2</sub>/Ar loading at 95 kPa and 303.15 K. Symbols are experimental data while lines are the calculated values using the extended Langmuir model.
- 2.6 Breakthrough profiles for 95% O<sub>2</sub>/5% Ar using Ar and He as the purge gases. Profiles on the left column depict adsorption experiments while those on the right depict desorption experiments. Figures (a) and (b) show O<sub>2</sub> profiles at the column outlet; (c) and (d) show corresponding temperature profiles measured by thermocouples 1 and 2 ( $T_1$  and  $T_2$ ). Symbols and lines correspond to experimental and simulation data, respectively. Experimental conditions:  $P_{\text{avg}}=95$  kPa,  $T_{\text{bath}}=303.15$  K,  $F_{\text{in}}=150$  ccm.
- 2.7 Breakthrough profiles for N<sub>2</sub> using 95% O<sub>2</sub>/5% Ar as the purge gas. Profiles on the left column depict adsorption experiments while those on the right depict desorption experiments. Figures (a) and (b) show component profiles at the column outlet; (c) and (d) show corresponding temperature profiles measured by thermocouples 1 and 2 ( $T_1$  and  $T_2$ ). Symbols and lines correspond to experimental and simulation data, respectively. Experimental conditions:  $P_{\text{avg}}=95$  kPa,  $T_{\text{bath}}=303.15$  K,  $F_{\text{in}}=150$  ccm.
- 2.8 Breakthrough profiles for Air using He as the purge gas. Profiles on the left column depict adsorption experiments while those on the right depict desorption experiments. Figures (a) and (b) show component profiles at the column outlet; (c) and (d) show corresponding temperature profiles measured by thermocouples 1 and 2 ( $T_1$  and  $T_2$ ). Symbols and lines correspond to experimental and simulation data, respectively. Experimental conditions:  $P_{\text{avg}}=95$  kPa,  $T_{\text{bath}}=303.15$  K,  $F_{\text{in}}=150$  ccm.
- 2.9 Cycle configuration and pressure profiles used in this study. The operating parameters shown are the ones used for the base case simulation.
- 2.10 Effect of  $P_L$  on: (a) purity and recovery of O<sub>2</sub>; (b) O<sub>2</sub> gas phase axial profiles of the Adsorption step; (c) Ar solid phase axial profiles of the Adsorption (solid line) and Pressurization (dashed line) steps in Skarstrom cycle.
- 2.11 Results of process optimization to maximize O<sub>2</sub> purity and recovery. (a) Pareto curve for the optimization of O<sub>2</sub> purity and recovery in the Skarstrom VSA cycle; (b) Variation of purity as a function of  $\frac{t_{\text{LR}}}{t_{\text{ADS}}}$  for the Pareto points.

- 3.1 Single component high pressure adsorption isotherms of a)N<sub>2</sub>, b)Ar, and c)O<sub>2</sub> on Ag-ETS-10 extrudates. Symbols are experimental values and lines are fitted dual site Langmuir model. (d) compares the isotherms of three gases at 303.15 K.
- 3.2 Effect of inlet flow rate on the breakthrough profiles for Ar and 50.0% O<sub>2</sub>/50.0% Ar. Figures (a) and (b) show concentration profiles at the column outlet; (c) and (d) show corresponding 1st derivative of the concentration profiles; (e) and (f) show corresponding temperature profiles measured by thermocouple 2 ( $T_2$ ). Symbols and lines correspond to experimental and simulation data, respectively. Experimental conditions:  $P_{\text{avg}}=95$  kPa,  $T_{\text{bath}}=303.15$  K.
- 3.3 Effect of inlet flow rate on the desorption profiles for Ar and 50.0% O<sub>2</sub>/50.0% Ar. Figures (a) and (b) show concentration profiles at the column outlet; (c) and (d) show corresponding temperature profiles measured by thermocouple 2 ( $T_2$ ). Symbols and lines correspond to experimental and simulation data, respectively. Experimental conditions:  $P_{\text{avg}}=95$  kPa,  $T_{\text{bath}}=303.15$  K.
- 3.4 Effect of temperature on the breakthrough profiles for N<sub>2</sub>, Ar and 95.0% O<sub>2</sub>/5.0% Ar. Figures (a), (b), and (c) show concentration profiles at the column outlet; (d), (e), and (f) show corresponding 1st derivative of the concentration profiles; (g), (h), and (i) show corresponding temperature profiles measured by thermocouple 2 ( $T_2$ ). Symbols and lines correspond to experimental and simulation data, respectively. Experimental conditions:  $P_{\text{avg}}=95$  kPa,  $F_{\text{in}}=150$  ccm.
- 3.5 Effect of temperature on the Desorption profiles for N<sub>2</sub>, Ar and 95.0% O<sub>2</sub>/5.0% Ar. Figures (a), (b), and (c) show concentration profiles at the column outlet; (d), (s), and (f) show corresponding temperature profiles measured by thermocouple 2 ( $T_2$ ). Symbols and lines correspond to experimental and simulation data, respectively. Experimental conditions:  $P_{\text{avg}}=95$  kPa,  $F_{\text{in}}=150$  ccm.
- 3.6 Effect of pressure on the breakthrough profiles for N<sub>2</sub>. (a) Concentration profile at the column outlet; (b) Corresponding 1st derivative of the concentration profile. Symbols and lines correspond to experimental and simulation data, respectively. Experimental conditions:  $T_{\text{bath}}=303.15$  K,  $F_{\text{in}}=150$  ccm.

- 3.7 Effect of particle size on the breakthrough profiles for  $N_2$ . (a) Concentration profile at the column outlet; (b) Corresponding 1st derivative of the concentration profile. Symbols and lines correspond to experimental and simulation data, respectively. Experimental conditions:  $P_{avg}=95$  kPa,  $T_{bath}=303.15$  K,  $F_{in}=150$  ccm.
- 4.1 Cycle configuration and pressure profiles of the adsorption cycles: (a) Skarstrom (b) 6-step with PE and LPP (c) 6-step with PE and HPP.
- 4.2 Schematic diagram of experimental VSA apparatus.
- 4.3 Comparison of experimental and simulated pressure profile experiment B. Operating conditions are provided in Table 3. Symbols are experimental values and lines correspond to simulation.
- 4.4 Comparison of experiments with model calculations for experiment C. Operating conditions are provided in Table 4.1. Symbols are experimental values and lines correspond to simulation. (a) Transient product purity during the adsorption steps; (b) Axial temperature profile for thermocouple located at 8 cm from the column inlet; (c) Transient product purity during the adsorption step with focus on high-purity range; (d) Axial temperature profile for thermocouple located at 8 cm from the column inlet for one cycle at cyclic steady state; (e) Experimental and simulated pressure profile.
- 4.5 Results of process optimization to maximize  $O_2$  purity and recovery for 95.0%  $O_2$  5.0% Ar as the feed using the Skarstrom cycle. (a) Comparison of Pareto curves for the optimization of  $O_2$  purity and recovery with fixed and variable bed lengths; (b) Variation of recovery as a function of bed utilization factor for the Pareto points.
- 4.6 Effect of bed length on axial concentration profiles and performance indicators.  $L = 1.12$  m was chosen by the optimizer for the variable bed length optimizations. (a)  $O_2$  gas phase axial concentration profiles at the end of the adsorption step; (b) Ar solid phase axial concentration profiles at the end of the adsorption step; (c)  $O_2$  purity and recovery as a function of  $L$  for a fixed BUF=1.7 and  $t_{ADS}=9.8$  s.
- 4.7 Comparison of PSA, VSA, and PVSA Skarstrom cycles for high-purity  $O_2$  production from 95.0%  $O_2$  5.0% Ar feed. (a) Pareto curve for the optimization of  $O_2$  purity and recovery; (b) Variation of purity as a function of  $P_H$  for the PSA cycle Pareto points.

- 4.8 Results of process optimization to maximize O<sub>2</sub> purity and recovery for 95.0% O<sub>2</sub>/5.0% Ar as the feed. Experimental data and column dimension for the simulations are obtained from Ferreira et al [1].
- 4.9 Comparison of various cycles for high-purity O<sub>2</sub> production. (a) Results of process optimization to maximize O<sub>2</sub> purity and recovery for the Skarstrom, 6-step with PE and LPP, and 6-step with PE and HPP cycles; (b) Axial profiles of gas phase mole fraction for the adsorption, evacuation, and light reflux steps of the 6-step cycle with PE and LPP; (c) Axial profiles of gas phase mole fraction for the adsorption, evacuation, and heavy product pressurization steps of the 6-step cycle with PE and HPP.
- 4.10 Results of process optimization to maximize O<sub>2</sub> productivity and minimize energy consumption for 95.0% O<sub>2</sub>/5.0% Ar as the feed. (a) Skarstrom cycle; (b) 6-step with PE and LPP cycle; (c) 6-step with PE and HPP cycle; (d) comparison of all three cycles for a purity constraint of 99.5% O<sub>2</sub>.
- 5.1 Strategy of this study for high-purity O<sub>2</sub> production: (a) single-stage O<sub>2</sub> production. (b) Dual-stage O<sub>2</sub> production.
- 5.2 Skarstrom VSA cycle experiments. Symbols are experimental values and lines correspond to simulation. (a) transient product purity during the adsorption steps; (b) axial temperature profile for thermocouple located at 8 cm from the column inlet; (c) transient product purity during the adsorption steps with focus on high-purity range; (d) axial temperature profile for thermocouple located at 8 cm from the column inlet for one cycle at cyclic steady state; (e) Experimental and simulated pressure profile.
- 5.3 Results of process optimization to maximize O<sub>2</sub> purity and recovery for 6-step cycle with PE and HPP VSA and dry air feed.
- 5.4 Results of process optimization to maximize O<sub>2</sub> productivity and minimize energy consumption for dry air feed delivering 99.5% O<sub>2</sub> product. (a) first stage: Skarstrom cycle with zeolite 5A delivering product with different levels of N<sub>2</sub> content; (b) second stage: Skarstrom cycle with Ag-ETS-10 with different levels of N<sub>2</sub> content in the feed; (c) comparison of multiple dual-stage O<sub>2</sub> purification approaches with the single-stage Skarstrom. Volume of adsorbent in the productivity values for the dual-stage configurations is the cost normalized volume of Ag-ETS-10; (d) comparison of four possible cycle designs for O<sub>2</sub> purification.
- 5.5 Results of process optimization to maximize O<sub>2</sub> purity and recovery for Skarstrom VSA cycle with different N<sub>2</sub> content in the feed.

- 5.6 Effect of  $N_2$  content in the feed on the concentration profiles: (a) Normalized  $N_2$  gas phase axial concentration profiles of the Evacuation step (normalized against  $y_{N_2}$  in the feed); (b)  $O_2$  solid phase axial concentration profiles of the Evacuation step in the Skarstrom cycle.
- 5.7 Cycle scheduling for the optimal operating conditions. Idle times are shown in gray blocks: (a) single-stage Skarstrom cycle using Ag-ETS-10 for  $O_2$  purification. (b) single-stage 6-step cycle with PE and HPP using Ag-ETS-10 for  $O_2$  purification. The black blocks indicate the HPP step.
- 5.8 Cycle scheduling for the optimal operating conditions. Idle times are shown in gray blocks: (a) Skarstrom cycle using zeolite 5A for  $N_2$  removal (stage 1). (b) 6-step cycle with PE and LPP using Ag-ETS-10 for  $O_2$  purification (stage 2)(c) 6-step cycle with PE and HPP using Ag-ETS-10 for  $O_2$  purification (stage 2). The black blocks indicate the HPP step.

# List of Tables

- 1.1 Reported Henry's law selectivity of adsorbents showing Ar/O<sub>2</sub> selectivity.
- 1.2 Reported O<sub>2</sub>/Ar separation through P/VSA.
- 1.3 Some of the applications of PSA in the area of gas separation [2, 3].
  
- 2.1 Parameters used in cycle simulations and optimizations.
- 2.2 Fitted Langmuir adsorption parameters for N<sub>2</sub>, O<sub>2</sub>, and Ar on Ag-ETS-10.
- 2.3 Range of decision variables used in the Skarstrom cycle simulation.
  
- 3.1 Fitted dual-site Langmuir adsorption parameters for N<sub>2</sub>, O<sub>2</sub>, and Ar on Ag-ETS-10 at high pressure.
  
- 4.1 Comparison of model results and experimental measurements for processes with 95/5 (O<sub>2</sub>/Ar) as the feed.
- 4.2 Range of decision variables used in cycle optimizations.
  
- 5.1 Fitted Langmuir adsorption parameters for N<sub>2</sub> and O<sub>2</sub> on zeolite 5A.
- 5.2 Operating conditions for the experimental cycle demonstrations.
- 5.3 Range of decision variables used in VSA cycle purity-recovery and energy-productivity optimizations.
- 5.4 Equations used for the calculation of total energy consumption in the VSA cycles.

# Nomenclature

$b$	parameter in Langmuir isotherm [ $\text{m}^3 \text{mol}^{-1}$ ]
$b_0$	parameter in Langmuir isotherm [ $\text{m}^3 \text{mol}^{-1}$ ]
$c$	fluid phase concentration [ $\text{mol m}^{-3}$ ]
$C_{\text{pa}}$	specific heat capacity of the adsorbed phase [ $\text{J mol}^{-1} \text{K}^{-1}$ ]
$C_{\text{pg}}$	specific heat capacity of the gas phase [ $\text{J mol}^{-1} \text{K}^{-1}$ ]
$C_{\text{ps}}$	specific heat capacity of the adsorbent [ $\text{J kg}^{-1} \text{K}^{-1}$ ]
$C_{\text{pw}}$	specific heat capacity of the column wall [ $\text{J kg}^{-1} \text{K}^{-1}$ ]
$d$	parameter in dual-site Langmuir isotherm [ $\text{m}^3 \text{mol}^{-1}$ ]
$d_0$	parameter in dual-site Langmuir isotherm [ $\text{m}^3 \text{mol}^{-1}$ ]
$D_L$	axial dispersion [ $\text{m}^2 \text{s}^{-1}$ ]
$D_m$	molecular diffusivity [ $\text{m}^2 \text{s}^{-1}$ ]
$D_p$	macropore diffusivity [ $\text{m}^2 \text{s}^{-1}$ ]
$d_p$	particle diameter [m]
$F$	flow rate [ $\text{cc min}^{-1}$ ]
$h_{\text{in}}$	inside heat transfer coefficient [ $\text{J m}^{-2} \text{K}^{-1} \text{s}^{-1}$ ]
$h_{\text{out}}$	outside heat transfer coefficient [ $\text{J m}^{-2} \text{K}^{-1} \text{s}^{-1}$ ]
$J$	objective function [-]
$k_i$	mass transfer coefficient [ $\text{s}^{-1}$ ]
$k_f$	external film resistance coefficient [ $\text{s}^{-1}$ ]
$K_w$	thermal conductivity of column wall [ $\text{J m}^{-1} \text{K}^{-1} \text{s}^{-1}$ ]
$K_z$	effective gas thermal conductivity [ $\text{J m}^{-1} \text{K}^{-1} \text{s}^{-1}$ ]
$L$	column length [m]
$L_p$	particle length [m]
$P$	pressure [Pa]
$P_{\text{avg}}$	average pressure [Pa]
$P_H$	high pressure in cycle simulation [Pa]
$P_L$	low pressure in cycle simulation [Pa]
$Pe$	Peclet number [-]
$q$	solid phase concentration [ $\text{mol kg}^{-1}$ ]
$q_s$	saturation concentration in the solid phase [ $\text{mol kg}^{-1}$ ]
$q^*$	equilibrium solid phase concentration [ $\text{mol kg}^{-1}$ ]
$R$	universal gas constant [ $\text{Pa m}^3 \text{mol}^{-1} \text{K}^{-1}$ ]
$r_{\text{in}}$	column inner radius [m]
$r_{\text{out}}$	column outer radius [m]
$r_p$	particle radius [m]

$T$	temperature [K]
$Re$	Reynolds number [-]
$Sc$	Schmidt number [-]
$Sh$	Sherwood number [-]
$T_a$	ambient temperature [K]
$T_{\text{bath}}$	water bath temperature [K]
$T_w$	column wall temperature [K]
$t$	time [s]
$U$	internal energy [J mol <sup>-1</sup> ]
$v$	interstitial velocity [m s <sup>-1</sup> ]
$v_b$	bed volume [m <sup>3</sup> ]
$v_d$	apparatus dead volume [m <sup>3</sup> ]
$y$	gas phase composition [-]
$z$	axial coordinate [m]

#### Greek symbols

$\alpha$	price factor to normalize volume of adsorbent [-]
$\epsilon$	bed voidage [-]
$\epsilon_p$	particle voidage [-]
$\mu$	fluid viscosity [kg m <sup>-1</sup> s <sup>-1</sup> ]
$\rho_s$	adsorbent particle density [kg m <sup>-3</sup> ]
$\rho_w$	wall density [kg m <sup>-3</sup> ]
$\theta$	time ratio of the duration of LPP and HPP step to the adsorption step [-]
$\tau$	tortuosity [-]
$\eta$	compression efficiency [-]
$\gamma$	adiabatic constant [-]
$\lambda$	rate of pressure change [s <sup>-1</sup> ]

#### Subscripts

ADS	adsorption step
avg	average
DES	desorption step
EVAC	evacuation step
exp	experiment
FP	feed pressurization step

H	high
HPP	heavy product pressurization step
I	intermediate
in	inlet stream
L	low
LR	light reflux step
LPP	light product pressurization step
out	outlet stream
sim	simulation

# Chapter 1

## Introduction

## 1.1 Air separation

Atmospheric air mainly contains  $N_2$  (78.09%),  $O_2$  (20.95%), and Ar (0.93%) balanced with other components such as water and  $CO_2$ . Oxygen separation from air with purities higher than 95.0% is an essential part of industries such as steel, paper, and glass production. Oxygen in purities higher than 99.0% is required in medicine, aerospace, and semiconductor industries. According to The United States Pharmacopoeia (USP), "Oxygen" is expected to have a purity of 99.0% in USA [4]. This requirement is 99.5% in Europe [5], and 99.6% in Japan [1]. It is worth noting that another class of oxygen named "Oxygen 93" with a purity of 93% is also being recognized for medical applications. Military and aerospace applications require oxygen higher than 99.5% purity [6,7] and semi-conductor industry requires oxygen higher than 99.8% [8]. For large-scale processes similar to steel industry, where oxygen with purity of 95.0% is sufficient, cryogenic distillation is usually chosen as it is economically preferable compared to technologies such as adsorption separation processes. However, to produce  $O_2$  with purities higher than 99.0%, due to similar physical properties of oxygen and argon such as the molecular size ( $O_2$  kinetic diameter= 3.46 Å and Ar kinetic diameter=3.70 Å) and the boiling points ( $O_2$  boiling point= 90.15 K and Ar boiling point= 87.35 K), this separation is very challenging. While cryogenic distillation is the preferred process for large-scale  $O_2$  purification, adsorption separation techniques are more preferable for small- and medium-scale applications (less than 100 tons per day) as they offer more favorable process economics [9]. It is worth noting that in order to produce high-purity  $O_2$ ,  $N_2$  should be also removed either at the same time as separating Ar (single-stage separation) or prior to  $O_2$  purification (dual-stage separation). In other words, type of the products required ( $N_2$ ,  $O_2$ , or Ar), production rate, and purity level of the products determine the appropriate technology for the air separation unit in each application. In this section, an introduction to the technologies currently available for oxygen production is presented.

### 1.1.1 Cryogenic distillation

Air separation by Cryogenic distillation was introduced by Carl von Linde in early 20th century and still widely used in industry. The basis of this separation, similar to the other distillation processes, is based on the different volatilities of the components. In order to separate  $N_2$  and  $O_2$ , atmospheric air goes through different stages: compression, purification, and distillation. All the stages are conducted under very low temperatures and factors like the physical phase and delivery pressure of the product determine the

operating conditions. This technology is efficient for industries which require large-scale oxygen production with purities less than 95.0%. However, for an small/medium-scale application where argon also needs to be removed from O<sub>2</sub> product stream, cryogenic distillation is no longer considered an energy-efficient technology.

### 1.1.2 Membrane-based separation

Membrane technology has also been considered for high-purity oxygen production from air. This separation is based on the differences in the diffusion rates of oxygen, nitrogen, and argon. Oxygen is the smallest molecule compared to the other two and will diffuse faster through the membrane. Thus, a permeate rich in O<sub>2</sub> will be collected at the product side. Low energy consumption, ease of the operations, and the possibility of designing a continuous process are among the advantages of this technology. However, achieving O<sub>2</sub> purities higher than 99.0% and synthesizing the material at a larger scale still remains an issue.

### 1.1.3 Adsorption-based separation

Adsorption-based air separation consists of two different approaches: kinetic-based and equilibrium-based separations. In the kinetic-based separation, similar to the membrane-based technology, the separation is based on the differences in the diffusion rate of the molecules. The pore size of the adsorbents used in this type of separation is in the same order of magnitude of the kinetic size of the air components. Oxygen will diffuse faster compared to N<sub>2</sub> and Ar since the molecule has a smaller kinetic size compared to the other two molecules. Therefore, the adsorbent is more selective toward O<sub>2</sub> and the raffinate stream contains more N<sub>2</sub> and Ar whereas the extract is rich in O<sub>2</sub>. Carbon Molecular sieves are the most common adsorbent used in the kinetic-based air separation processes. In the equilibrium-based separation, pore aperture of the adsorbents is large enough to allow all the components to be adsorbed at the same rate. However, the components are separated based on the difference in their adsorption affinity. Nitrogen has the strongest interaction with the cations of the adsorbent and will retain inside the column. This means the adsorbents are selective toward N<sub>2</sub> and the raffinate stream is going to be rich in O<sub>2</sub> and Ar. Conventional adsorbents used in air separation such as zeolite 5A or LiX have no selectivity of Argon over oxygen or vice versa [10–15]. This makes producing high-purity O<sub>2</sub> very challenging if the choice of adsorbent is limited to these materials. However, over the past two decades, new adsorbents showing Ar/O<sub>2</sub> or O<sub>2</sub>/Ar selectivity

were introduced into the field. This opened up the possibility of using commercialized raffinate cycles for the purpose of high-purity oxygen production. This will be further discussed in the following section.

In order to design a continuous separation process, adsorption separation technologies are generally divided into three groups: pressure swing adsorption (PSA), temperature swing adsorption (TSA), and vacuum swing adsorption (VSA). The separation in all these three approaches relies on the change of adsorption affinity with the variation of the operating conditions such as the pressure and temperature. Adsorption affinity increases with a rise in pressure and a decrease in temperature. This assists in designing a simple three-step cycle with specific operating conditions for the initial step (pressurizing or cooling), conducting the adsorption step either at high pressure or low temperature, and regenerating the adsorbent (desorption) at low pressure or high temperature. Fulfilling the purity constraint for high-purity oxygen product may require introducing more complex cycles depending on the nature of adsorbent used and the purity requirements.

#### 1.1.4 Choice of adsorbent

When choosing an adsorbent for a separation process, several parameters need to be taken into account. The adsorbent should be selective toward one of the components and this selectivity should be high enough to meet the purity-recovery constraint. Selectivity of component A over component B is analogous to the relative volatility in the distillation and is defined as [32]:

$$\alpha_{AB} = \frac{X_A/X_B}{Y_A/Y_B} \quad (1.1)$$

where X and Y are the mole fractions of the corresponding components in the adsorbed and fluid phase at equilibrium, respectively. In addition to the high selectivity, the adsorbent should have large enough capacities and the kinetics of the adsorbent should be fast enough to allow achieving high productivity rates. Cost and ease of synthesis at larger scales plus stability at harsh operating conditions are also very important when choosing the appropriate adsorbent. As stated earlier, conventional adsorbents used for air separation do not show Ar/O<sub>2</sub> selectivity and cannot deliver O<sub>2</sub> with a purity greater than 95% [10–15]. Kinetic based separations using carbon molecular sieves (CMS) have been reported for this separation [10, 16, 17]. Limited number of adsorbents that can separate the two gases based on equilibrium have been also reported. The common characteristic between most of these adsorbent is the presence of silver in their structure. However, Afonso et al [18] have recently reported an Ar/O<sub>2</sub> equilibrium selectivity of 1.3 on Ag-free VA-class hydrophobic dipeptides. Argon showed the highest affinity followed by O<sub>2</sub> and

$N_2$ , respectively. Table 1.1 summarizes Henry’s law selectivity of  $Ar/O_2$  for some of the reported adsorbents.

Table 1.1: Reported Henry’s law selectivity of adsorbents showing  $Ar/O_2$  selectivity.

Adsorbent	$Ar/O_2$ selectivity	Temperature (K)	Reference
CMS	0.81-0.93	293.15 K	Jin et al. [17]
VA-class hydrophobic dipeptides	1.3	278.15 K	Afonso et al. [18]
Ag-Mordenite	1.17-1.19	303.15 K	Sebastian and Jasra [19]
Ag-ZSM-5	1.11-1.29	303.15 K	Sebastian and Jasra [19]
Ag-X	1.11	303.15 K	Sebastian and Jasra [19]
Ag-LiLSX	1.14	298.15 K	Ferreira et al. [20]
Ag-ETS-10 binderless	1.41-1.49	303.15 K	Anson et al. [21] and Shi et al. [22]
Ag-ETS-10	1.39	303.15 K	This study

As mentioned earlier, silver-exchanged adsorbents have shown  $Ar/O_2$  selectivity which points to the potential to produce high-purity  $O_2$  in a single-stage adsorption process. Silver mordenite [19,23], silver-exchanged zeolite-A [19], Ag-ZSM-5 [19], silver exchanged X-type zeolites [24,25], Ag-Li-LSX [20,26,27] have been reported as a potential adsorbent for  $Ar/O_2$  separation. Silver-exchanged Engelhard Titanosilicate (Ag-ETS-10), synthesized at the University of Alberta, has shown relatively high  $Ar/O_2$  selectivity compared to other reported adsorbents [21, 22]. On this material,  $N_2$  is the strongest component followed by  $Ar$  and  $O_2$ , respectively. This opens up the possibility of developing processes where high-purity  $O_2$  can be obtained as a raffinate (light) product as the adsorption processes have been commercialized only for situations where the desired product is collected as a raffinate. In this study, Ag-ETS-10 adsorbent, synthesized in the same research group, is characterized and used in all the experiments and cycle simulations.

### 1.1.5 Cycles for oxygen purification

Pressure swing adsorption (PSA) and vacuum swing adsorption are the two main processes reported in the literature for  $O_2$  purification. Sircar has reported  $O_2$  purification in a single stage VSA using zeolite 13X [28]. Jee et al. have also reported a two-bed PSA with various cycle configuration and a three-bed PVSA (pressure vacuum swing adsorption) with two consecutive blowdown steps using carbon molecular sieve (CMS) to develop high-purity  $O_2$  [8, 29]. Knaebel and Kandybin have shown  $O_2$  production in a single-bed PSA cycle using Ag-mordenite [23]. Air Products reported a process simulation for  $O_2$  production using AgLiLSX [30] which was later demonstrated experimentally [26]. Ferreira et al. reported experimental and process simulation of  $O_2$  production in a single-stage PVSA using AgLiLSX and were able to obtain 99.13%  $O_2$  purity with 6.2% recovery from air [31]. In another recent publication [1],  $O_2$  purity and recovery of the process was improved to

99.75% purity with 5.6% and 99.51% purity with 14.2% recovery using a two stage PVSA. The authors have shown that multiple approaches can be used to remove N<sub>2</sub> before using an oxygen VSA, e.g. by using a PSA for Nitrogen removal (kinetic or equilibrium) they were able to improve the purity and the recovery of the process by adding an intermediate blower. Table 1.2 shows a summary of O<sub>2</sub> purity and recovery obtained from P/VSA processes using various sorbents. The common point between these reported cycles, except the work by Jee et al [8] is the low O<sub>2</sub> recovery obtained. Designing new cycles with higher recovery values may assist in reducing the size of the column which is of interest for on-site high-purity O<sub>2</sub> production.

Table 1.2: Reported O<sub>2</sub>/Ar separation through P/VSA.

Adsorbent	Feed [N <sub>2</sub> /O <sub>2</sub> /Ar in %]	O <sub>2</sub> purity [%]	O <sub>2</sub> recovery[%]	Type	Reference
Ag-Mordenite	0/95/5	99.5-99.6	9.8-12.0	experiment and simulation	Knaebel and Kandybin [23]
CMS	0/95/5	99.8	78.0	experiment and simulation	Jee et al. [8]
AgLiLSX	0/95/5	98.98-99.65	2.93-4.29	experiment and simulation	Dee et al. [30] and Santos et al. [26]
AgLiLSX	78/21/1	99.13	6.2	experiment and simulation	Ferreira et al. [31]
AgLiLSX	0/95/5	99.15-99.28	8.6-12.0	experiment and simulation	Ferreira et al. [1]
AgLiLSX	78/21/1	99.51-99.75	5.6-14.2	experiment and simulation	Ferreira et al. [1]

### 1.1.6 Thermodynamics and kinetics of adsorption

Adsorption technology has been widely applied in gas separation and purification industries. Air separation, N<sub>2</sub>/CH<sub>4</sub> separation from natural gas, and H<sub>2</sub> purification are among the most common applications [32]. At this stage, only raffinate cycles, i.e. purifying light product, are commercialized. Recently numerous studies have discussed the potential of adsorption technology for heavy product separation (extract cycles). In order to design an appropriate process for any application, both thermodynamics and kinetics of the separation should be well understood. The former is usually studied by measuring adsorption equilibrium isotherms either by a volumetric or a gravimetric method [33,34]. In the volumetric approach two cells with known volumes are connected, where one cell is under vacuum with a known amount of previously activated (de-gassed) sample, and the other cell is filled with the adsorbate gas. Both temperature and pressure of the two cells are known and recorded. Certain amount of gas is dosed from the second cell to the cell under vacuum. Once the system reaches equilibrium, the amount adsorbed can be easily calculated by writing a mass balance on the gas phase before and after the dosing. This procedure is repeated for different pressure values until a full isotherm curve is obtained. In the gravimetric approach, a known amount of activated sample is exposed to the adsorbate at a certain pressure and constant temperature. Once equilibrium is reached, the adsorbed amount can be calculated from the weight change before and after injecting the adsorbate gas. Similar to volumetric method, this experiment will be repeated to measure

the amount adsorbed for the full range of pressure at the desired temperature. Dynamics of adsorption (i.e. momentum, heat, and mass transfer) can be understood using a dynamic column breakthrough (DCB) experiment. For an equilibrium-based separation, DCB seems to be sufficient enough to obtain the required information. However, for a kinetic-based separation, more detailed techniques, such as zero-length column chromatography [35], might be required to measure the diffusion rates of gas species inside the adsorbent particles. Since air separation on Ag-ETS-10 is an equilibrium-based phenomenon, only DCB experiments are considered in this study.

In DCB experiments, a column is packed with the adsorbent particles and is activated prior to conducting an experiment. The column is then introduced to pure, binary, and multi-component gas streams and the dynamics of adsorption is investigated by monitoring the gas phase composition at the outlet of the column as well as the pressure, flow rate, and axial temperature profiles across the column. Both adsorption and desorption experiments can be conducted using a DCB apparatus. However, several factors need to be considered before designing the system. Column dimensions should be designed such that ratio of the gas in the dead volume of the apparatus to the gas adsorbed on the adsorbent particles is negligible. At the same time the column size should be chosen so that the duration of the experiments, specially desorption runs, are feasible. In addition to this, large pressure drop and channeling should be avoided. Sufficient number of instruments such as flow controllers and meters, thermocouples, and pressure transducers should be used in order to acquire all the data required to perform a mass balance around the system and obtain all the information needed to investigate dynamics of the system. It is worth noting that the dynamics of this experiment is affected by adsorption equilibrium as well as adsorption kinetics and fluid dynamics. Therefore, accurate measurement of equilibrium of the adsorbate-adsorbent system with an independent technique, such as volumetric method, is very important. Fluid dynamics of the system can be well described by an equation of state (EOS). Therefore, kinetics of adsorption can be studied using a properly designed DCB experiments by feeding the inputs from the independent equilibrium measurement to a generic model and describing the profiles observed in the DCB experiments with the model. Moreover, effect of the competition between multiple adsorbate on the equilibrium can be easily studied using DCB experiment by feeding a multi-component gas stream to the system. It is important to mention that investigating this effect by a volumetric or a gravimetric method is not straightforward. In this study, volumetric method is used to obtain isotherms of  $N_2$ ,  $O_2$ , and Ar and DCB experiments is used to validate the model and study dynamics of the separation more thoroughly.

### 1.1.7 Pressure swing adsorption (PSA)

Pressure swing adsorption (PSA) is a technology used in gas industry to separate gases based on the differences in their affinities at different levels of pressure [3,32]. This difference is usually referred to selectivity of the adsorbent towards one of the adsorbates. This selectivity can emerge from the difference in the equilibrium loading (thermodynamics) of the gases or the difference in the diffusion rates (kinetics) [36]. The size of the separation unit predominately depends on the difference between the amount adsorbed at high and low pressures for the desired product. This value is known as working capacity and is illustrated in Figure 1.1. In a PSA process, the concept of selectivity and working capacity is used to design a process. Basic PSA process, as shown in Figure 1.2, consists of three steps: adsorption, blowdown, and pressurization [37]. During an adsorption step, feed is introduced to the column at high pressure. The preferably adsorbed species is retained in the column while the other species will leave the column and are collected as the raffinate product. In the blowdown step, the column pressure is reduced to a lower value in order to regenerate the column and the preferably adsorbed component is collected as the extract product at the feed side of the column. During the pressurization step, the column is pressurized back to the high pressure with the feed stream in order to make it ready for the next cycle. In more complex cycles, to improve the recovery of the cycle, both raffinate or extract streams can be used to pressurize the column. The minimum number of columns for a continuous process is two. However, more columns may be required for more complex cycles.

Skarstrom [38] proposed adding a purge step after the blowdown step in order to improve the recovery of the light product. During this step, part of the raffinate stream is refluxed back to the column which will help in pushing the concentration front of the preferably adsorbed component back to the feed end. Later Berlin [39] proposed adding a pressure equalization step where the ends of the two columns, one at high pressure and one at low pressure, are connected. Therefore, the pressure in both of the columns will be equalized and this results in reduction of the energy consumption and higher recovery since one column is partially pressurized with the high pressure gas in the other column instead of pressurizing with the feed stream. Table 1.3 summarizes some of the most common applications of PSA technology in the area of gas separation.

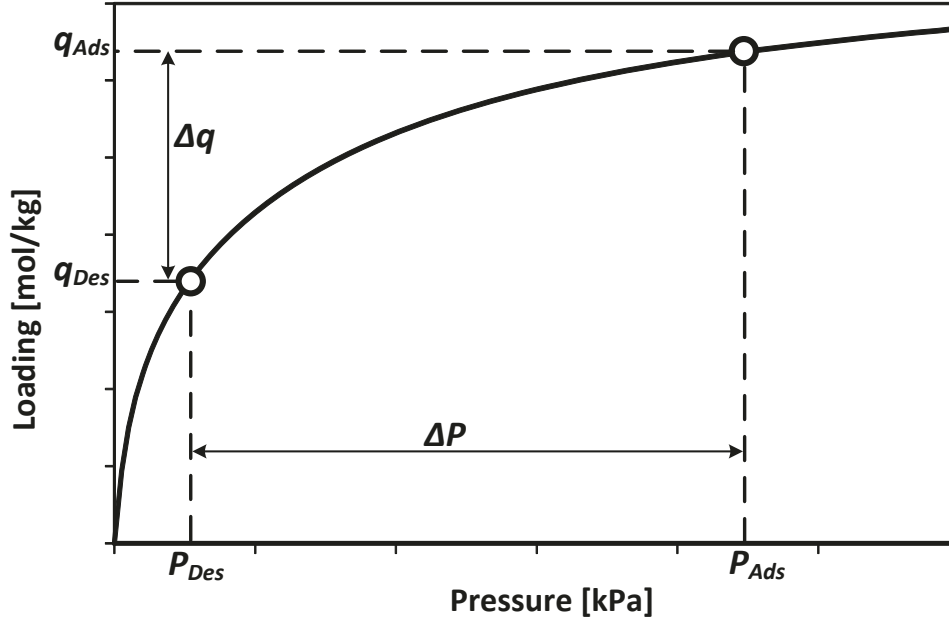


Figure 1.1: Pressure dependency of adsorption explored in pressure swing adsorption processes.  $\Delta q$  represent working capacity between the adsorption and desorption pressures,  $P_{Ads}$  and  $P_{Des}$ , respectively.

Table 1.3: Some of the applications of PSA in the area of gas separation [2, 3].

Adsorbent	Application
Alumina, Zeolites 4A and 5A	air drying
Zeolite 5A	H <sub>2</sub> recovery
Carbon Molecular sieve (CMS), Na-ETS-10	N <sub>2</sub> production
Zeolites 5A and 13X	O <sub>2</sub> production
Zeolite 13X	N <sub>2</sub> /CO <sub>2</sub> separation
Zeolite 13X	H <sub>2</sub> /CO <sub>2</sub> separation
CMS	CH <sub>4</sub> recovery

In order to evaluate the performance of an adsorption cycle, product purity, product recovery, productivity and total energy consumption of the cycle are considered. Product purity is the average concentration of the desired component in the product over the period of collection. Product recovery is defined as the amount of desired component collected in the product divided by the amount of the same component introduced to the column during the adsorption and pressurization step. Productivity is defined as the amount of the target component collected in the product per unit volume or mass of the adsorbent per unit time. Total energy consumption is measured as the total energy consumed in one cycle per unit mass or mole of the desired component collected in the product. The advantage of PSA over other adsorption technologies such as temperature swing adsorption (TSA) is the faster cycles since reducing and increasing pressure is much faster than changing

temperature levels which results in higher productivity. However, a PSA process requires more valves and vacuum pumps compared to a TSA process and scheduling the steps is more complex. It is worth noting that if the low pressure during the regeneration step is less than the ambient pressure, then the process is called vacuum swing adsorption (VSA) and the regeneration step is called evacuation instead of blowdown. VSA process consumes more power compared to PSA due to the lower pressure levels. However, similar to the case of  $O_2/Ar$  separation on Ag-ETS-10 in this study, going to vacuum levels might be helpful to meet the purity constraints due to the higher selectivity at lower pressures.

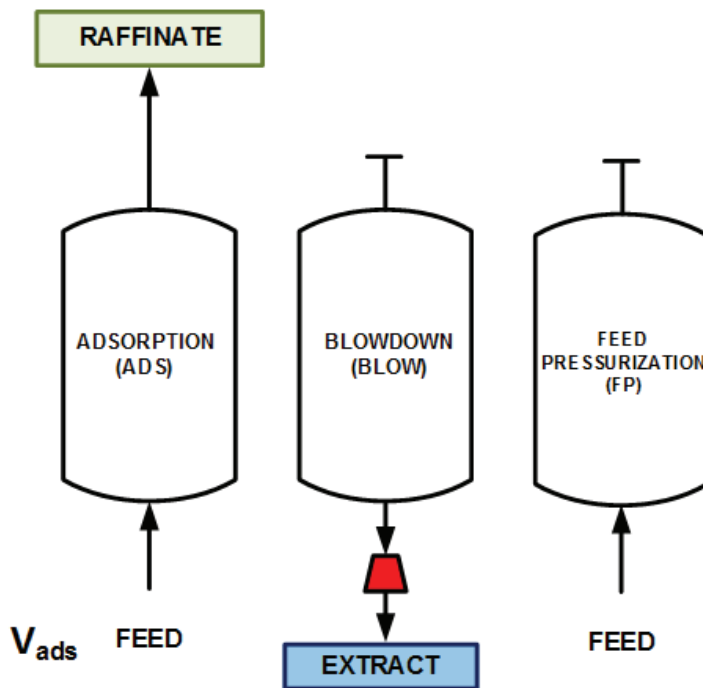


Figure 1.2: Schematic representation of a basic 3-step PSA cycle.

### 1.1.8 Modeling and simulation of adsorption

Modeling and simulation of the adsorption processes assists in ranking the adsorbents and choosing the promising ones for the next steps of any study on adsorption processes [40]. Once the material is chosen, DCB experiments can be used to validate the model and based on that validated model, cycles can be designed and the economics of the process can be studied before moving to pilot-scale demonstration. There are mainly two approaches to model an adsorption process. The first approach is to consider a simplified model such as equilibrium theory model [41] or batch adsorber model [42] where instantaneous equilibrium is assumed between the adsorbent and the adsorbate. These models can provide information about the best possible performance of an adsorbent and a cycle

and can be used to rank the materials at a short computation time. The other approach to model adsorption process is to use a dynamic model where finite mass transfer and other effects such as dispersion are taken into account. Therefore, in order to simulate the process, a system of coupled non-linear momentum, heat, and mass balance partial differential equations (PDE) should be solved numerically in parallel. Appropriate initial and boundary conditions for each of these PDEs need to be defined and these equations should be discretized in space or time using numerical methods such as finite difference and finite volume technique. The resulting ordinary differential equations (ODE) can be solved using programming tools available such as MATLAB or COMSOL. Obviously, this approach requires better computations resources compared to the first approach but can be reliably used to predict cycle performance and can be later used in optimizing the operating conditions in order to meet the target performance indicators.

In this study adsorption equilibrium is modeled by well-known Langmuir model [43]. This empirical model assumes the molecules are adsorbed at a fixed number of site with identical energies. Each site can only accommodate one molecule and there is no interaction between molecules adsorbed on two neighboring sites. In other words, the original Langmuir model assumes homogeneous site with identical energies. However, this might not be true for all the systems. Therefore, this model is modified to dual-site Langmuir model by introducing a second term. More details about these models and the fitting parameters is provided in Chapters 2 and 3.

In almost all of the applications of adsorption processes, more than one component is present and therefore, competitive adsorption equilibrium between the multiple components present should be well described in order to design a separation process. This can be done by ideal adsorbed solution (IAS) theory or the extension of single-component models to multi-component systems, known as extended single-site or dual-site Langmuir model. In this study, it was shown that the extended Langmuir model was able to describe the competition between  $N_2$ ,  $O_2$  and Ar. This was confirmed by comparing the experimental equilibrium loading from DCB experiments and those predicted by the extended Langmuir model and will be discussed in Chapter 2.

Kinetics of adsorption can also be described using two different approaches: pore diffusion model and linear driving force (LDF) model. In the pore diffusion model [44], local loading at every point within the adsorbent particle is calculated by solving the detailed diffusion equation for the particle. However, in the LDF model, an average concentration is assumed for the adsorbent particle and a lumped mass transfer coefficient is assumed. Chapter 2 provides more details on this model. It has been shown in the literature that LDF is sufficient enough in most of the equilibrium-based separations to describe adsorption kinetics [45]. In this study, since the pore opening of Ag-ETS-10 is much larger

than  $N_2$ ,  $O_2$ , and Ar molecule sizes, LDF model is used to describe the kinetics of the separation.

### 1.1.9 Optimization of adsorption processes

As discussed earlier, the performance of an adsorption process is usually evaluated by indicators such as product purity, product recovery, productivity, and total energy consumption. Purity and recovery targets are usually decided by the application, as in  $O_2$  purification, or by regulatory targets set by responsible institutions. Energy and productivity may be considered as a proxy for the operating and capital cost, respectively. Reaching the global optimal operating conditions for an adsorption process with the aid of process optimization can save a significant amount of time and energy. Therefore, optimization of energy-productivity is of outstanding importance. However, the purity-recovery constraints should be also met while the optimal operating conditions are found for energy-productivity values. Therefore, a global optimization tool, which considers multiple objective functions and satisfies all the constraints, is required. The complexity of multi-step multi-component dynamic adsorption processes requires the optimization routines to be accurate and at the same time the optimization needs to be done at a reasonable amount of time. It is worth noting that adsorption processes need to pass through a transient state before reaching cyclic steady state. This can be anywhere from less than 50 cycles for less complex systems to more than 100 cycles for more complex systems. Hence, the optimization routine needs to be well-optimized for a prompt and precise outcome.

Depending on the optimization method, definition of objective functions, and the method used to solve PDEs, multiple approaches are available in the literature [46–51]. Multi-objective optimization algorithms provide a robust approach by creating many generations of the operating conditions but involves computational complexity. Non-dominated sorting genetic algorithm II (NSGA-II), used in this study, introduced elitism to the original approach and hence, reduced the computation time [51]. This approach mimics biological evolution by using natural selection strategy. The algorithm chooses an initial population of the decision variables and calculates a fitness value for each of the decision variables. Based on the fitness value, new members of the population, called parents are created and then children are created either by a crossover between the parents or by mutation, where random changes are made to a single parent. In the next stage, the parents are replaced by the children and this will continue until an optimal solution is found. This approach is stochastic and is able to escape a local minimum but does not guarantee reaching the global optima. However, it is available in MATLAB optimization toolbox and can be linked to the PSA model described earlier and easily parallelized on multiple

cores, therefore, reducing the computation time. It is worth noting that this approach has been successful in predicting the performance indicators in a pilot plant adsorption unit [52] which further verifies its success in scaling up.

In this study, GA was used to optimize the operating condition for purity-recovery and energy-productivity optimizations. Figure 1.3 shows the typical work-flow of an optimization routine in this study. As it can be seen, the optimizer chooses a random set of decision variables as the initial population and introduces them to the full PSA model. The model later calculates the objective functions ( $J_1$  and  $J_2$ ), that is a function of performance indicators (P.I.), e.g. purity and recovery. This procedure is repeated once the stopping criteria, which is usually the number of generations or the tolerance of the objective functions, is met. However, for a constraint optimization such as energy-productivity, where a certain product purity or recovery is required, the objective function is penalized if the constraints are not satisfied. This will prevent the optimizer from choosing the operating conditions that are far from meeting the desired constraints. In the last stage, the optimizer returns a trade-off between the two objective functions with the optimal operating conditions.

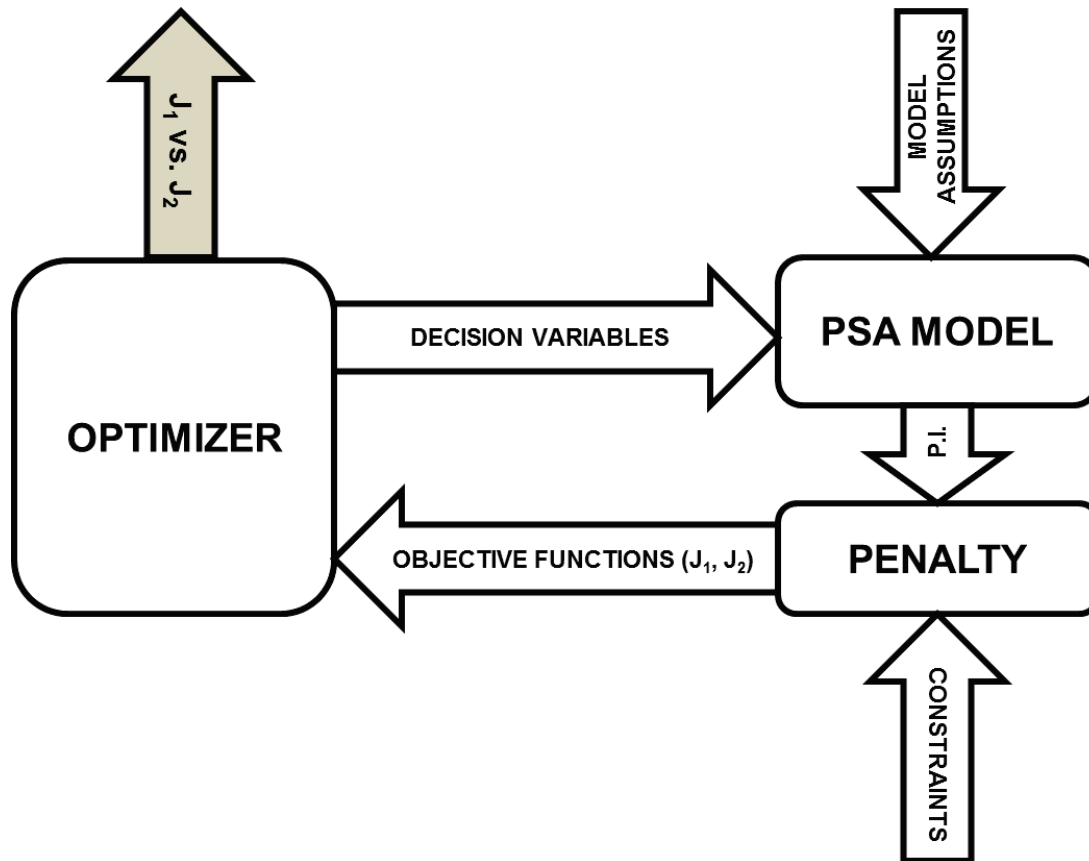


Figure 1.3: Typical work-flow of the PSA optimization routine in this study.

## 1.2 Challenges in high-purity oxygen production

Although air separation with adsorption technology has been widely studied over the past decades and commercialized, producing  $O_2$  with purities higher than 99.0% still remains a challenge. The three main challenges, that this thesis addresses, are as follows:

- Few adsorbents are reported in the literature with sufficient  $Ar/O_2$  or  $O_2/Ar$  selectivity for high-purity  $O_2$  production. Ag-ETS-10 has previously shown selectivity of around 1.5 for  $Ar/O_2$  [21,22], which is to the best of our knowledge the highest equilibrium selectivity reported for this separation. However, exploring the possibility of producing high-purity  $O_2$  using Ag-ETS-10 at a larger scale is necessary.
- On the other hand, the recovery of PSA process for  $O_2$  production is generally low (Table 1.2). Further, most of the applications for high-purity  $O_2$  are aimed for small-scale on-site  $O_2$  production and require higher recoveries in order to reduce the equipment size. Therefore, size of the adsorption unit is an important factor and designing advanced PSA cycles with higher recoveries, that results in smaller columns, is of great interest.
- Obtaining a trade-off between multiple performance indicators such as  $O_2$  purity and  $O_2$  recovery or productivity and total energy consumption of the cycle is not straight forward. Creating robust and efficient optimizations routines to obtain these trade-offs will assist in comparing different cycle configurations and choosing the most optimal design while meeting the constraints.

## 1.3 Objectives and structure of the thesis

The principal objective of this thesis is to characterize Ag-ETS-10 adsorbent for high-purity oxygen production from air, validate the large-scale performance of the material experimentally, design VSA processes and optimize them for high-purity oxygen production, and validate experimental performance of Ag-ETS-10 in a lab-scale VSA process. To reach the main objectives, the following key steps were followed:

- The experimental single-component low-pressure and high-pressure adsorption isotherms at different temperatures were measured and fitted to an empirical model for Ag-ETS-10 extrudates used in the next stages of this study.
- A lab-scale dynamic column breakthrough adsorption apparatus was designed and

constructed. Detailed pure, binary, and ternary breakthrough experiments were performed in order to validate large-scale performance of Ag-ETS-10 for O<sub>2</sub> purification.

- A rigorous and efficient model was implemented and validated with the experimental breakthrough data such as the concentration and temperature profiles. Dynamics of the separation was extensively studied by investigating the effect of multiple parameters such as the adsorbent particle size, feed velocity, pressure, and temperature on the breakthrough profiles.
- The model was extended to simulate different PVSA configurations. New VSA cycles were proposed and simulated to verify the potential of Ag-ETS-10 for high purity O<sub>2</sub> production.
- Two sets of multi-objective optimization studies were conducted, first to determine the optimal process conditions to maximize O<sub>2</sub> purity and recovery and second to minimize energy consumption and maximize productivity of the cycles designed while meeting different O<sub>2</sub> purity constraints. Significant improvement in the performance indicators was obtained through process optimization.
- Experimental performance of Ag-ETS-10 was validated with the Skarstrom VSA configuration and the values of experimental purity and recovery were compared with those predicted by the simulations.

Chapter 2 presents characterization of Ag-ETS-10 adsorbent by single-component adsorption isotherms of O<sub>2</sub>, Ar, and N<sub>2</sub> using a volumetric technique and single, binary, and ternary breakthrough profiles which were measured using a laboratory scale dynamic column breakthrough apparatus. A simple vacuum swing adsorption process (VSA) is also simulated and optimized in this chapter to demonstrate the potential of the material to produce high-purity oxygen.

Chapter 3 provides a detailed study on the mass transfer dynamics of O<sub>2</sub> separation using Ag-ETS-10. The effect of adsorbent particle size, feed flow rate, temperature, and pressure on the breakthrough profiles are studied. Influence of macropore, micropore, and film resistance and dispersion within the column is investigated based on these experimental results using fundamentals of mass transfer which assists in classifying the dynamics of this separation.

Chapter 4 discusses the possibility of using various vacuum swing adsorption (VSA) cycle configurations including the simple Skarstrom cycle, a 6-step with pressure equalization and light product pressurization, and 6-step with pressure equalization and heavy product equalization to maximize O<sub>2</sub> purity, recovery, and productivity, and to minimize total

energy consumption of the cycles. The effect of different operating parameters such as the bed length and the nitrogen content in the feed on the performance indicators is also presented and the experimental Skarstrom VSA cycles are compared with the predictions from the model.

Chapter 5 provides a detailed comparison between all the cycles proposed in the previous chapter. The possibility of performing a single-stage separation is investigated and the results are compared with different combinations of dual-stage processes by looking into the energy-productivity optimization results. Experimental Skarstrom VSA cycles are compared with the predictions from the model. A simple graphical scheduling study was also conducted in order to calculate the number of columns required for a continuous process using the better performing configurations.

Chapter 6 provides the conclusions of this work as well as recommendations for further studies.

## Chapter 2

# Characterization of Ag-ETS-10

Many medical and industrial applications require high-purity oxygen. Due to the similar physical properties of oxygen and argon, this separation is very challenging and very few commercial adsorbents offer the ability to separate the two gases. Silver exchanged titanosilicates (Ag-ETS-10) have the potential to separate these gases based on their adsorption affinities. In this work, adsorption isotherms of O<sub>2</sub>, Ar, and N<sub>2</sub> on Ag-ETS-10 extrudates have been measured using a volumetric technique and described using a Langmuir isotherm. Single, binary, and ternary breakthrough profiles were measured using a laboratory scale dynamic column breakthrough apparatus. These profiles have been modeled by writing mass and energy balances that are solved using the finite volume technique. The model was able to predict the experimental profiles to a high degree of accuracy. A simple vacuum swing adsorption process (VSA) was simulated using mathematical models to demonstrate the potential of the material to produce high-purity oxygen. Multi-objective optimization to maximize O<sub>2</sub> purity and recovery from a feed containing 95% O<sub>2</sub> and 5% Ar revealed that purities in excess of 99.0% can be achieved at a recovery of 11.35%.

## 2.1 Introduction

The separation of oxygen and argon is an important process for many applications such as in medicine, waste water treatment, aerospace, welding, and steel production [8,53]. Many of these applications require high-purity oxygen in excess of 99%. According to The United States Pharmacopoeia (USP), "Oxygen" is expected to have a purity of 99% in USA [4]. This requirement is 99.5% in Europe [5], and 99.6% in Japan [1]. It is worth noting that another class of oxygen named "Oxygen 93" with a purity of 93% is also being recognized for medical applications. Military and aerospace applications require oxygen higher than 99.5% purity [6,7] and semi-conductor industry requires oxygen higher than 99.8% [8]. Due to the similar physical properties of oxygen and argon such as size ( $O_2$  kinetic diameter= 3.46 Å and Ar kinetic diameter=3.70 Å) and boiling points ( $O_2$  boiling point= 90.15 K and Ar boiling point= 87.35 K), this separation is very challenging. While cryogenic distillation is the preferred process for large-scale  $O_2$  purification, adsorption separation techniques are more preferable for small- and medium-scale applications (less than 100 tons per day) as they offer more favorable process economics [9]. It is worth noting that adsorption-based high purity (99.5%) oxygen purifiers are already commercialized with multiple vendors providing this technology [54].

Conventional adsorbents used for air separation do not show Ar/ $O_2$  selectivity and cannot deliver  $O_2$  with a purity greater than 95% [10–15]. Carbon molecular sieves (CMS) are able to separate  $O_2$  and Ar based on the kinetics of adsorption [10,16,17] and few adsorbents that can separate the two gases based on equilibrium have been reported. Afonso et al [18] have recently reported an Ar/ $O_2$  equilibrium selectivity of 1.3 on Ag-free VA-class hydrophobic dipeptides. Argon showed the highest affinity followed by  $O_2$  and  $N_2$ , respectively. Table 1.1 summarizes Henry's law selectivity of Ar/ $O_2$  for some of the reported adsorbents. Silver-exchanged adsorbents have shown Ar/ $O_2$  selectivity and have created a potential to produce high-purity  $O_2$  in a single stage adsorption process. Silver mordenite [19,23], silver exchanged zeolite-A [19], Ag-ZSM-5 [19], silver exchanged X-type zeolites [24,25], Ag-Li-LSX [20,26,27] have been reported as a potential adsorbent for Ar/ $O_2$  separation. Recently, silver-exchanged ETS-10 (Ag-ETS-10) has shown relatively high Ar/ $O_2$  selectivity compared to other reported adsorbents. [21,22] On this material  $N_2$  shows the strongest affinity followed by Ar and  $O_2$ , respectively. This opens up the possibility of developing processes where high-purity  $O_2$  can be obtained as a raffinate (light) product. It is worth noting that adsorption processes have been commercialized only for situations where the desired product is collected as a raffinate.

Experimental and process simulation of  $O_2$  purification using pressure swing adsorption

(PSA) and vacuum swing adsorption (VSA) have been reported in literature. Sircar has reported O<sub>2</sub> purification in a single stage VSA using zeolite 13X [28]. Jee et al. have reported a two-bed PSA with various cycle configuration and a three-bed PVSA (pressure vacuum swing adsorption) with two consecutive blowdown steps using carbon molecular sieve (CMS) to develop high-purity O<sub>2</sub> [8, 29]. Knaebel and Kandybin have shown O<sub>2</sub> production in a single-bed PSA cycle using Ag-mordenite [23]. Air Products reported a process simulation for O<sub>2</sub> production using AgLiLSX [30] which was later demonstrated experimentally [26]. Recently, Ferreira et al. reported experimental and process simulation of O<sub>2</sub> production in a single-stage PVSA using AgLiLSX and were able to obtain 99.13% O<sub>2</sub> purity with 6.2% recovery from air [31]. In another recent publication [1] from the same authors, O<sub>2</sub> purity and recovery of the process was improved to 99.75% purity with 5.6% and 99.51% purity with 14.2% recovery using a two stage PVSA. The authors [1] have shown that multiple approaches can be used to remove N<sub>2</sub> before using an oxygen VSA, e.g. by using a PSA for Nitrogen removal (kinetic or equilibrium) they were able to improve the purity and the recovery of the process by adding an intermediate blower. Table 1.2 shows a summary of O<sub>2</sub> purity and recovery obtained from P/VSA processes using various sorbents. In this work, adsorption isotherms of O<sub>2</sub>, N<sub>2</sub> and Ar on Ag-ETS-10 extrudates have been obtained using a volumetric apparatus over a range of temperatures and pressures and described using a suitable isotherm model. A laboratory-scale dynamic column breakthrough apparatus was used to validate the large-scale performance of the adsorbent, using both pure gases and mixtures. From these experiments, competitive isotherms were measured and compared to those predicted by the model. A mathematical model was developed by writing mass and energy balances in order to describe the breakthrough experiments. Finally, a simple 4-step vacuum swing adsorption (VSA) cycle was simulated to estimate the potential of the process to produce high-purity oxygen.

## 2.2 Materials and methods

### 2.2.1 Materials

As a first step, Na-ETS-10 was synthesized by the hydrothermal method [22, 55] and then formed into 1/16" extrudates with the use of a binder. The extruded sample was twice ion-exchanged with silver nitrate solution, containing 1.5 times the mass of the Na-ETS-10 in the column, at 358.15 K by using a strip column setup with 30 wt.% silver loading. Prior to each set of experiments, the Ag-ETS-10 extrudates were activated for 16

hours at 523.15 K under a N<sub>2</sub> environment. All gases in this study (99.999% N<sub>2</sub>, 99.999% Ar, 99.999% He, dry air, 95% O<sub>2</sub>/5% Ar, 50% O<sub>2</sub>/50% Ar, and 70% O<sub>2</sub>/30% Ar) were obtained from Praxair Canada Inc.

### 2.2.2 Isotherm measurements

Adsorption isotherms of pure N<sub>2</sub>, O<sub>2</sub>, and Ar on Ag-ETS-10 were measured using a Micromeritics ASAP 2020C volumetric physisorption system. This instrument delivers high resolution data in the Henry’s law region. Samples (~500 mg) were loaded into quartz U-tubes and activated under N<sub>2</sub> flow of 200 ml/min at 523.15 K overnight. The sample was held isothermally under N<sub>2</sub> flow for 15 min before applying vacuum for 60 minutes at a pressure of less than 0.5 Pa. Once the temperature in the furnace was stable, equilibrium data was collected. Adsorption isotherms of all three gases were measured at 303.15, 323.15, and 343.15 K from 0 to 115 kPa. All experiments were performed at low pressures where the measured quantity can be conveniently assumed to be the absolute adsorbed amount.

## 2.3 Dynamic column breakthrough experiments

A lab-scale dynamic column breakthrough apparatus, shown in Figure 2.1, was designed and constructed to validate the large-scale performance of the Ag-ETS-10 adsorbents to separate O<sub>2</sub> from air. This apparatus was designed to record relevant parameters required to study adsorption column dynamics. The stainless steel column had a volume of 325.6 cc and a packed length of 32 cm. The inner and outer diameters were 3.6 cm and 4.8 cm, respectively. The column was placed in a water bath to ensure the experiments are conducted in an isothermal condition. The temperature was controlled using a water circulation bath (PolyScience, Niles, Ill, USA). Two mass-flow controllers (Parker/Porter, Hatfield, PA, USA) located at the column inlet, were used to control the flows of the purge and test gas in the range of 0 to 5000 sccm. The outlet flow rate is measured using a flow meter (Parker/Porter, Hatfield, PA, USA) in the range of 0 to 500 sccm. The accuracy of the flow meter is  $\pm 1\%$  FS. Two thermocouples (Omega Engineering, Stamford, CT, USA) were positioned along the bed at 8 cm and 24 cm from the inlet to record temperature changes. The inlet pressure was monitored using a pressure transducer (GE Druck, Billerica, MA, USA). A differential pressure transducer (GE Druck, Billerica, MA, USA) was used to measure pressure drop across the bed. A back pressure regulator (Swagelok, Solon, OH, USA) was located at the outlet to maintain the system pressure

at a desired value. The outlet gas composition was monitored by a mass spectrometer (Pfeiffer Vacuum OmniStar GSD 320, Asslar, Germany). A data acquisition system was built using LabView to control and record all the measured parameters.

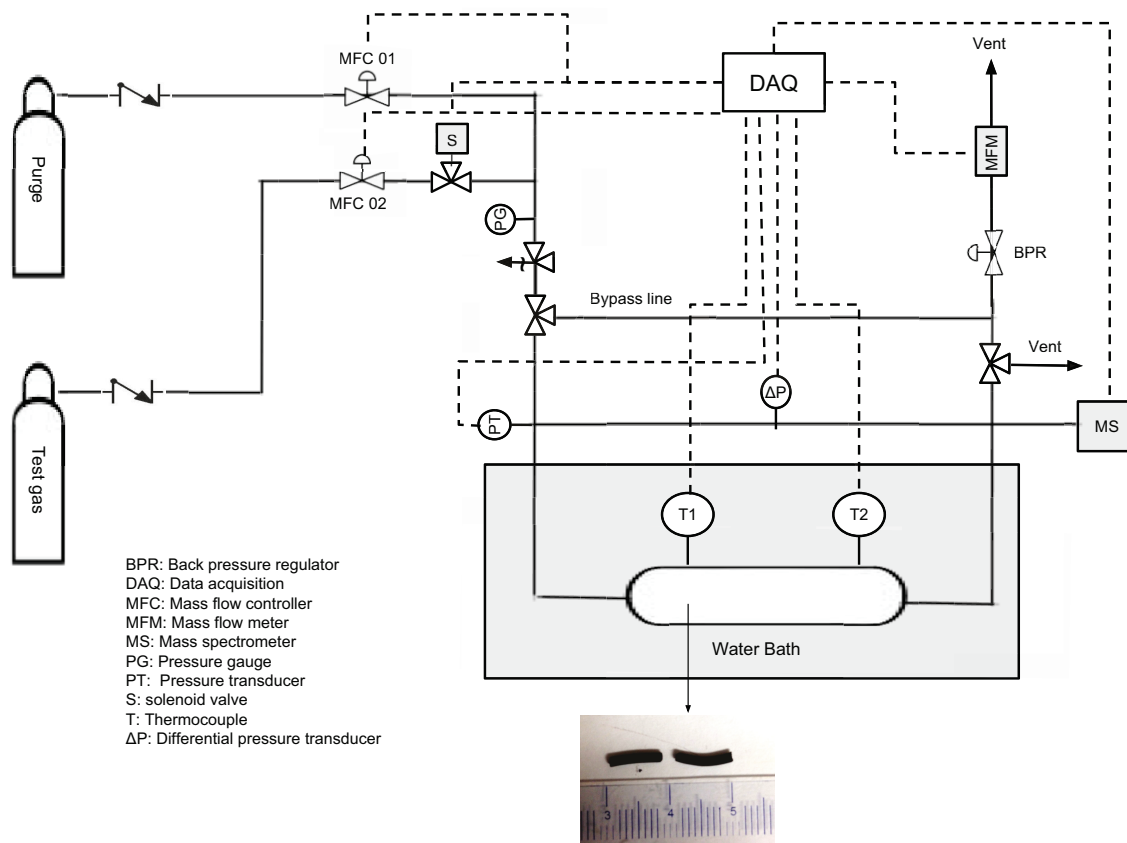


Figure 2.1: Schematic diagram of dynamic-column breakthrough apparatus. Picture at the bottom shows Ag-ETS-10 extrudates along with a ruler (units in cm)

The column with Ag-ETS-10 extrudates was activated in an oven at 523.15 K for 12 hours with a purge of He prior to each set of experiments. Mass flow controllers and the mass flow meter were calibrated at different pressures and gas compositions using a universal gas flow meter (Agilent technologies, Santa Clara, CA, USA). The mass spectrometer signal was also calibrated prior to each run using gases of known compositions. The bed was initially saturated with the purge gas and then switched to the test gas for the adsorption experiments and switched back to the purge gas for the desorption experiments. The flow rates were controlled by the mass flow controllers with given set points. In this study, breakthrough profiles at 303.15 K and 95 kPa were obtained for pure N<sub>2</sub>, pure Ar, dry air, and various O<sub>2</sub>/Ar mixtures (95/5, 70/30, and 50/50). Experiments were conducted normally at flow rate of 150 ccm (P=95 kPa, T=293.15 K). Prior to performing the breakthrough experiments, the dead volume in the upstream and downstream piping

was estimated by replacing the column with a union and running a blank breakthrough experiment. These experiments revealed that the dead volume in the system (piping and instruments) was 15 cc compared to the empty column volume of 325.6 cc. Since the dead volume was much smaller compared to the column volume and the spread of the breakthrough arising from extra-column volume was minimal, a simple point-by-point correction was used to correct the adsorption and desorption breakthrough curves [56].

## 2.4 Modeling

### 2.4.1 Modeling column dynamics

A generic dynamic column breakthrough model was developed to simulate the dynamic column breakthrough experiments. This model includes contributions from dispersion, convection, adsorption, pressure drop across the column, and heat transfer. The model was developed based on the following assumptions:

1. The gas phase is ideal since all experiments are conducted at low pressure ( $<200$  kPa) and 303.15 K.
2. No radial gradients of composition and temperature exist in the column.
3. The flow in the column is adequately described by the axially-dispersed plug flow model.
4. The temperature at the water bath, is constant and uniform around the column.
5. The heat transfer resistance is lumped into the inside and outside heat transfer coefficients.
6. The gas and the solid phases are in thermal equilibrium.
7. The specific heat capacity of the adsorbed phase is equal to that of the gas phase.
8. The pressure drop in the column is described by the Darcy's law, since the experiments were performed at low flow rates and the maximum measured pressure drop was 1.4 kPa.
9. The binary and ternary equilibrium were assumed to be adequately described by the extended Langmuir isotherm.
10. The mass transfer resistance is controlled by molecular diffusion in the macropores.

Based on this assumptions fluid phase mass balance for component  $i$  is given by:

$$\frac{\partial c_i}{\partial t} = \frac{\partial}{\partial z} \left( c D_L \frac{\partial y_i}{\partial z} + c_i v \right) - \frac{1 - \epsilon}{\epsilon} \frac{\partial q_i}{\partial t} \quad (2.1)$$

where  $c_i$  is the fluid phase concentration of component  $i$ ,  $D_L$  is the axial dispersion coefficient,  $y_i$  is fluid phase mole fraction of component  $i$ ,  $v$  is the interstitial velocity in  $z$  direction,  $\epsilon$  is bed voidage and  $q_i$  is solid phase concentration of component  $i$ . The axial dispersion coefficient,  $D_L$  is described by the following equation [32]:

$$D_L = 0.7 D_m + 0.5 v d_p \quad (2.2)$$

where  $D_m$  is the molecular diffusivity and  $d_p$  is the diameter of the adsorbent particle. Using the ideal gas law, Eq. 2.1 is rearranged to give:

$$\frac{\partial y_i}{\partial t} + \frac{y_i}{P} \frac{\partial P}{\partial t} - \frac{y_i}{T} \frac{\partial T}{\partial t} = \frac{T}{P} D_L \frac{\partial}{\partial z} \left( \frac{P}{T} \frac{\partial y_i}{\partial z} \right) - \frac{T}{P} \frac{\partial}{\partial z} \left( \frac{y_i P}{T} v \right) - \frac{RT}{P} \frac{1 - \epsilon}{\epsilon} \frac{\partial q_i}{\partial t} \quad (2.3)$$

Using the same approach, the total mass balance can be written as:

$$\frac{1}{P} \frac{\partial P}{\partial t} - \frac{1}{T} \frac{\partial T}{\partial t} = - \frac{T}{P} \frac{\partial}{\partial z} \left( \frac{P}{T} v \right) - \frac{RT}{P} \frac{1 - \epsilon}{\epsilon} \sum_{i=1}^{n_{comp}} \frac{\partial q_i}{\partial t} \quad (2.4)$$

The mass transfer into the solid phase is described by Linear driving force (LDF) model:

$$\frac{\partial q_i}{\partial t} = k_i (q_i^* - q_i) \quad (2.5)$$

where  $q_i^*$  is solid phase equilibrium capacity and  $k_i$  is the lumped mass transfer coefficient of component  $i$ . Considering macropore diffusion resistance,  $k_i$  can be described by [32]:

$$k_i = \frac{15 \epsilon_p D_p}{r_p^2} \quad (2.6)$$

where  $\epsilon_p$  and  $r_p$  are particle porosity and radius respectively.  $D_p$  is macropore diffusivity and is defined by the following equation:

$$D_p = \frac{D_m}{\tau} \quad (2.7)$$

where  $D_m$  is molecular diffusivity that is calculated from Chapman-Enskog theory [57] and  $\tau$  is adsorbent tortuosity. Darcy's law is used to calculate pressure drop across the column:

$$-\frac{\partial P}{\partial z} = \frac{150}{4} \frac{1}{r_p^2} \left( \frac{1 - \epsilon}{\epsilon} \right)^2 \mu v \quad (2.8)$$

where  $\mu$  is fluid viscosity and is assumed to be independent of temperature. The energy balance along the column is described by:

$$\left[ \frac{1-\epsilon}{\epsilon} \left( \rho_s C_{p,s} + C_{p,a} \sum_{i=1}^{n_{comp}} q_i \right) \right] \frac{\partial T}{\partial t} = \frac{K_z}{\epsilon} \frac{\partial^2 T}{\partial z^2} - \frac{C_{p,g}}{R} \frac{\partial}{\partial z} (vP) - \frac{C_{p,g}}{R} \frac{\partial P}{\partial t} - \frac{1-\epsilon}{\epsilon} C_{p,a} T \sum_{i=1}^{n_{comp}} \frac{\partial q_i}{\partial t} + \frac{1-\epsilon}{\epsilon} \sum_{i=1}^{n_{comp}} \left( (-\Delta H_i) \frac{\partial q_i}{\partial t} \right) - \frac{2h_{in}}{\epsilon r_{in}} (T - T_w) \quad (2.9)$$

where  $\rho_s$  is the density of adsorbent,  $C_{p,s}$ ,  $C_{p,a}$ , and  $C_{p,g}$  are specific heat capacities of the adsorbent, adsorbed phase, and gas phase, respectively,  $K_z$  is effective gas thermal conductivity,  $\Delta H_i$  is heat of adsorption of component  $i$ ,  $h_{in}$  is the overall inside heat transfer coefficient,  $r_{in}$  is inner radius of the column and  $T_w$  is the wall temperature. The energy balance across the column wall is described by the following equation:

$$\rho_w C_{p,w} \frac{\partial T_w}{\partial t} = K_w \frac{\partial^2 T_w}{\partial z^2} + \frac{2r_{in}h_{in}}{r_{out}^2 - r_{in}^2} (T - T_w) - \frac{2r_{out}h_{out}}{r_{out}^2 - r_{in}^2} (T_w - T_a) \quad (2.10)$$

where,  $\rho_w$  is wall density,  $C_{p,w}$  is specific heat capacity of the column wall,  $K_w$  is thermal conductivity of the column wall,  $r_{out}$  is outer radius of the column and  $h_{out}$  is outside heat transfer coefficient between the wall and the water bath around the column, and  $T_a$  is water bath temperature. All model parameters and physical properties are listed in Table 2.1 (column 1).

Table 2.1: Parameters used in cycle simulations and optimizations.

Parameter	Value		Source
<b>Column properties</b>	<b>Column 1</b>	<b>Column 2</b>	
column length, $L$ [m]	0.32	0.062	measured
inner column radius, $r_{in}$ [m]	0.01805	0.0080	measured
outer column radius, $r_{out}$ [m]	0.02415	0.0095	measured
column void fraction, $\epsilon$	0.32	0.30	measured
particle voidage, $\epsilon_p$	0.35	0.35	assumed
tortuosity, $\tau$	3	3	assumed
<b>Properties and constants</b>			
universal gas constant, $R$ [m <sup>3</sup> Pa mol <sup>-1</sup> K <sup>-1</sup> ]	8.314		standard value
adsorbent particle density, $\rho_s$ [kg m <sup>-3</sup> ]	990		measured
column wall density, $\rho_w$ [kg m <sup>-3</sup> ]	7800		standard value
specific heat capacity, $C_{p,g}$ [J kg <sup>-1</sup> K <sup>-1</sup> ]	1041.3 (N <sub>2</sub> ), 895.63 (O <sub>2</sub> ) and 521.45 (Ar)		standard values
specific heat capacity of adsorbed phase, $C_{p,a}$ [J kg <sup>-1</sup> K <sup>-1</sup> ]	1041.3 (N <sub>2</sub> ), 895.63 (O <sub>2</sub> ) and 521.45 (Ar)		assumed
specific heat capacity of adsorbent, $C_{p,s}$ [J kg <sup>-1</sup> K <sup>-1</sup> ]	715.9		fitted
specific heat capacity of column wall, $C_{p,w}$ [J kg <sup>-1</sup> K <sup>-1</sup> ]	502		standard value
fluid viscosity, $\mu$ [kg m <sup>-1</sup> s <sup>-1</sup> ]	$1.801 \times 10^{-5}$ (N <sub>2</sub> ), $2.095 \times 10^{-5}$ (O <sub>2</sub> ), and $2.291 \times 10^{-5}$ (Ar)		standard values
molecular diffusivity, $D_m$ [m <sup>2</sup> s <sup>-1</sup> ]	$7.185 \times 10^{-5}$ (N <sub>2</sub> ), $7.481 \times 10^{-5}$ (O <sub>2</sub> ), and $7.614 \times 10^{-5}$ (Ar)		standard values
effective gas thermal conductivity, $K_z$ [J m <sup>-1</sup> K <sup>-1</sup> s <sup>-1</sup> ]	0.0903		assumed
thermal conductivity of column wall, $K_w$ [J m <sup>-1</sup> K <sup>-1</sup> s <sup>-1</sup> ]	16		standard value
inside heat transfer coefficient, $h_{in}$ [J m <sup>-2</sup> K <sup>-1</sup> s <sup>-1</sup> ]	15.2		fitted
outside heat transfer coefficient, $h_{out}$ [J m <sup>-2</sup> K <sup>-1</sup> s <sup>-1</sup> ]	1462.1		fitted

All the above equations were discretized in space using the finite volume technique by dividing the column into 30 cells. The WENO scheme, which is computationally efficient [58], was used to discretize the equations in space. The final set of ordinary differential equations (ODEs) were non-dimensionalized and solved using the *ode23s* solver provided in MATLAB.

## 2.4.2 Mass balance calculations

In order to calculate the amount of gas adsorbed on the solid in a particular breakthrough experiment, the experiments need to be run to completion, i.e. both thermal and mass transfer fronts should completely break through, and temperature of the thermal-bath is kept constant through out the experiment. Once this condition can be ensured, the following mass balance [59] around the adsorption column was used to calculate the loading from breakthrough experiments:

$$In - Out = Accumulation\ in\ the\ solid\ phase + Accumulation\ in\ the\ gas\ phase \quad (2.11)$$

Expressing the different terms we have:

$$\int_0^t \left( \frac{F_{in} P_{in} y_{in}}{RT_{in}} \right) dt - \int_0^t \left( \frac{F_{out} P_{out} y_{out}}{RT_{out}} \right) dt = V_b \rho_s (1 - \epsilon) q_{i,exp} + \frac{V_b \epsilon P_{avg} y_{in}}{RT} + \frac{V_d P_{avg} y_{in}}{RT} \quad (2.12)$$

where the first and the second terms on the left hand side are the number of moles of the adsorbate entering and leaving the column, respectively. The first term on the right hand side is the number of moles adsorbed in the solid phase and the second and the third terms are the accumulation in the void spaces of the column and in the dead volume of the breakthrough apparatus, respectively.  $F_{in}$  and  $F_{out}$  represent the volumetric flow rates measured by the flow controllers and flow meters at the column inlet and outlet, respectively,  $P_{in}$  and  $P_{out}$  are values of pressures measured at the column inlet and outlet,  $T_{in}$  and  $T_{out}$  correspond to the inlet and outlet temperatures, respectively, and  $y_{in}$  and  $y_{out}$  represent composition, of the gas phase at the inlet (cylinder composition) and outlet (measured using a mass spectrometer), respectively. On the right hand side of the equation,  $P_{avg}$  denotes the average (arithmetic mean of inlet and outlet) pressure measured at the end of an experiment. Since all the variables, except  $q_{i,exp}$ , are experimentally measured, Eq. 2.12 can be rearranged to calculate  $q_{i,exp}$ .

## 2.5 Results and discussion

### 2.5.1 Isotherm measurements

The measured adsorption isotherms are shown in Figure 2.2. All the three gases exhibited favorable isotherms with  $N_2$  showing the strongest adsorption followed by Ar and  $O_2$ . Ar and  $O_2$ , in fact showed only a modest non-linearity. The pure component loadings for all three gases were described by a classical single-site Langmuir isotherm:

$$q_i^* = \frac{q_{s,i} b_i c_i}{1 + b_i c_i} \quad (2.13)$$

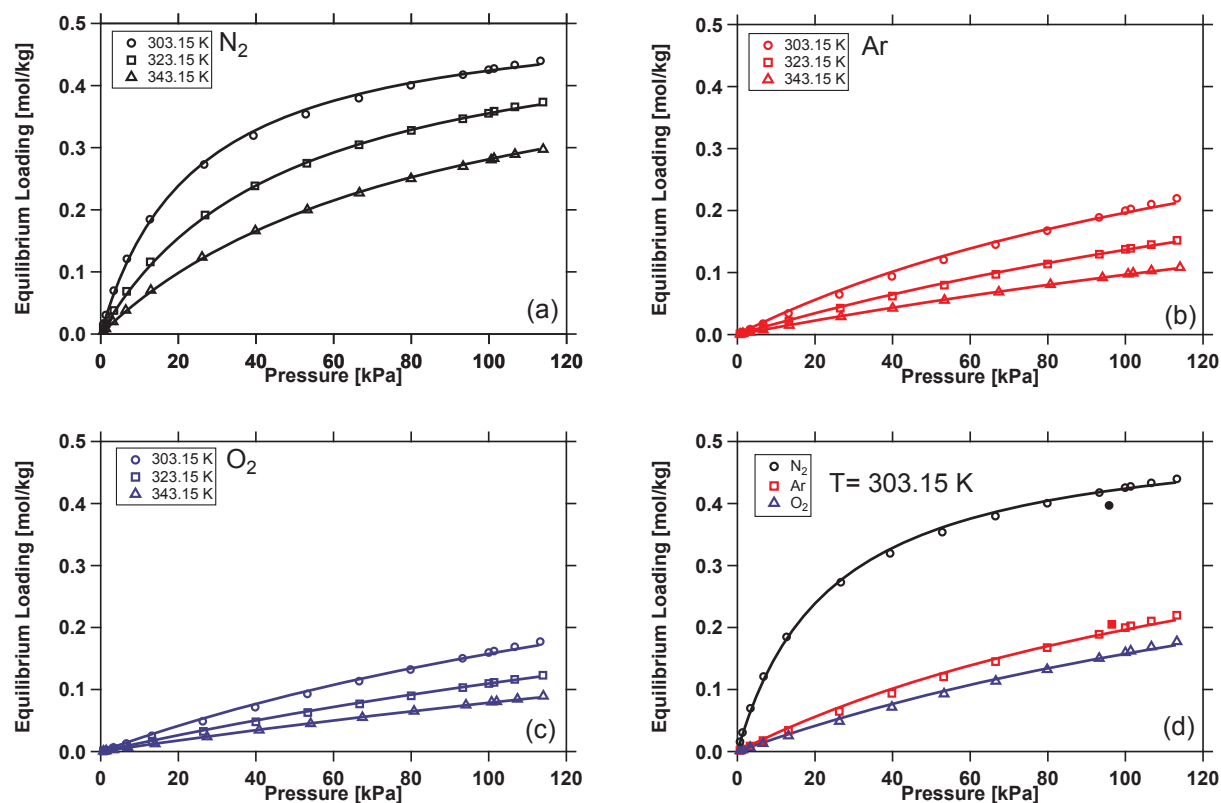


Figure 2.2: Single component adsorption isotherms of a)  $N_2$ , b) Ar, and c)  $O_2$  on Ag-ETS-10 extrudates. Symbols are experimental values and lines are fitted Langmuir model. (d) compares the isotherms of three gases at 303.15 K. Closed symbols in (d) are experimental loadings calculated from breakthrough experiments.

where  $c_i$  and  $q_i^*$  are the gas phase and equilibrium solid phase concentration of component  $i$ , respectively,  $q_{s,i}$  (mol/kg) is solid phase saturation capacity, and  $b_i$  is adsorption equilib-

Table 2.2: Fitted Langmuir adsorption parameters for N<sub>2</sub>, O<sub>2</sub>, and Ar on Ag-ETS-10.

Parameter	N <sub>2</sub>	Ar	O <sub>2</sub>
$b_0$ (m <sup>3</sup> mol <sup>-1</sup> )	$3.02 \times 10^{-6}$	$8.35 \times 10^{-6}$	$1.27 \times 10^{-5}$
$q_s$ (mol kg <sup>-1</sup> )	0.53	0.53	0.53
$-\Delta U_i$ (kJ mol <sup>-1</sup> )	26.34	18.82	16.93

rium constant of component  $i$  which follows the van't Hoff type temperature dependence:

$$b_i = b_{0,i} e^{\frac{-\Delta U_i}{RT}} \quad (2.14)$$

where  $U_i$  is the internal energy of component  $i$ . Equations 2.13 and 2.14 were fitted to the experimental points by varying  $q_{s,i}$ ,  $b_{0,i}$ , and  $\Delta U_i$ . The data were simultaneously fitted by constraining all gases to have identical saturation capacities. The fitted isotherm model parameters are listed in Table 2.2.

## 2.5.2 Breakthrough measurements

A series of breakthrough experiments were performed using various gas mixtures at different conditions. Pure N<sub>2</sub>, Ar, He, three O<sub>2</sub>/Ar mixtures (95% O<sub>2</sub>/5% Ar, 70% O<sub>2</sub>/30% Ar, and 50% O<sub>2</sub>/50% Ar), and dry air were used in this study. Pure component measurements were used to compare experimental loadings with those measured in the volumetric experiments. Binary and ternary experiments were performed to validate the prediction of competitive adsorption and to evaluate the effectiveness of the model to capture breakthrough profiles. Several runs were repeated to ensure that the results are reproducible.

## 2.5.3 Single-component breakthrough measurements

Figure 2.3(a) shows the breakthrough profile of pure N<sub>2</sub>, pure Ar, and 95% O<sub>2</sub>/5% Ar entering a column previously saturated with pure He at 95.0 kPa and 303.15 K. For safety reasons, it was not possible to work with pure O<sub>2</sub> and hence experiments using a mixture of 95% O<sub>2</sub>/5% Ar are described in this sub-section. The feed flow rate in all the runs was maintained at 150 ccm. Temperature profiles for the breakthrough experiments measured by the thermocouple located at 8 cm and 24 cm length from inlet are shown in Figure 2.3(b). In both figures, symbols and lines represent experimental data and simulated profiles, respectively. It can be observed that Ar leaves the column later than O<sub>2</sub> while N<sub>2</sub> is the strongest species and has the longest breakthrough time. This observation is in agreement with the isotherms shown in Figure 2.2. Figure 2.3(b) shows that N<sub>2</sub> has

the highest increase in temperature followed by Ar and O<sub>2</sub>. These results are consistent with the  $\Delta U_i$  values reported in Table 2.2. Using the mass balance given by Eqn 2.12, the solid phase loadings were calculated and are shown in Fig 2.2(d) as closed symbols. It can be seen that the loadings measured from static experiments are comparable to those from the breakthrough experiments although the N<sub>2</sub> loading from the breakthrough experiment was slightly lower than the loading measured by the volumetric method.

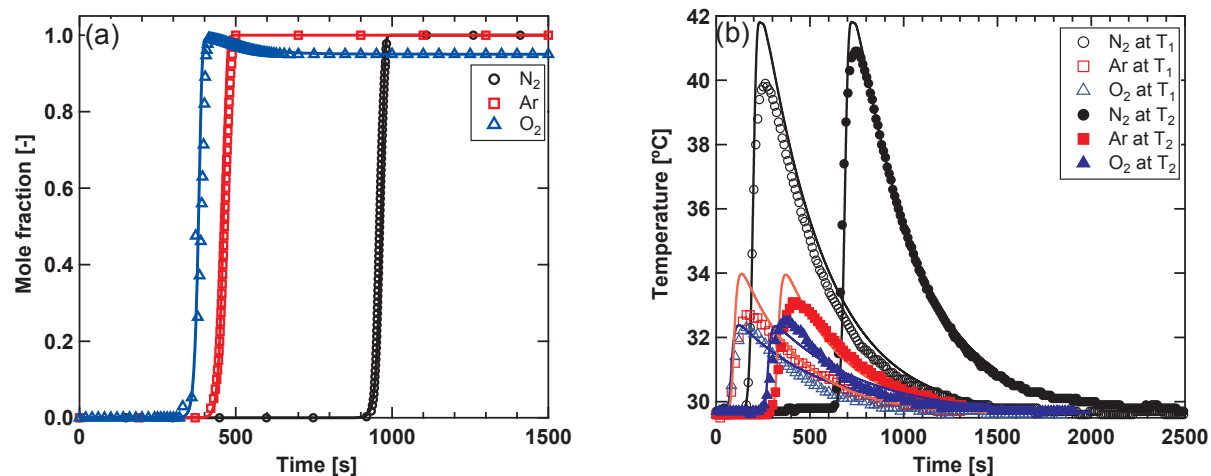


Figure 2.3: Adsorption breakthrough profiles for N<sub>2</sub>, Ar, 95% O<sub>2</sub>/5% Ar using He as the purge gas. Figure (a) shows breakthrough profiles measured at the column outlet; (b) shows corresponding temperature profiles measured by thermocouples 1 and 2 ( $T_1$  and  $T_2$ ). Symbols and lines correspond to experimental and simulation data, respectively. Experimental conditions:  $P_{\text{avg}}=95$  kPa,  $T_{\text{bath}}=303.15$  K,  $F_{\text{in}}=150$  ccm.

The model described in Section 3.1 was solved to provide the breakthrough curves and temperature profiles. Of all the model parameters used for simulation, only three parameters, namely  $h_{\text{in}}$ ,  $h_{\text{out}}$ , and  $C_{\text{ps}}$  were used as fitting parameters. The breakthrough experiment with pure N<sub>2</sub> was used to calculate the values of these parameters. The genetic algorithm (GA) subroutine in MATLAB global optimization toolbox was used for the fitting procedure. The objective of the fitting procedure was to minimize sum of the areas between the experimental and simulated curves for  $y_{\text{N}_2}$ ,  $T_1$ , and  $T_2$  as described by the following equation:

$$J = \frac{\int_0^t (y_{\text{out}}^{\text{exp}} - y_{\text{out}}^{\text{sim}}) dt}{\int_0^t y_{\text{out}}^{\text{exp}} dt} + \frac{\int_0^t (T_1^{\text{exp}} - T_1^{\text{sim}}) dt}{\int_0^t T_1^{\text{exp}} dt} + \frac{\int_0^t (T_2^{\text{exp}} - T_2^{\text{sim}}) dt}{\int_0^t T_2^{\text{exp}} dt} \quad (2.15)$$

The value of  $J$  was found to be 0.016 and the corresponding values of the fitting variables are reported in Table 2.1. The values of  $h_{\text{in}}$  and  $h_{\text{out}}$  were compared to standard correlations to ensure they are within the expected range. The inside heat transfer coefficient  $h_{\text{in}}$

was calculated to be  $13.35 \text{ J m}^{-2} \text{ K}^{-1} \text{ s}^{-1}$  from Leva's correlation [32] while the outside heat transfer coefficient  $h_{\text{out}}$  was calculated to be  $1207.1 \text{ J m}^{-2} \text{ K}^{-1} \text{ s}^{-1}$  from Churchill and Chu's correlation [60]. These values compare well with the fitted values reported in Table 2.1. Pinheiro et al. [61] have reported the value of  $C_{p,s}=800.0 \text{ J kg}^{-1} \text{ K}^{-1}$  for binderless ETS-10 particles which is comparable to the fitted value of  $715.9 \text{ J kg}^{-1} \text{ K}^{-1}$  used in this study for Ag-ETS-10 particles with the use of a binder.

In a separate attempt, the lumped mass transfer coefficient ( $k_i$ ) was included along with the other fitting parameters mentioned above. The value of  $k_i$  hence obtained was 35% larger than the value calculated from Eq. 2.6. However, the value of  $J$  in Eq. 2.15 improved only by 0.1%. This revealed that in the range of experiments, mass transfer had a minor impact. Therefore,  $k_i$  was described using macropore diffusion control for the rest of the simulations. Note that more studies are required to establish the mass transfer mechanism. However, ETS-10 has an 10-membered ring pore opening ( $8 \text{ \AA}$  pore size) compared to the molecular size of  $\text{N}_2$ ,  $\text{O}_2$ , and Ar which are all less than  $4 \text{ \AA}$ . Therefore, kinetic effects are less likely to influence the separation. Figure 2.3 shows the comparison of the experimental results with the simulated ones. The results reveal that the predictions of both composition and temperature are in good agreement with the experimental data. The slight roll-up in the oxygen profiles occurs due the competition between  $\text{O}_2$  and Ar since the feed mixture in this case contained 95%  $\text{O}_2$  and 5% Ar. This effect is well captured by the simulations.

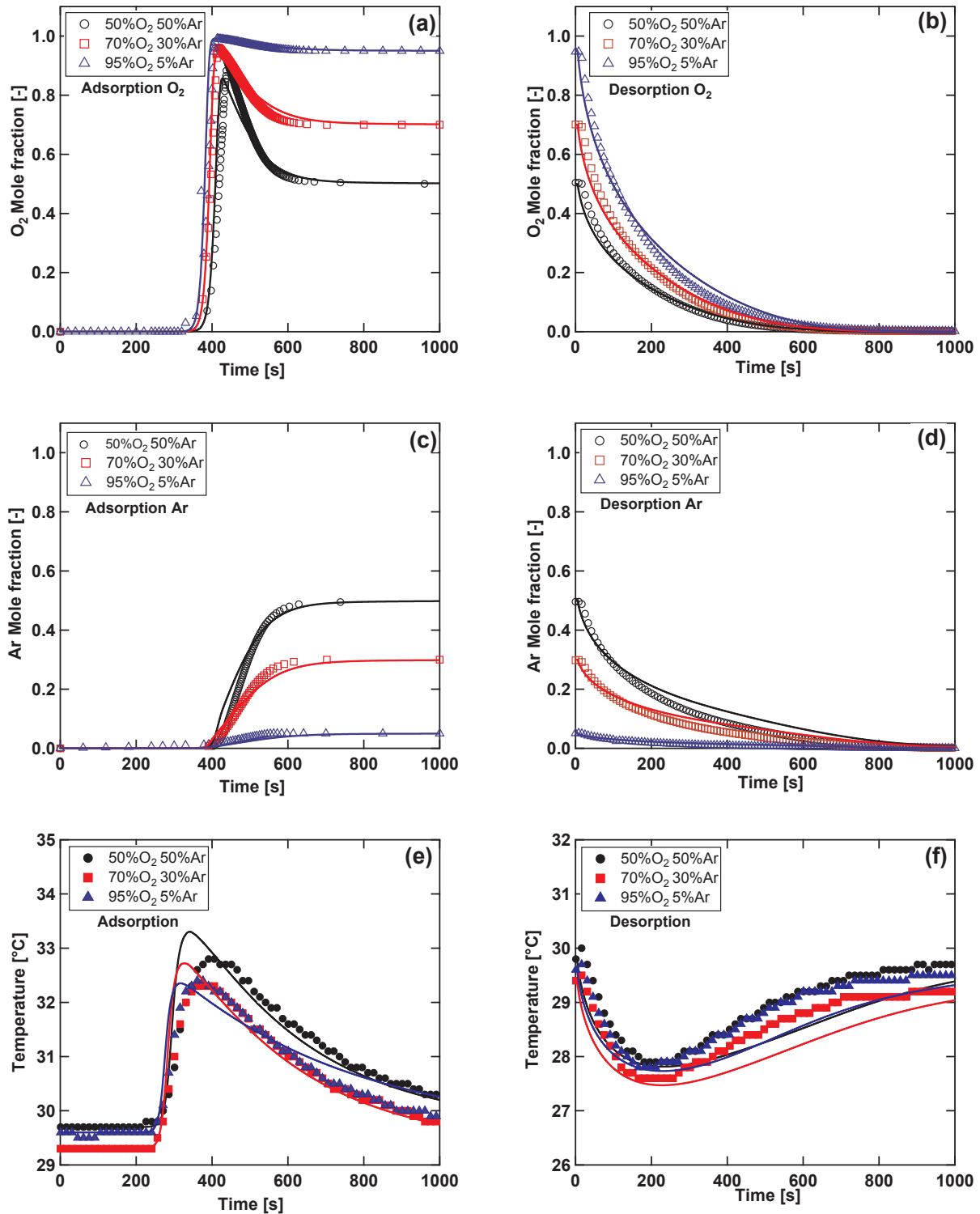


Figure 2.4: Breakthrough profiles with various compositions of  $O_2/Ar$  mixture using He as the purge gas. Profiles on the left column depict adsorption experiments while those on the right depict desorption experiments. Figures (a) and (b) show  $O_2$  profiles at the column outlet; (c) and (d) show corresponding Ar profiles; (e) and (f) show the temperature profile measured by thermocouple 2 ( $T_2$ ). Symbols and lines correspond to experimental and simulation data, respectively. Experimental conditions:  $P_{avg}=95$  kPa,  $T_{bath}=303.15$  K,  $F_{in}=150$  cm.

## 2.5.4 Binary breakthrough measurements

The advantage of the Ag-ETS-10 adsorbent is its ability to separate O<sub>2</sub> and Ar. Hence the next set of the experiments focuses on binary system of O<sub>2</sub> and Ar. Three different gas mixtures of O<sub>2</sub>/Ar were used for these runs. In the adsorption step, the column was initially saturated with He and the test gas was introduced to the column. Once the breakthrough was completed, the inlet stream was switched to He to initiate the desorption experiment. All the flows were maintained at 150 ccm and the experiments were conducted at 95.0 kPa and 303.15 K. Figure 2.4 shows adsorption and desorption profiles for these runs. The effect of competition between O<sub>2</sub> and Ar is clearly seen through roll-up of O<sub>2</sub> profiles in the adsorption step as shown in Figure 2.4(a). This effect is more evident when Ar mole fraction is higher since the competition between O<sub>2</sub> and Ar is more dominant compared to other compositions.

The experimental oxygen and argon equilibrium solid loadings were calculated using Eq. 2.12. In this study, the extended Langmuir isotherm:

$$q_i^* = \frac{q_{s,i} b_i c_i}{1 + \sum_{i=1}^{n_{comp}} b_i c_i} \quad (2.16)$$

was used to describe the competition between O<sub>2</sub> and Ar. The comparison of the experimental equilibrium loading (symbols) and those from the extended Langmuir model (lines) is shown in Figure 2.5. It can be seen the model is adequate in predicting the competitive loading over a wide range of compositions. Therefore, the extended Langmuir isotherm was used for describing the competitive behavior in all the simulations. The breakthrough runs were simulated and the results are shown in Figure 2.4. The model predictions are in good agreement with the experiments.

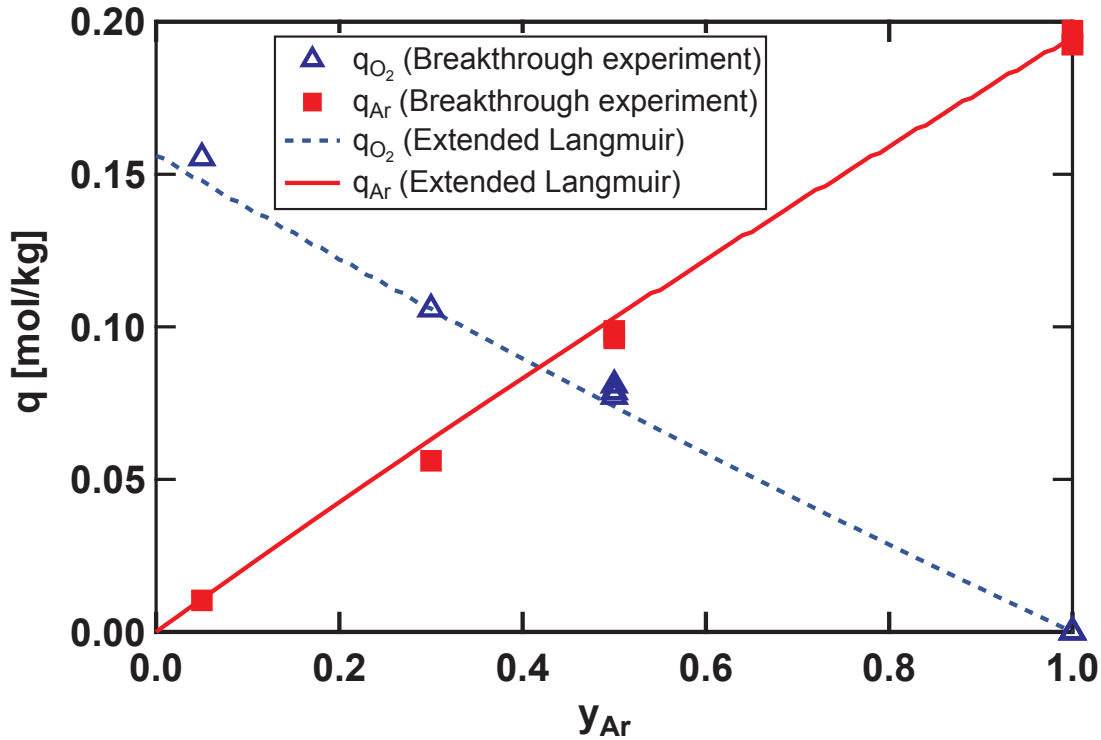


Figure 2.5: Binary  $O_2/Ar$  loading at 95 kPa and 303.15 K. Symbols are experimental data while lines are the calculated values using the extended Langmuir model.

In order to further explore the dynamics of the composition fronts the effect of changing the purge gas was investigated. Two different purge gases (He and Ar) were used in these experiments. Figure 2.6(a) shows the breakthrough profiles for the adsorption step. When He is used as a purge gas, a lighter component (He) is being displaced by a heavier mixture (95%  $O_2/5\%$  Ar). In this case, the adsorption front shows a step change, i.e. a shock front. However, when Ar (stronger component) is being displaced by 95%  $O_2/5\%$  Ar a simple wave is observed. The changes in the type of transition is an equilibrium effect caused by the competitive equilibrium between the gases [62]. Opposite trends compared to the adsorption step is seen in the desorption profiles as shown in Figure 2.6(b). This effect is also nicely reflected in the temperature profiles of the adsorption and desorption shown in Figures 2.6(c) and 2.6(d), respectively. For the case of He as the purge gas, the temperature profile shows a positive change during the adsorption step. However, when Ar is used as the purge gas, a negative change in the temperature is noticed. The trends are reversed in 2.6(d) where temperature increases slightly when Ar is used as the purge gas and it drops relatively more when 95%  $O_2/5\%$  Ar is displaced by He. The modeling results show a good match with the experiments.

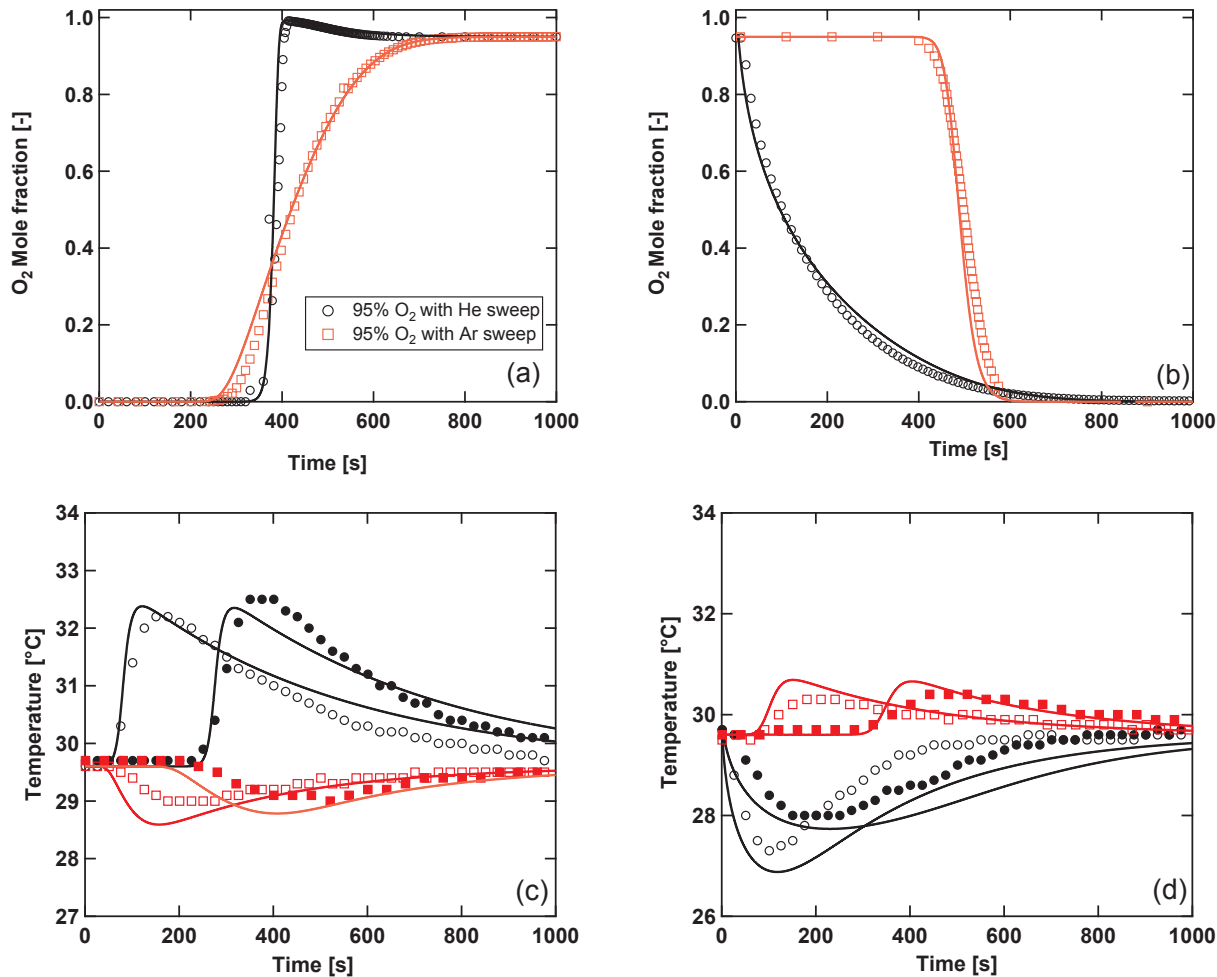


Figure 2.6: Breakthrough profiles for 95% O<sub>2</sub>/5% Ar using Ar and He as the purge gases. Profiles on the left column depict adsorption experiments while those on the right depict desorption experiments. Figures (a) and (b) show O<sub>2</sub> profiles at the column outlet; (c) and (d) show corresponding temperature profiles measured by thermocouples 1 and 2 ( $T_1$  and  $T_2$ ). Symbols and lines correspond to experimental and simulation data, respectively. Experimental conditions:  $P_{\text{avg}}=95$  kPa,  $T_{\text{bath}}=303.15$  K,  $F_{\text{in}}=150$  ccm.

## 2.5.5 Ternary breakthrough measurements

As a final step in the characterization, multi-component breakthrough profiles were studied. Figure 2.7(a) shows breakthrough profiles of N<sub>2</sub>, O<sub>2</sub>, and Ar for a column initially saturated with 95% O<sub>2</sub>/5% Ar and purged with pure N<sub>2</sub>. Once N<sub>2</sub> is introduced into the column, it displaces O<sub>2</sub> and Ar. The model is able to describe the competition between the three components well. The model captures the overshoot in the Ar breakthrough profile right before N<sub>2</sub> breakthrough. Figure 2.7(c) shows temperature profiles at  $T_1$  and

$T_2$  for this set of experiment. The rise in the temperature is about two degrees less than what was previously observed when  $N_2$  replaced He in Figure 2.3(b). The heat removed due to desorption of 95%  $O_2$ /5% Ar contributes to the lower temperature rise; an effect that is well captured by the model. Figure 2.7(b) and 2.7(d) show the desorption profiles when  $N_2$  is being displaced by a mixture of 95%  $O_2$ /5% Ar. The desorption profiles show a long-tail that is characteristic of a favorable isotherm.

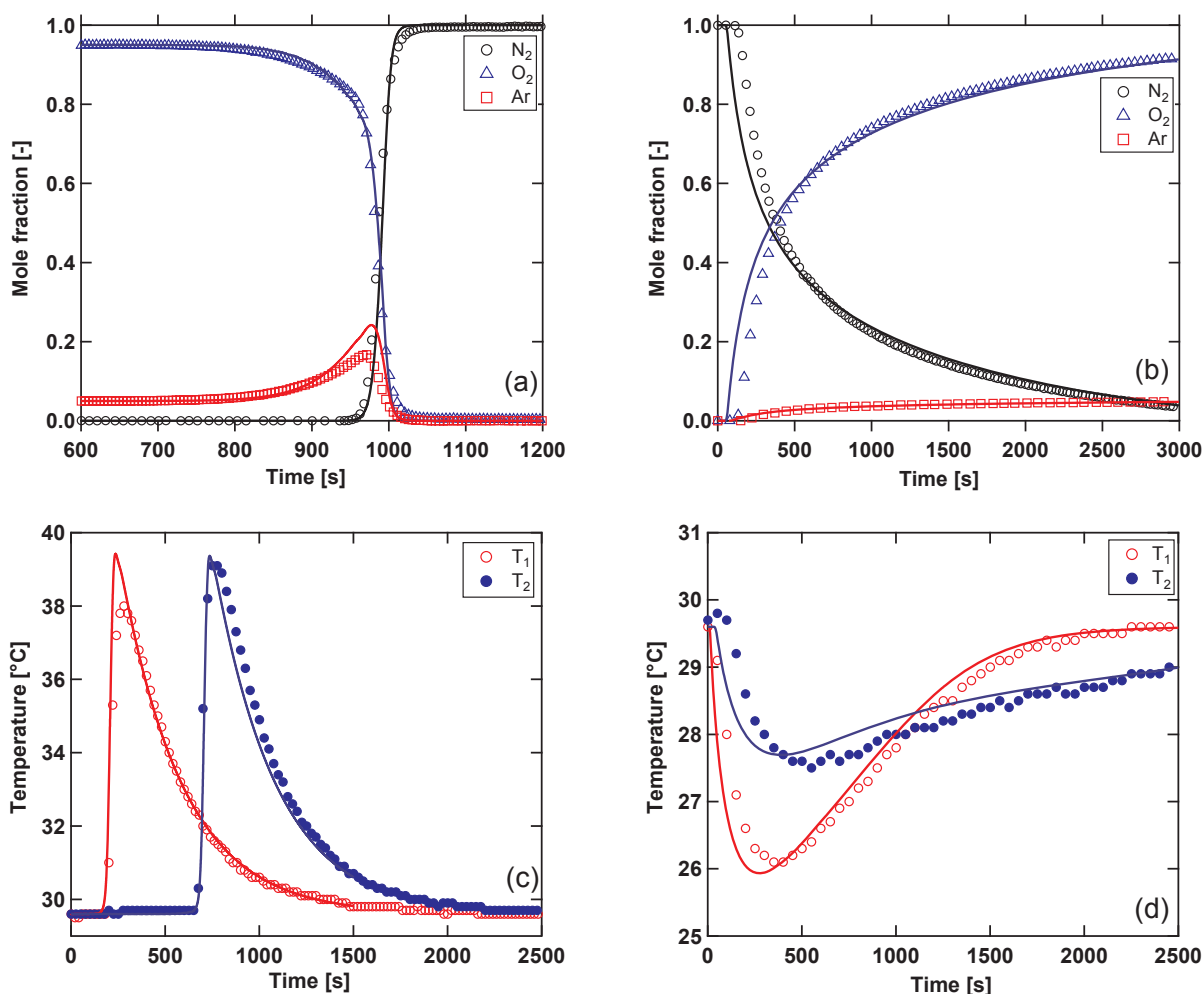


Figure 2.7: Breakthrough profiles for  $N_2$  using 95%  $O_2$ /5% Ar as the purge gas. Profiles on the left column depict adsorption experiments while those on the right depict desorption experiments. Figures (a) and (b) show component profiles at the column outlet; (c) and (d) show corresponding temperature profiles measured by thermocouples 1 and 2 ( $T_1$  and  $T_2$ ). Symbols and lines correspond to experimental and simulation data, respectively. Experimental conditions:  $P_{avg}=95$  kPa,  $T_{bath}=303.15$  K,  $F_{in}=150$  cm.

In the final set of experiments, the column is initially saturated with He, dry air (78.0%  $N_2$ , 21.0%  $O_2$ , 1.0% Ar) is introduced into the bed at  $t=0$ . The results of this experiment is

shown in Figure 2.8. The competition between  $O_2$  and Ar is clear as demonstrated by the roll-up in the  $O_2$  profiles. Once Ar starts breaking through, a decrease in  $O_2$  mole fraction in the outlet is observed. When  $N_2$  starts to breakthrough both  $O_2$  and Ar's composition fall to feed values. As it was described in pure component breakthrough tests,  $N_2$  is the last component to leave the column. Figure 2.8(c) and 2.8(d) show temperature profiles measured by the thermocouples located at 8 cm and 24 cm from column inlet. The first peak which is observed at thermocouple  $T_2$  is due to the adsorption of  $O_2$  and Ar while the second peak arises from  $N_2$  front and shows a higher temperature rise. The distance between the two peaks increases as the fronts move along the column. All the effects observed in the experiments are well described by the model except  $N_2$  breakthrough time. The predicted  $N_2$  breakthrough is slightly longer than the experimental value. This difference is probably due to the deactivation of a small portion of the bed at the inlet. This effect is also visible in the temperature profiles of adsorption where the rise at the first thermocouple is almost two degrees less than the one at the second thermocouple as shown in Figure 2.8(c).

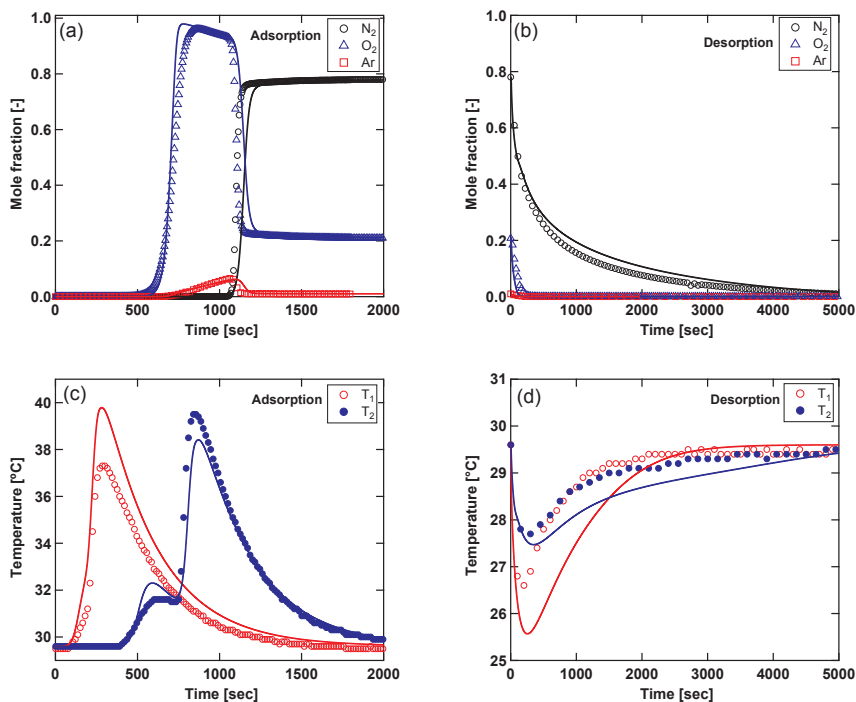


Figure 2.8: Breakthrough profiles for Air using He as the purge gas. Profiles on the left column depict adsorption experiments while those on the right depict desorption experiments. Figures (a) and (b) show component profiles at the column outlet; (c) and (d) show corresponding temperature profiles measured by thermocouples 1 and 2 ( $T_1$  and  $T_2$ ). Symbols and lines correspond to experimental and simulation data, respectively. Experimental conditions:  $P_{avg}=95$  kPa,  $T_{bath}=303.15$  K,  $F_{in}=150$  ccm.

## 2.6 Vacuum swing adsorption process for oxygen purification

In order to verify the capability of Ag-ETS-10 for high-purity O<sub>2</sub> production, a simple vacuum swing adsorption cycle was developed. It is important to stress that the purpose of this study is to demonstrate the ability to produce high-purity O<sub>2</sub> at a reasonable recovery using Ag-ETS-10. The process described here is simple and to provide excellent performances, more complex processes that could result in improved performance will be studied in an upcoming manuscript. At this stage, the well-known Skarstrom cycle was simulated using the approach described by Haghpanah et al. [58]. The cycle configuration and pressure profile are shown in Figure 2.9. This cycle consists of four different steps: adsorption at higher pressure  $P_H$ , evacuation at lower pressure  $P_L$ , light reflux or light product purge at  $P_L$ , and finally feed pressurization from  $P_L$  to  $P_H$ . We assume that a pre-purification stage to remove all the N<sub>2</sub> using an appropriate adsorbent [31] can be considered and the oxygen purification unit receives a feed containing 95% O<sub>2</sub>/5% Ar. Also, the feed stream needs to be dehumidified prior to entering the adsorption bed as humidity will reduce the performance of Ag-ETS-10. A suitable adsorbent, e.g., silica gel or Zeolite 3A can be used for this purpose. We will consider only the oxygen purification stage using Ag-ETS-10 for this study. The column dimensions and adsorbent properties are reported in Table 2.1 (column 1). The operating parameters are step times:  $t_{ADS}$ ,  $t_{EVAC}$ ,  $t_{LR}$ , and  $t_{FP}$ , the feed velocity  $v_F$ , and the low pressure  $P_L$ . This simple cycle, using a set of parameters reported in Figure 2.9, results in a raffinate stream containing 99.01% O<sub>2</sub> with recovery of 11.35 %. This simple cycle highlights the ability of Ag-ETS-10 to produce high-purity O<sub>2</sub> with reasonable recovery.

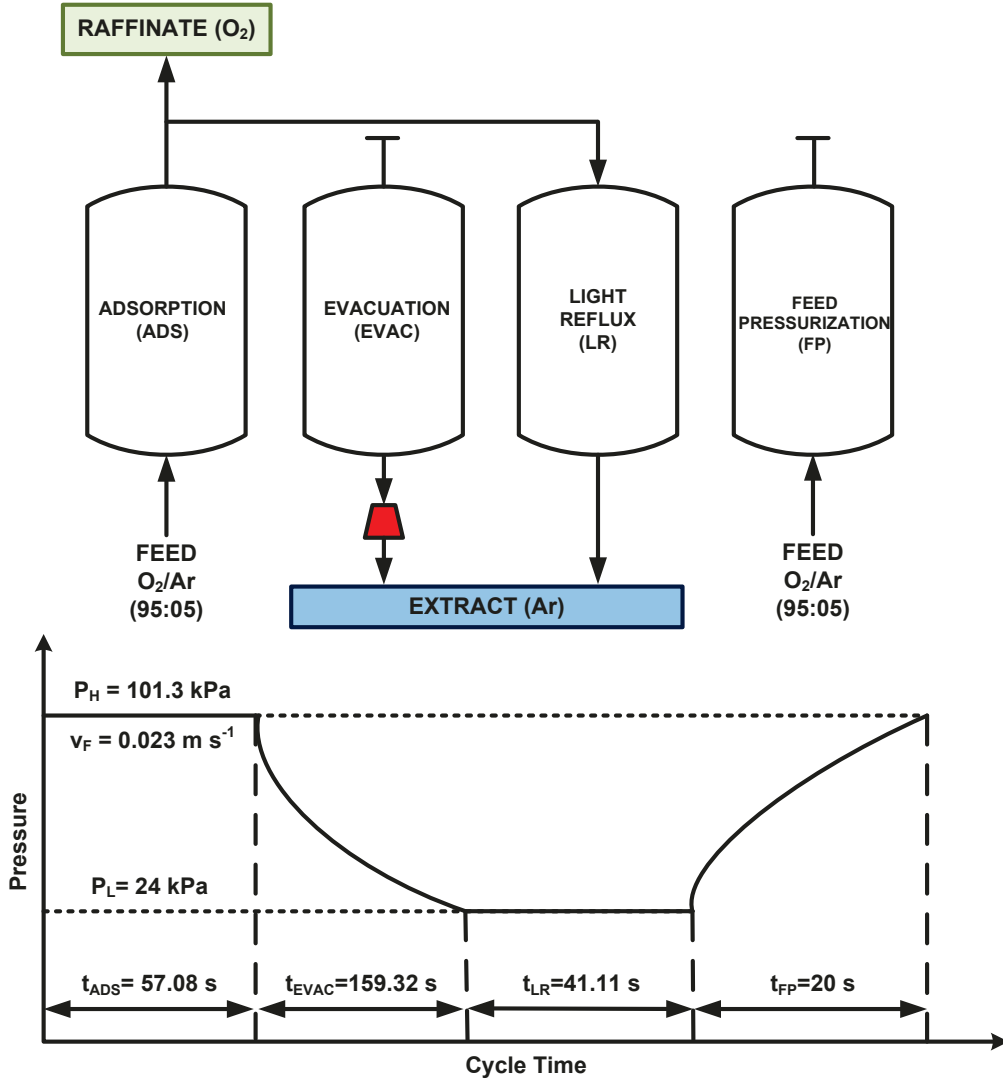


Figure 2.9: Cycle configuration and pressure profiles used in this study. The operating parameters shown are the ones used for the base case simulation.

The effect of  $P_L$  on the cycle performance was studied by keeping all other operating parameters fixed as reported in Figure 2.9. As shown in Figure 2.10(a), the value of purity increases with increasing  $P_L$ ; reaches a maximum; and then drops. However, the recovery consistently increases with increasing  $P_L$ . Figure 2.10(b) shows the corresponding gas phase axial profiles at the end of the adsorption step at cyclic steady state for three different values of  $P_L$ . As it can be seen, the gas phase mole fraction of  $O_2$  at the column outlet ( $\frac{z}{L} = 1$ ) for the cycle with  $P_L=0.24$  bar is the highest compared to the other two cycles followed with  $P_L=0.10$  bar and  $P_L=0.80$  bar, respectively. Figure 2.10(c) shows profiles of the Ar solid phase concentration at the end of the adsorption and pressurization steps for two different values of  $P_L$ . For  $P_L=0.1$ , the Ar front has almost reached the light

product end of the column at the end of the pressurization step and introducing more feed in the adsorption step will result in a substantial decrease in the purity. This can explain the trend observed for purity by changing  $P_L$  in Figure 2.10(a) and suggests smaller  $t_{\text{ADS}}$  or pressurizing with the light product will lead to higher  $\text{O}_2$  purity. This analysis suggests conducting parametric study for all operating parameters will be time consuming and may not always produce the optimal operating conditions. Therefore, a rigorous multi-objective optimization is required to further understand the effect of different operating parameters.

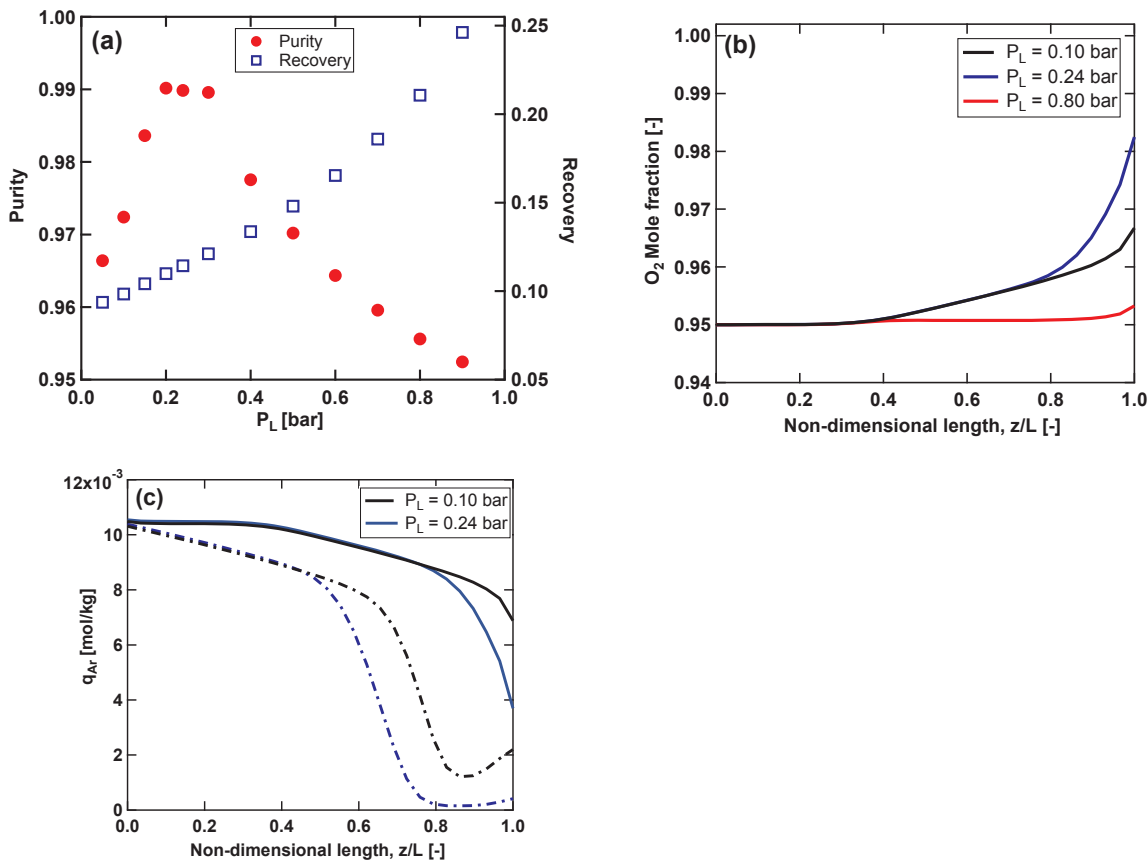


Figure 2.10: Effect of  $P_L$  on: (a) purity and recovery of  $\text{O}_2$ ; (b)  $\text{O}_2$  gas phase axial profiles of the Adsorption step; (c) Ar solid phase axial profiles of the Adsorption (solid line) and Pressurization (dashed line) steps in Skarstrom cycle.

A rigorous optimization of the Skarstrom cycle was performed to identify the optimal operating conditions. The non-dominated sorting genetic algorithm II [58] in MATLAB global optimization toolbox was used in the optimization procedure [63]. The objective functions were purity and recovery of  $\text{O}_2$  and the decision variables were  $t_{\text{ADS}}$ ,  $t_{\text{EVAC}}$ ,  $t_{\text{LR}}$ ,  $P_L$ , and  $v_F$ . The constraint  $t_{\text{LR}} < t_{\text{ADS}}$  was enforced. The ratio of  $\frac{t_{\text{LR}}}{t_{\text{ADS}}}$  provides an

indication of the reflux fraction. The high pressure  $P_H$  is fixed at 101.3 kPa and  $t_{FP}$  is fixed at 20 s since this is the realistic time for pressurization in an industrial scale. The bounds for all the decision variables are listed in Table 2.3. At this point, it is worth mentioning that the true measure of a process will be to assess its economic potential, e.g., energy consumption and productivity. This aspect is outside the scope of this work and will be addressed in a future communication.

Table 2.3: Range of decision variables used in the Skarstrom cycle simulation.

Decision variable	Range
$t_{ADS}$ [s]	20 – 100
$t_{EVAC}$ [s]	30 – 200
$t_{LR}$ [s]	2 – 100
$v_F$ [m s <sup>-1</sup> ]	0.005 – 0.5
$P_L$ [kPa]	3.04 – 60.78

The purity-recovery Pareto curve for this cycle is shown in Figure 2.11 (a). Each point on the Pareto curve corresponds to a set of decision variables and the trend between purity and recovery shows the trade-off range between the two objective functions. The Pareto curve indicates that a purity value in excess of 99.0% and 99.5% can be achieved at a recovery of 11.35% and 7.8%, respectively. Ferreira et al. [1] have reported 99.28% and 99.15% purities with 8.6% and 12.0% recovery, respectively, for a feed containing 95% O<sub>2</sub>/5% Ar using a more complicated cycle which includes pressure equalization and back fill steps. Figure 2.11(b) shows ratios of  $\frac{t_{LR}}{t_{ADS}}$  corresponding to the Pareto front in Figure 2.11(a). As expected, purity of O<sub>2</sub> in the product stream increases by increasing this ratio. This study shows that a simple Skarstrom cycle can be designed to obtain rather high-purity oxygen from a feed containing 95% O<sub>2</sub>. It is possible to improve the process performance by applying more complex cycles. This study will be reported in Chapter 4.

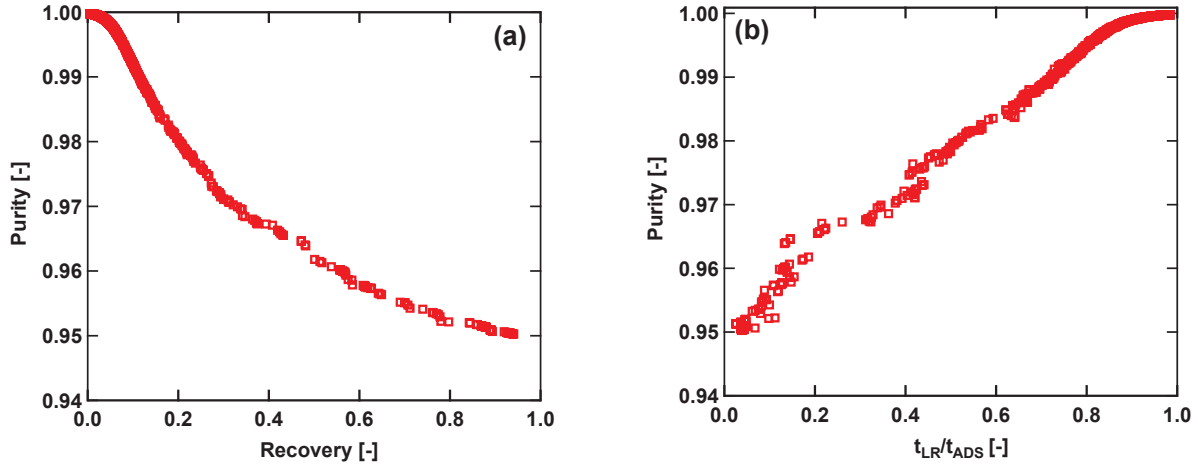


Figure 2.11: Results of process optimization to maximize  $O_2$  purity and recovery. (a) Pareto curve for the optimization of  $O_2$  purity and recovery in the Skarstrom VSA cycle; (b) Variation of purity as a function of  $\frac{t_{LR}}{t_{ADS}}$  for the Pareto points.

## 2.7 Conclusions

In this study, the possibility of high-purity  $O_2$  production using Ag-ETS-10 adsorbent was explored. Breakthrough profiles of various gas mixtures were measured using a laboratory scale dynamic column breakthrough apparatus to validate the large-scale performance of the adsorbent. Ag-ETS-10 has shown the capability to separate pure  $O_2$  from air since  $O_2$  is the lighter component on Ag-ETS-10 compared to  $N_2$  and Ar. These profiles have been modeled by writing detailed mass and energy balances. The model was able to predict experimental profiles of mole fraction and temperature well. Binary equilibrium of Ar/ $O_2$  was well predicted by single-site extended Langmuir model. A simple Skarstrom vacuum swing adsorption cycle was developed to further explore the capability of Ag-ETS-10 for high-purity  $O_2$  production from a feed containing 95%  $O_2$ /5% Ar. A parametric study on the effect of the low pressure  $P_L$  on the cycle performance suggested multi-objective optimization of the cycle to satisfy objective functions. This cycle was optimized and purity-recovery Pareto curves were obtained by using genetic algorithm. The results verify the ability of Ag-ETS-10 to produce high-purity  $O_2$  in excess of 99.0% with recovery of 11.35% using the simple Skarstrom VSA cycle.

## Chapter 3

# Dynamics of oxygen purification

Recent multi-component breakthrough experiments in our laboratory have shown that silver exchanged titanosilicates (Ag-ETS-10) have the potential to separate oxygen and argon based on their thermodynamic affinities. Understanding mass transfer and fluid transport dynamics of this separation process is important for process-scale design. In this work, breakthrough profiles of  $N_2$ ,  $O_2$ , and Ar and their mixtures on Ag-ETS-10 extrudates and granules have been measured using a laboratory scale dynamic column breakthrough apparatus. In order to investigate the dynamics of the mass transfer, effect of flow rate, temperature and pressure on the concentration and temperature profiles were studied. These experiments have been described by discretization of mass and energy balances using the finite volume technique. The model could predict the experimental profiles to a high level of precision. In a separate attempt,  $N_2$  breakthrough profiles on two columns filled with Ag-ETS-10 extrudates and granules with two different sizes were obtained. Influence of macropore, micropore, and film resistance and dispersion within the column was investigated based on these experimental results using fundamentals of mass transfer and fluid dynamics which assisted in classifying the dynamics of this separation. The experimental results verified the fast mass transfer nature of Ag-ETS-10 and its capability for high-purity  $O_2$  production at larger scales using rapid adsorption cycles with negligible mass transfer limitation.

## 3.1 Introduction

The demand for portable oxygen concentrators (POC) is growing worldwide [64]. The rise in the number of patents on portable medical oxygen concentrators in the last two decades reflects the interest in developing new materials as well as adsorption processes to separate and purify oxygen from air [65]. In addition to this, industries such as aerospace, semiconductors, military, and medical require the production of on-site oxygen with ultra-high purity ( $>99.5\%$ ) [20]. It has been demonstrated that adsorption processes offer more favorable process economics and meet the purity and throughput requirements for small-scale applications such as  $O_2$  purification [9]. The aim of designing more efficient separation processes that can achieve high  $O_2$  purities, entails the discovery of new adsorbent materials and novel design and development of highly-efficient pressure swing adsorption (PSA) processes. For instance, rapid pressure swing adsorption (RPSA) cycles can assist in improving the productivity of the desired component subjected to negligible mass transfer resistance in the adsorbent particles. In order to design efficient processes, a thorough understanding of the physical properties of the material, adsorption mechanism, momentum, heat, and mass transfer mechanisms of the separation should be attained.

Our previous study showed that silver-exchanged titanosilicates (Ag-ETS-10) have the ability to purify oxygen reaching purities in excess of 99.0% using the simple Skarstrom cycle [66]. Although our mathematical model was validated through single and multi-component dynamic column breakthrough (DCB) experiments, the purpose here is to provide a full description of the dominating mechanisms for this process and verify the validity of the assumptions made. It has been pointed out [67–69] that assumptions such as lumped mass and heat transfer coefficients require full experimental evidence and validation of the ability of the model to capture all the transport resistances in only one coefficient. Further, the study of operating conditions such as the flow rate, temperature, pressure, and particle size provides a full insight about the process dynamics and the conditions that favor the separation. On the other hand, it is also important to find the operating conditions that affect the process the most and the transport mechanism that dominates. For instance, particle size studies offer the necessary information about the dominant mass transfer resistance (micropore or macropore) in the adsorbent as well as the channeling and clustering within the column that can cause pressure drop and axial dispersion [64, 69].

In order to better understand the dynamics of the separation and the mechanisms that control the process, a series of experiments using our in-house dynamic column breakthrough (DCB) apparatus were carried out. The effect of flow rate, temperature, pressure, and particle size was studied. The results allowed us to conclude that the process is mainly

controlled by the equilibrium rather than mass transfer effects. All the experiments were modeled and simulated using a non-isothermal axially dispersed plug flow model which included all the transport effects. The simulations showed an agreement with the experimental results, which further confirmed the validity of the mathematical model and the assumptions used to describe the experimental data.

## 3.2 Materials and methods

### 3.2.1 Materials

Same batch of Ag-ETS-10 extrudates as in Chapter 2 were used in this Chapter. To study the particle size effect on the dynamics of adsorption, these extrudates were crushed to 0.5 mm granules. Prior to each set of experiments, the Ag-ETS-10 extrudates were activated for 16 hours at 523.15 K under a N<sub>2</sub> environment. All gases in this study (99.999% N<sub>2</sub>, 99.999% Ar, 99.999% He, 95.0% O<sub>2</sub>/5.0% Ar, and 50.0% O<sub>2</sub>/50.0% Ar) were obtained from Praxair Canada Inc.

### 3.2.2 Isotherm measurements

#### Low pressure isotherm measurements

In our previous study [66], low pressure (up to 115 kPa) isotherms were reported for N<sub>2</sub>, O<sub>2</sub>, and Ar for three different temperatures, namely 303.15, 323.15, and 343.15 K. These were adequately described by a single site Langmuir isotherm. Isotherms and the values of Langmuir isotherm parameters are provided in Figure 2.2 and Table 2.2.

#### High pressure isotherm measurements

In this work, since pressures higher than 115 kPa were studied, the adsorption isotherms of pure N<sub>2</sub>, O<sub>2</sub>, and Ar on Ag-ETS-10 were measured using a HPVA-100 high pressure volumetric unit from VTI instruments (Hialeah, FL). The samples were activated under the same conditions as in the low pressure isotherm measurements. The measured adsorption isotherms are shown in Figure 3.1. The pure component loadings were not adequately represented by the single site Langmuir isotherm. Hence, for all the three gases dual-site Langmuir isotherm was used:

$$q_i^* = \frac{q_{sb,i} b_i c_i}{1 + b_i c_i} + \frac{q_{sd,i} d_i c_i}{1 + d_i c_i} \quad (3.1)$$

where  $c_i$  and  $q_i^*$  are the gas phase and equilibrium solid phase concentration of component  $i$ , respectively,  $q_{sb,i}$  and  $q_{sd,i}$  (mol/kg) are the solid phase saturation capacity of the first and the second site, respectively.  $b_i$  and  $d_i$  are adsorption equilibrium constants of component  $i$  which follow the van't Hoff type temperature dependence:

$$b_i = b_{0,i} e^{\frac{-\Delta U_{b,i}}{RT}} \quad (3.2)$$

$$d_i = d_{0,i} e^{\frac{-\Delta U_{d,i}}{RT}} \quad (3.3)$$

where  $U_{b,i}$  and  $U_{d,i}$  are the internal energy of component  $i$  for site 1 and 2. Equations 3.1, 3.2, and 3.3 were fitted simultaneously to the experimental points by varying  $q_{sb,i}$ ,  $q_{sd,i}$ ,  $b_{0,i}$ ,  $d_{0,i}$ ,  $\Delta U_{b,i}$ , and  $\Delta U_{d,i}$ . The fitted isotherm model parameters are listed in Table 3.1.

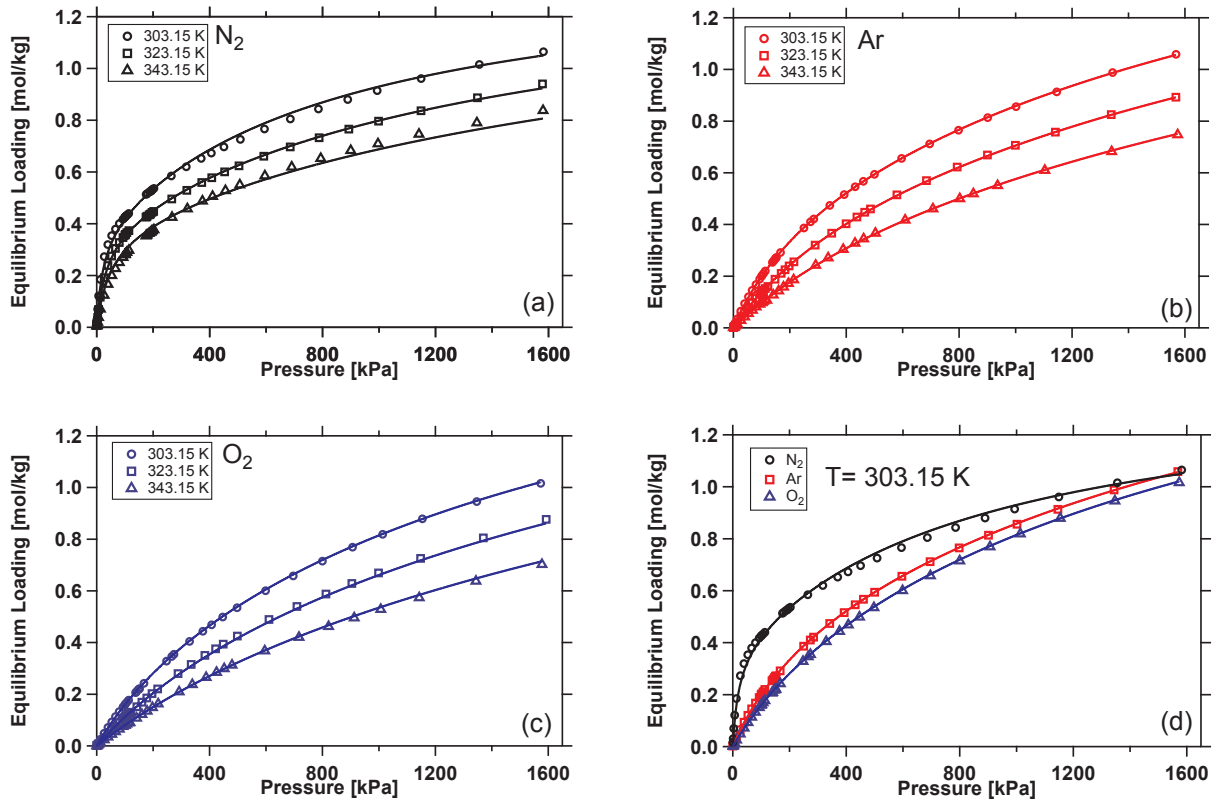


Figure 3.1: Single component high pressure adsorption isotherms of a) N<sub>2</sub>, b) Ar, and c) O<sub>2</sub> on Ag-ETS-10 extrudates. Symbols are experimental values and lines are fitted dual site Langmuir model. (d) compares the isotherms of three gases at 303.15 K.

Table 3.1: Fitted dual-site Langmuir adsorption parameters for N<sub>2</sub>, O<sub>2</sub>, and Ar on Ag-ETS-10 at high pressure.

Parameter	N <sub>2</sub>	Ar	O <sub>2</sub>
$b_{0,i}$ (m <sup>3</sup> mol <sup>-1</sup> )	$3.32 \times 10^{-6}$	$6.87 \times 10^{-6}$	$8.55 \times 10^{-6}$
$d_{0,i}$ (m <sup>3</sup> mol <sup>-1</sup> )	$2.42 \times 10^{-4}$	$1.18 \times 10^{-5}$	$1.42 \times 10^{-5}$
$q_{sb,i}$ (mol kg <sup>-1</sup> )	1.06	0.46	0.33
$q_{sd,i}$ (mol kg <sup>-1</sup> )	0.37	1.71	1.69
$-\Delta U_{b,i}$ (kJ mol <sup>-1</sup> )	17.06	18.41	17.22
$-\Delta U_{d,i}$ (kJ mol <sup>-1</sup> )	15.71	11.25	11.26

### 3.2.3 Model

A generic dynamic column breakthrough model described in the earlier publication [66] and in Chapter 2 was used in this study to simulate the adsorption breakthrough experiments. The equations used in the model were described earlier in the previous chapter. These equations were discretized in space using finite volume technique and the resulting ordinary differential equations were solved using the *ode23tb* solver provided in MATLAB. A similar approach to what has been discussed by Haghpanah et al [58], was used in this study to define the initial and boundary conditions for each of these steps.

## 3.3 Results and discussion

Four sets of experiments were conducted to study the effect of operating parameters such as the flow rate, temperature, pressure, and the adsorbent particle size on the breakthrough profiles. Same batch of Ag-ETS-10 was consistently used through out the parametric studies. In each of the sections below, only one parameter was changed while the other operating conditions were fixed. The objective of these experiments were to identify the importance of mass transfer effects, hydrodynamics of the column, and thermodynamics of the separation in determining the dynamics of this separation.

### 3.3.1 Effect of flow rate

The effect of three different flow rates on the adsorption breakthrough profiles of pure Ar and 50% O<sub>2</sub>/50% Ar mixture was explored. The column was initially purged with helium and the test gas was introduced to the column at flow rates of 150 ccm, 200 ccm, and 300 ccm. The composition of the outlet stream was measured with a mass spectrometer (Pfeiffer Vacuum OmniStar GSD 320, Asslar, Germany). All other instrumentations and

equipment used in this study were similar to the ones reported in Chapter 2. The column dimensions and adsorbent properties used in this section were also identical to those reported earlier [66] and are summarized in Table 2.1 (column 1).

Figures 3.2(a) and (c) show the corresponding breakthrough profiles and their first derivative for pure Ar experiments, respectively. The temperature profiles for the thermocouple located at 24 cm from the column inlet is also shown in Figure 3.2(e). As it can be seen, the model was able to predict the experimental profiles for all the three flow rates. Figure 3.2(c) indicates the concentration front was sharper for the higher flow rates which was possibly due to the larger Peclet numbers for higher flow rates (i.e. higher velocities). Peclet number is defined as:

$$Pe = \frac{vL}{D_L} \quad (3.4)$$

where  $D_L$  is the axial dispersion coefficient and is described by the following equation [32]:

$$D_L = 0.7D_m + 0.5vd_p \quad (3.5)$$

According to Eqs. 3.4 and 3.5, at higher velocities, Peclet number, i.e. ratio of convective to dispersive transport, is larger. Therefore the concentration profiles were sharper similar to what was observed in Figure 3.2(c). Macro/micropore diffusion resistances are not affected by the change in velocity of the feed if all other operating conditions are the same. The only other mass transfer resistance affected by the velocity of the fluid is the external film resistance.  $k_f$ , the external film resistance coefficient, is defined as [32]:

$$k_f = \frac{ShD_m}{2R_p} \quad (3.6)$$

where  $D_m$  and  $Sh$  are the molecular diffusion of the fluid and the Sherwood number, respectively. Sherwood number is calculated using the Wakao and Funazkri correlation [70]:

$$Sh = 2.0 + 1.1Sc^{1/3}Re^{0.6} \quad (3.7)$$

where  $Sc$  and  $Re$  are the Schmidt and Reynolds numbers, respectively. The former is independent of the fluid velocity while the latter increases at higher velocities. Therefore, according to Eqs. 3.6 and 3.7, once the flow rates of the fluid increases,  $k_f$  has a larger magnitude (i.e. less resistance) which results in sharper breakthrough profiles. However,

for the range of velocities used in these experiments, Sherwood number, defined as the ratio of the convective mass transport to the rate of diffusive mass transport, was around the lower limit of 2.0 predicted by Eq. 3.7. Hence, the change in the steepness of the breakthrough profiles was likely from the change in the hydrodynamics of the system rather than external film resistance. This observation was further verified by comparing the magnitude of dispersion and film resistance effects through parameter  $\delta$  [32]:

$$\delta = \left( \frac{1 - \epsilon}{\epsilon} \right) \left( \frac{3k_f}{R_p} \right) \left( \frac{D_L}{v^2} \right) \quad (3.8)$$

In the case of these experiments,  $\delta$  was in order of 500-2000 which essentially means axial dispersion had significantly larger contribution compared to the external film resistance [32].

The effect of flow rate was also investigated for a 50.0% O<sub>2</sub>/50.0% Ar mixture with the same range of inlet flow rates. The results for this set of experiments are shown in Figures 3.2(b), (d), and (f). Same effect as in the Ar experiments was observed for 50.0% O<sub>2</sub>/50.0% Ar feed. It is worth noting that higher purities of O<sub>2</sub> at the outlet was detected when the feed flow rate was larger. This effect was well captured by the model and was possibly due to the sharper O<sub>2</sub> concentration front traveling through the column at higher inlet velocity. As it can be observed in Figures 3.2(e) and (f), temperature rise in the thermocouple located at 24 cm from the inlet was larger at higher velocities which was possibly due to the larger contribution of the convective heat transfer at higher flow rates. The concentration and temperature profiles for the desorption runs for the same set of experiments are shown in Figure 3.3.

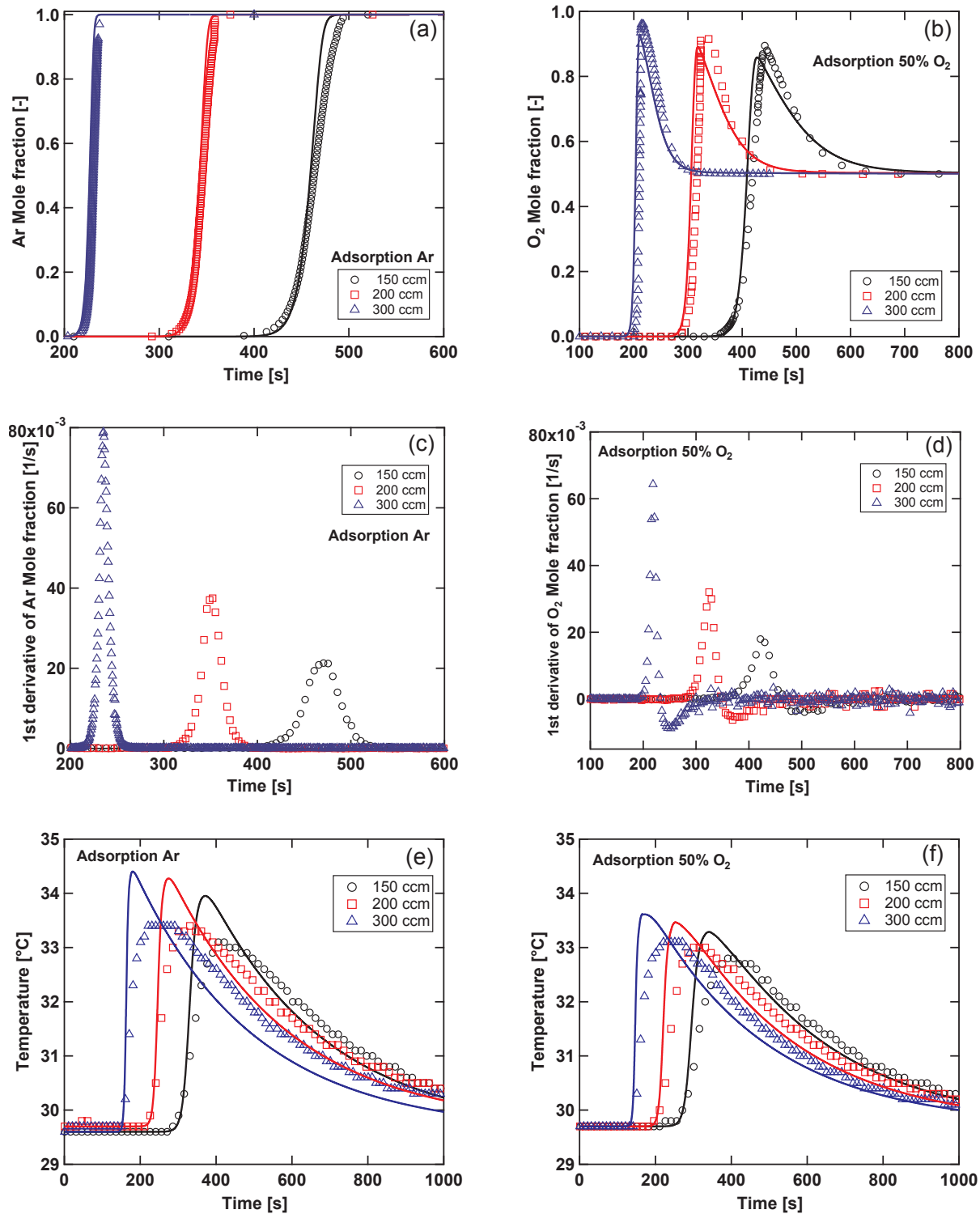


Figure 3.2: Effect of inlet flow rate on the breakthrough profiles for Ar and 50.0% O<sub>2</sub>/50.0% Ar. Figures (a) and (b) show concentration profiles at the column outlet; (c) and (d) show corresponding 1st derivative of the concentration profiles; (e) and (f) show corresponding temperature profiles measured by thermocouple 2 ( $T_2$ ). Symbols and lines correspond to experimental and simulation data, respectively. Experimental conditions:  $P_{\text{avg}}=95$  kPa,  $T_{\text{bath}}=303.15$  K.

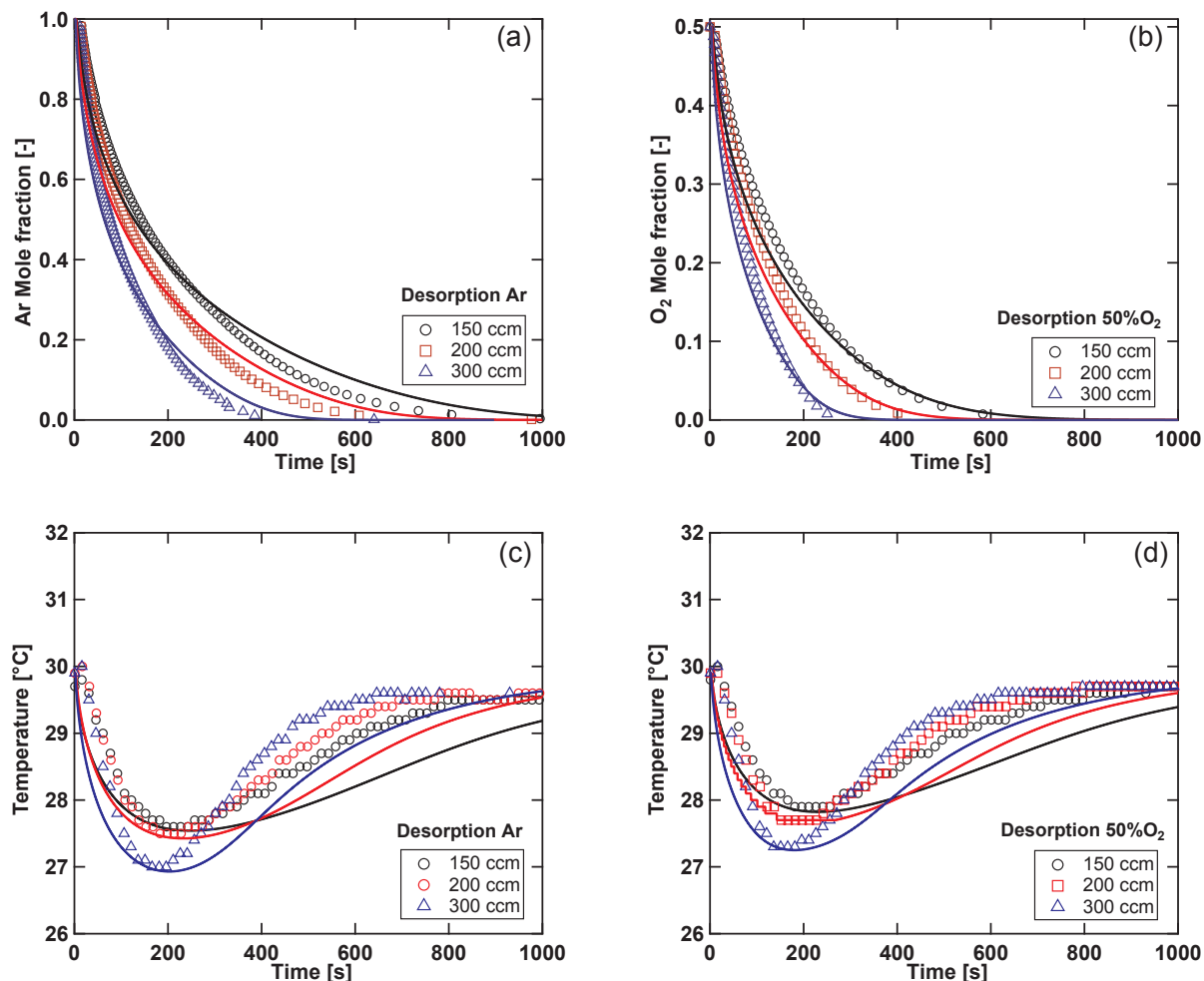


Figure 3.3: Effect of inlet flow rate on the desorption profiles for Ar and 50.0% O<sub>2</sub>/50.0% Ar. Figures (a) and (b) show concentration profiles at the column outlet; (c) and (d) show corresponding temperature profiles measured by thermocouple 2 ( $T_2$ ). Symbols and lines correspond to experimental and simulation data, respectively. Experimental conditions:  $P_{\text{avg}}=95$  kPa,  $T_{\text{bath}}=303.15$  K.

### 3.3.2 Effect of temperature

Second set of experiments were conducted to study the effect of temperature on the breakthrough profiles of pure N<sub>2</sub>, Ar, and 95.0% O<sub>2</sub>/5.0% Ar. Adsorption breakthrough experiments were conducted at 303.15 K, 313.15 K, and 323.15 K. The temperature of the experiments were controlled using a water circulation bath (PolyScience, Niles, Ill, USA). The inlet flow rate for all these experiments was kept constant at 150 ccm. The column dimensions used in this section were similar to the previous section and are summarized in Table 2.1 (column 1). Figures 3.4(a) to (c) present the concentration of the stream leaving

the adsorption column and the corresponding first derivative of the concentration and temperature profiles are shown in Figures 3.4(d) to (f) and Figures 3.4(g) to (i), respectively. As it can be observed in these figures,  $N_2$  breakthrough profiles were sharper at lower temperatures whereas the opposite trend was observed for Ar and  $O_2$  (i.e. sharper fronts at higher temperatures). The trend observed for  $N_2$  profiles was a clear thermodynamic effect due to the more nonlinear isotherms of  $N_2$  compared to the ones for Ar and  $O_2$ . If the mass transfer was the limiting phenomena, similar trends should have been observed for all the three gases by varying the temperature since the diffusion rate increases at higher temperatures. However, the components in this study present different behavior depending on their equilibrium properties. This observation indicated that shape of the breakthrough profiles in this set of experiments was governed by the thermodynamics of the process rather than mass transfer effects such as surface diffusion or macro/micropore diffusion. This was in alignment with the fact that ETS-10 ring pore opening is around 8 Å and is much larger compared to the molecular size of  $N_2$ ,  $O_2$ , and Ar which are all less than 4 Å. Therefore, kinetic effects are less likely to influence the separation and the capability of Ag-ETS-10 to be used in rapid pressure swing adsorption (RPSA) cycles was further verified. It is also worth noting that the experimental temperature profiles for the thermocouple located at 24 cm from the column inlet was well captured by the simulations as shown in Figures 3.4(g) to (i). The experimental concentration and temperature profiles of the desorption runs for the same group of experiments are shown in Figure 3.5 along with the model predictions.

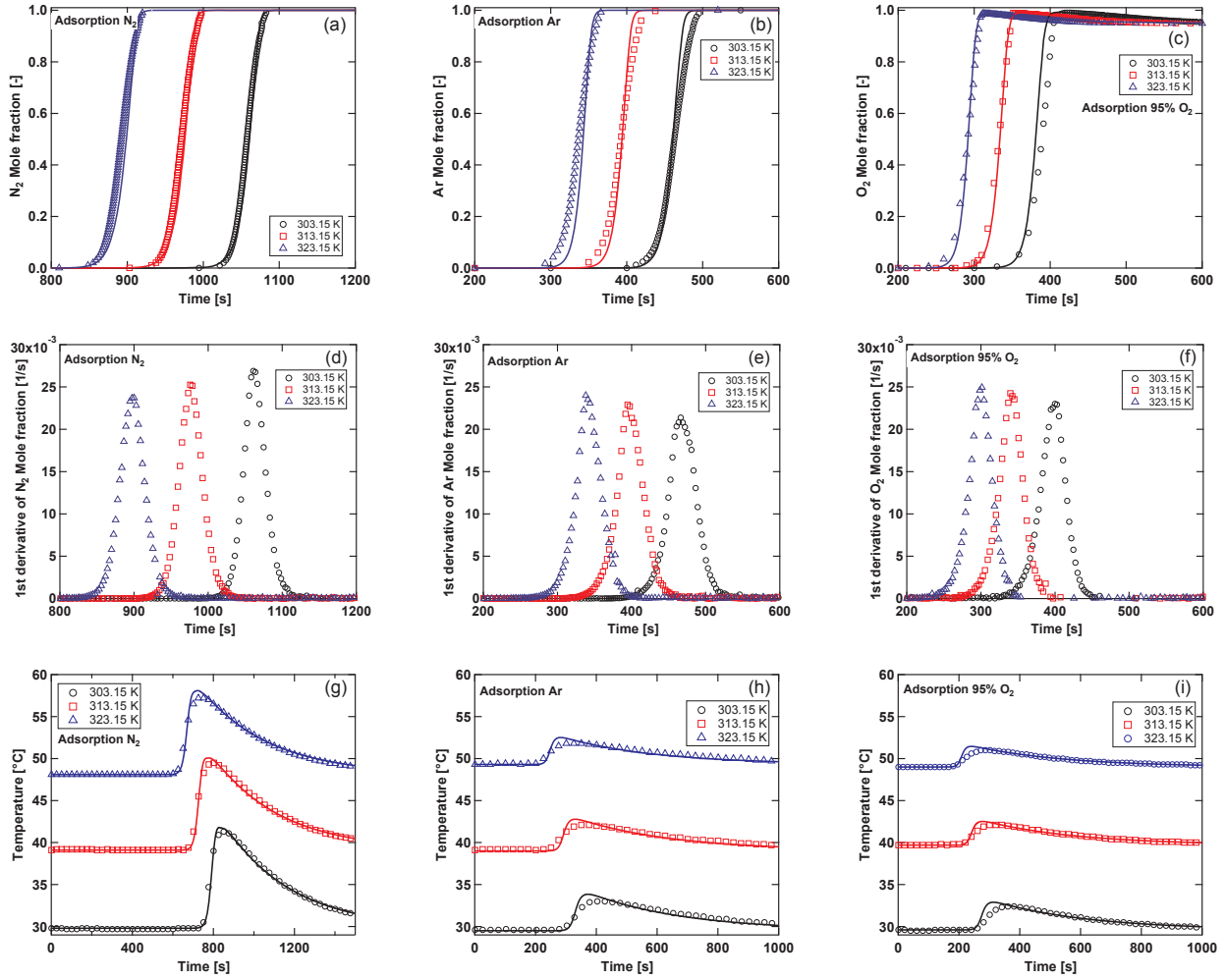


Figure 3.4: Effect of temperature on the breakthrough profiles for  $N_2$ , Ar and 95.0%  $O_2$ /5.0% Ar. Figures (a), (b), and (c) show concentration profiles at the column outlet; (d), (e), and (f) show corresponding 1st derivative of the concentration profiles; (g), (h), and (i) show corresponding temperature profiles measured by thermocouple 2 ( $T_2$ ). Symbols and lines correspond to experimental and simulation data, respectively. Experimental conditions:  $P_{avg}=95$  kPa,  $F_{in}=150$  ccm.

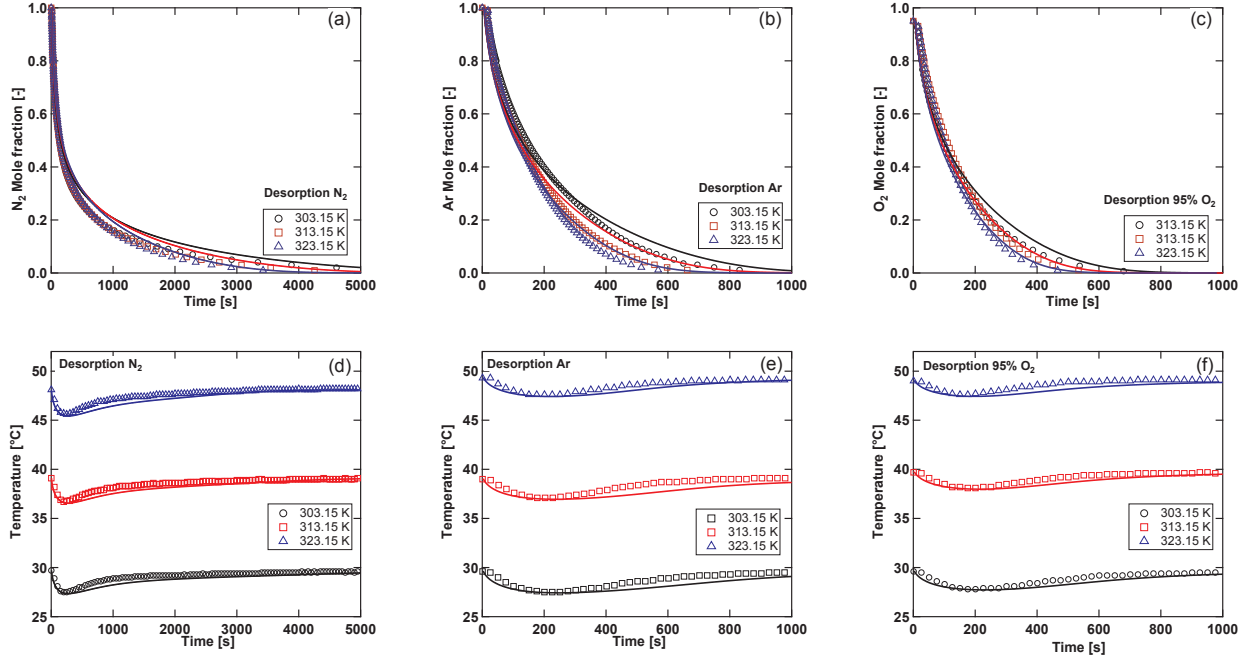


Figure 3.5: Effect of temperature on the Desorption profiles for  $N_2$ , Ar and 95.0%  $O_2$ /5.0% Ar. Figures (a), (b), and (c) show concentration profiles at the column outlet; (d), (s), and (f) show corresponding temperature profiles measured by thermocouple 2 ( $T_2$ ). Symbols and lines correspond to experimental and simulation data, respectively. Experimental conditions:  $P_{\text{avg}}=95$  kPa,  $F_{\text{in}}=150$  ccm.

### 3.3.3 Effect of pressure

In order to study the effect of operating pressure on the breakthrough profiles, the same batch of Ag-ETS-10 as in the previous sections was used. However, the cylindrical extrudates (1.2 mm diameter) were packed into a smaller column with the dimensions reported in Table 2.1 (column 2). Nitrogen breakthrough profiles were obtained at 96.5 kPa, 195.7 kPa, and 294.9 kPa while keeping the temperature and the flow rate constant at 303.15 K and 150 ccm, respectively. The corresponding breakthrough profiles at three different pressures and the first derivatives of the concentration profiles are shown in Figures 3.6(a) and (b), respectively. As expected, concentration front at higher pressures propagates faster along the column compared to the fronts at lower pressures which results in shorter breakthrough times. The minor discrepancies between the model predictions and the experimental data in Figure 3.6(a) was possibly resulting from the wall effects [71] due to the smaller ratio of bed diameter to the particle size compared to the previous sections where a bed with a larger diameter was used. Although molecular diffusion decreases with an increase in the operating pressure, but  $N_2$  breakthrough profiles were relatively sharper

at higher pressure as shown in Figure 3.6(b). This was a clear sign that similar to the experiments in the previous section, equilibrium effects dominated in these experiments rather than mass transfer effects. It is worth mentioning that according to Eq. 3.5, since  $D_m$  is smaller at higher pressures,  $D_L$  also decreases (i.e. larger Peclet numbers) and hydrodynamics of the separation could potentially make the concentration fronts steeper, in addition to the equilibrium effects. However, based on the observations in section 3.3.2, thermodynamics of the process seems to dominate in these experiments.

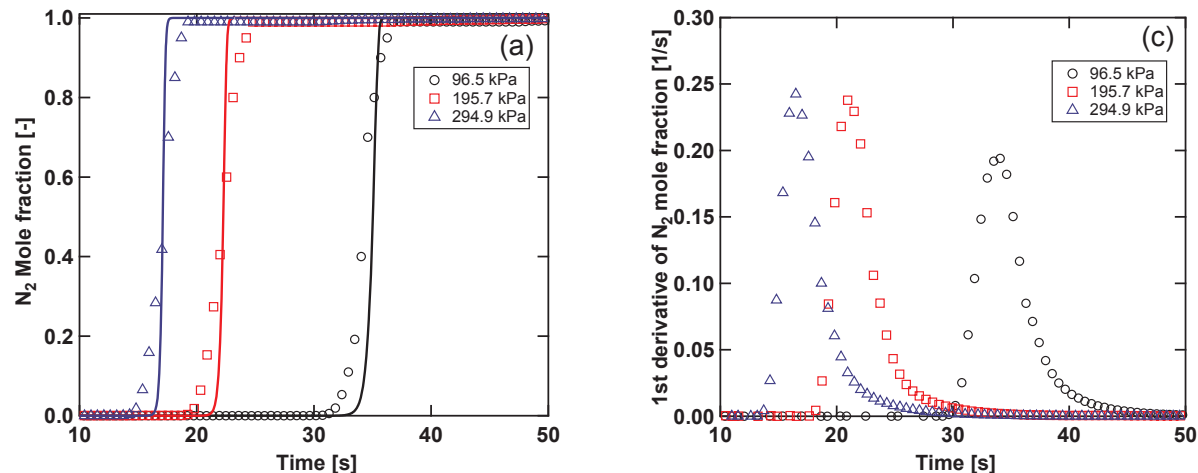


Figure 3.6: Effect of pressure on the breakthrough profiles for N<sub>2</sub>. (a) Concentration profile at the column outlet; (b) Corresponding 1st derivative of the concentration profile. Symbols and lines correspond to experimental and simulation data, respectively. Experimental conditions:  $T_{\text{bath}}=303.15$  K,  $F_{\text{in}}=150$  ccm.

### 3.3.4 Effect of particle size

The last group of experiments performed as a part of this study was to investigate the effect of particle size on the breakthrough profiles. The cylindrical extrudates ( $d_p = 1.2$  mm,  $L_p = 10$  mm), studied in the previous sections, were crushed to make granules with 0.5 mm diameter. Column 2 with the dimensions reported in Table 2.1 was packed with the same mass of Ag-ETS-10 granules as in the case of cylindrical extrudates and N<sub>2</sub> breakthrough profile at 303.15 K, 96.5 kPa, and 150 ccm feed flow rate was obtained. Figure 3.7(a) shows both of the breakthrough profiles for the crushed and un-crushed Ag-ETS-10 particles and the corresponding first derivatives are also shown in Figure 3.7(b). Figure 3.7(a) indicates that there was almost no change in the adsorption capacity of Ag-ETS-10 particles after the crushing since the breakthrough profiles lie exactly on top of each other. As shown in Figure 3.7(b), although sharper breakthrough profile was

obtained for the crushed granules, which was possibly due to the larger dispersion effects or smaller macropore mass transfer resistance in the granules compared to the cylindrical extrudates, this difference was too small to have a major effect on the performance of the process. In other words, this set of results along with the other experiments discussed in the previous sections, confirmed the fast mass transfer nature of the components of air within Ag-ETS-10 particles and further verified the capability of Ag-ETS-10 for high-purity O<sub>2</sub> production at larger scales using rapid VSA cycles with negligible mass transfer limitation.

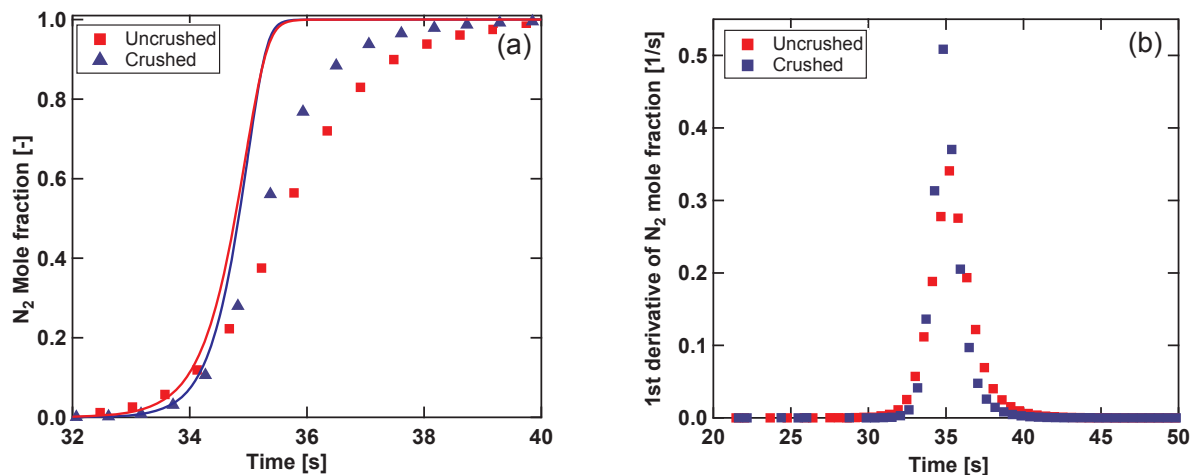


Figure 3.7: Effect of particle size on the breakthrough profiles for N<sub>2</sub>. (a) Concentration profile at the column outlet; (b) Corresponding 1st derivative of the concentration profile. Symbols and lines correspond to experimental and simulation data, respectively. Experimental conditions:  $P_{\text{avg}}=95$  kPa,  $T_{\text{bath}}=303.15$  K,  $F_{\text{in}}=150$  ccm.

### 3.4 Conclusions

In this work, the effects of flow rate, temperature, pressure, and particle size on the breakthrough profiles of N<sub>2</sub>, O<sub>2</sub>, and Ar and their mixtures on Ag-ETS-10 extrudates and granules were investigated using a laboratory scale dynamic column breakthrough apparatus. Finite volume technique was used to discretize the partial differential equations to model the experimental data. This model was able to predict the experimental concentration and temperature profiles. Using fundamentals of fluid dynamics and mass transfer, it was concluded that the sharper profiles obtained at higher inlet velocities were likely due to the change in the hydrodynamics of the system (i.e. larger Peclet numbers) rather than external film resistance. The effect of temperature on the breakthrough profiles was also studied and the result indicated that the shape of the concentration fronts were governed

by the equilibrium rather than mass transfer effects. The same conclusion was reached by exploring the effect of pressure on  $N_2$  breakthrough profiles. In a separate attempt,  $N_2$  concentration profiles on two columns filled with Ag-ETS-10 extrudates and granules with two different sizes were obtained. Although a minor effect of particle size was observed, it was concluded that mass transfer through Ag-ETS-10 particle is less likely to dominate the separation process and Ag-ETS-10 has the potential for high-purity  $O_2$  production at larger scales under rapid adsorption cycles since mass transfer resistance is almost negligible.

## Chapter 4

# Cycle development and process optimization

Producing oxygen with purity of higher than 95.0% from atmospheric air (78.0% N<sub>2</sub>, 21.0% O<sub>2</sub> and 1.0% Ar) is challenging because of similar physical properties of oxygen and argon. Silver-exchanged titanosilicates (Ag-ETS-10) have shown the potential to separate these gases based on their thermodynamic affinities. In this study, various vacuum swing adsorption (VSA) cycle configurations including the simple Skarstrom cycle and more complicated 6-step VSA cycles were simulated using mathematical models to maximize O<sub>2</sub> purity and recovery. The simulations were verified by conducting simple 3-step and the Skarstrom vacuum swing adsorption (VSA) cycle experiments. A mixture of 95.0%/5.0% O<sub>2</sub>/Ar feed was considered in the simulations and a rigorous multi-objective optimization was conducted to maximize O<sub>2</sub> purity and recovery. The simulations predicted 27.3% recovery for a product with 99.5% purity for a 6-step cycle with pressure equalization and light product pressurization steps. The recovery for the same level of purity was improved significantly to 91.7% by implementing a heavy product pressurization step. The effect of bed length on O<sub>2</sub> purity and recovery and the comparison of VSA with pressure swing adsorption (PSA) and pressure-vacuum swing adsorption (PVSA) for high-purity O<sub>2</sub> production were also investigated. Rigorous multi-objective optimizations were conducted to maximize oxygen productivity and minimize energy consumption of the VSA cycles, while meeting different purity constraints, and significant improvement in the performance indicators was obtained through process optimization.

## 4.1 Introduction

On-site high-purity oxygen production has attracted the attention of researchers due to the many applications such as in medical, semi-conductor, military, and aerospace industries [1, 4–8]. Separating O<sub>2</sub> from air (78.0% N<sub>2</sub>, 21.0% O<sub>2</sub>, 1.0% Ar) is already industrialized by using either cryogenic distillation or adsorption processes. However, due to the similar physical properties of O<sub>2</sub> and Ar such as the molecular size, boiling point, and adsorption affinity, producing ultra-high purity O<sub>2</sub>, i.e. with purities above 99.0%, is challenging. Conventional zeolites reported for air separation, such as zeolite 5A or LiLSX, do not show O<sub>2</sub>/Ar selectivity and can only produce product with around 95.0% O<sub>2</sub> purity [10–15]. Oxygen production based on the difference in the diffusion rates of Ar and O<sub>2</sub> has also been reported and widely studied in the literature [10, 16, 17]. Silver-free [18] and Silver-exchanged adsorbents, have opened the path for high-purity O<sub>2</sub> production using equilibrium-based adsorption processes [19, 20, 23–27]. To the best of our knowledge, silver-exchanged titanosilicate adsorbents (Ag-ETS-10) have shown the highest Henry’s selectivity (1.49) reported for Ar over O<sub>2</sub> [21, 22]. Table 1.1 summarizes the values of selectivity reported in literature for O<sub>2</sub>/Ar separation. In our earlier publication [66], the performance of Ag-ETS-10 extrudates for this separation was verified by an extensive dynamic column breakthrough study and the Skarstrom vacuum swing adsorption cycle simulation for a feed containing 95.0% O<sub>2</sub>/5.0% Ar. An optimized vacuum swing adsorption (VSA) Skarstrom cycle verified the ability of Ag-ETS-10 to produce O<sub>2</sub> in excess of 99.0% with recovery of 11.35%.

Kinetic-based separation using carbon molecular sieves (CMS) has also been extensively studied by Jee et al. using a two-bed pressure swing adsorption (PSA) with various cycle configuration and a three-bed pressure-vacuum swing adsorption (PVSA) with two consecutive blowdown steps [8, 29]. Sircar has reported a single-stage VSA O<sub>2</sub> purification with zeolite 13X [28]. Single-bed PSA with Ag-Mordenite as the adsorbent have been also studied by Knaebel and Kandybin [23]. High-purity O<sub>2</sub> production using Ag-LiLSX has been proposed by Air Products both in simulation [30] and experimental [26] works. Ferreira et al. reported experimental and process simulation of O<sub>2</sub> production in a single-stage [31] and dual-stage [1] PVSA using AgLiLSX. Table 1.2 shows a summary of O<sub>2</sub> purity and recovery obtained from P/VSA processes using various sorbents. It is important to note that except the study by Jee et al. [8], the recoveries obtained in these studies have been modest, i.e. less than 14.2 %, This is typical for separations where an adsorbent with modest selectivity is used while requiring a high purity. Hence, the applications of adsorptive O<sub>2</sub> separation is likely to be in niche areas where on-site O<sub>2</sub> generation is required. However, for large-scale applications cryogenic separation is likely

to be preferred.

In this study, the Skarstrom cycle along with two 6-step cycles were extensively studied. Cycle simulations were verified by comparing the experimental purity and recovery from simple 3-step and Skarstrom cycles with the predicted values from the simulations. The effect of bed length on the optimized purity-recovery Pareto fronts was investigated. Vacuum swing adsorption (VSA) Skarstrom cycle was compared with pressure swing adsorption (PSA) and pressure-vacuum swing adsorption (PVSA) Skarstrom cycles and the purity-recovery Pareto curves were compared with each other. In order to improve the recovery of O<sub>2</sub>, two more advanced cycles: a 6-step with pressure equalization (PE) and light product pressurization (LPP) steps; and a 6-step with pressure equalization (PE) and heavy product pressurization (HPP) steps, were also considered in this study. Finally, a series of energy-productivity optimizations were conducted for all the three cycles and the corresponding Pareto fronts were obtained for different purity levels of O<sub>2</sub> in the product stream. The main focus of this study is to further investigate the capability of Ag-ETS-10 for high-purity O<sub>2</sub> production by simple cycles currently available in the market and to design new cycle configurations in order to improve the performance indicators such as O<sub>2</sub> recovery, productivity, and total energy consumption of the cycle.

## 4.2 Materials and methods

### 4.2.1 Materials

The Ag-ETS-10 extrudates characterized in Chapters 2 and 3 with the properties reported in Table 2.1 were used in this chapter. The sample used in this study has been repeatedly used for the past three years in our laboratory and no deterioration has been observed.

### 4.2.2 Isotherm measurements

#### Low pressure isotherm measurements

In Chapter 2, low pressure (up to 115 kPa) isotherms were reported for N<sub>2</sub>, O<sub>2</sub>, and Ar for three different temperatures, namely 303.15, 323.15, and 343.15 K. These were adequately described by a single site Langmuir isotherm model. Isotherms and the values of Langmuir isotherm parameters are provided in Table 2.2 and Figure 2.2.

#### High pressure isotherm measurements

In this chapter, since pressures higher than 115 kPa were studied, the adsorption isotherms

of pure  $N_2$ ,  $O_2$ , and Ar on Ag-ETS-10 were measured using a HPVA-100 high pressure volumetric unit from VTI instruments (Hialeah, FL). The samples were activated under the same conditions as in the low pressure isotherm measurements. The measured adsorption isotherms are shown in Figure 3.1. The pure component loadings were not adequately represented by the single site Langmuir isotherm. Hence, for all the three gases dual-site Langmuir isotherm was used. The fitted isotherm model parameters are listed in Table 3.1.

### 4.2.3 Vacuum swing adsorption cycles

The model introduced in Chapter 2 was used in this section for the cycle simulations and optimizations. Three different raffinate cycles were considered in this study for  $O_2$  purification. In Chapter 2, the simple 4-step Skarstrom cycle was considered as the first approach to purify oxygen with a feed stream of 95.0%  $O_2$  and 5.0% Ar. The purity-recovery Pareto curve was obtained and purities in excess of 99.0% and 99.5% at corresponding recoveries of 11.35% and 7.8%, respectively, were achieved. The cycle configuration and pressure profile of the Skarstrom cycle are shown in Figure 4.1(a). In this cycle, adding the light product reflux (LR) step assisted in improving the purity. However, in order to improve the recovery of the cycle, two more complex cycles were considered in the current study. A 6-step cycle with pressure equalization (PE) and light product pressurization (LPP) steps [20], as shown in Figure 4.1(b), was considered. The third cycle, proposed in this study, is a 6-step cycle with pressure equalization (PE) shown in Figure 4.1(c). However, instead of pressurizing with the light product stream (raffinate), heavy product stream (extract) is used to pressurize the column. In addition to this, light reflux step is eliminated in this cycle in order to reduce oxygen loss in the extract stream. Purity-recovery and energy-productivity Pareto curves for all these three cycles have been compared and the results will be discussed in section 4.4. The column dimensions and adsorbent properties used in the simulation were identical to those reported earlier [66] and are summarized in Table 2.1 (column 1).

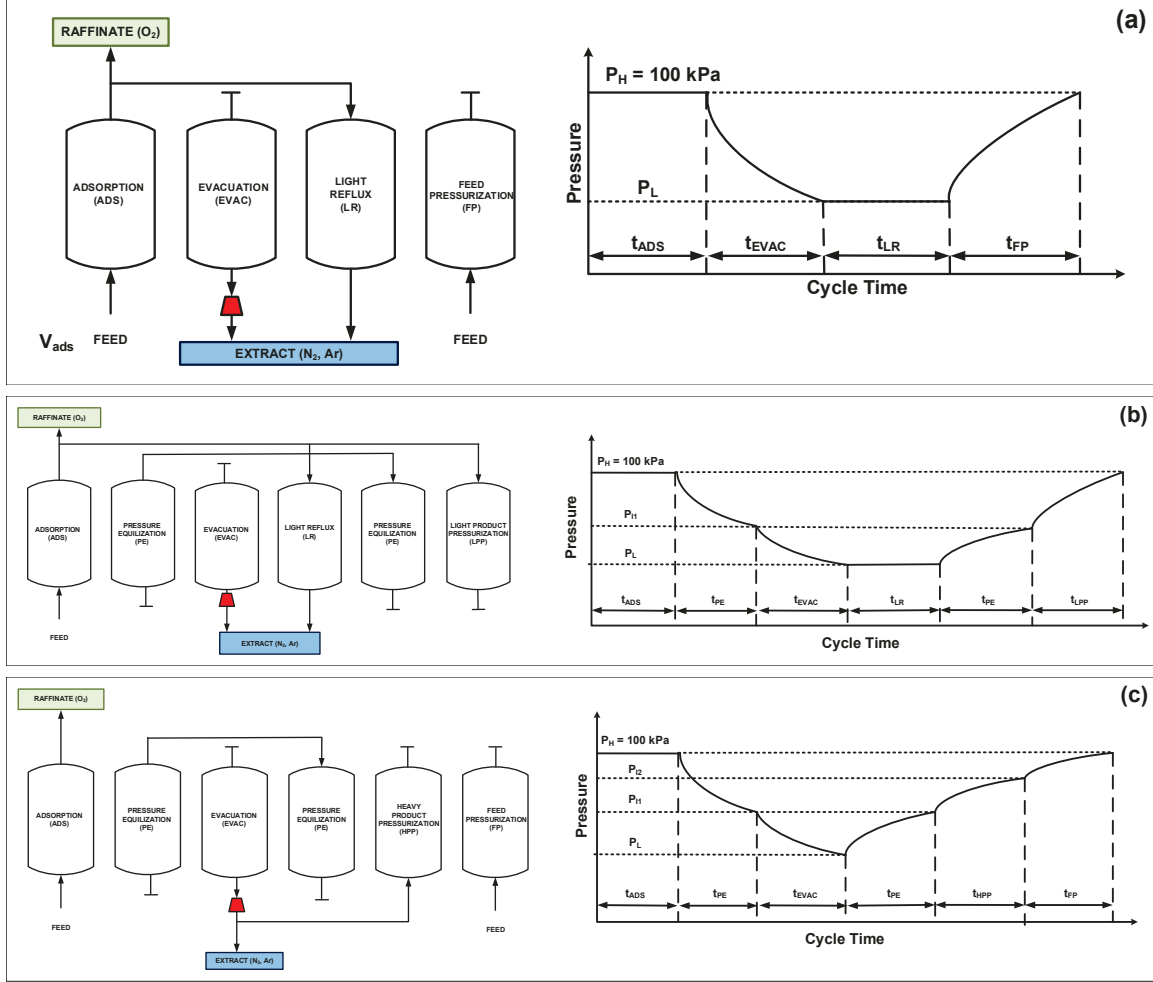


Figure 4.1: Cycle configuration and pressure profiles of the adsorption cycles: (a) Skarstrom (b) 6-step with PE and LPP (c) 6-step with PE and HPP.

#### 4.2.4 Constituent steps

**Adsorption (ADS):** During this step feed stream is introduced to the column at  $z = 0$  at high pressure  $P_H$  and 303.15 K with feed velocity of  $v_{ads}$ . The stronger components ( $N_2$  and Ar) are preferentially adsorbed and the lighter component ( $O_2$ ) leaves the column at  $z = L$ .

**Evacuation (EVAC):** In this step the product end of the column ( $z = L$ ) is closed and the column is depressurized with a vacuum pump from  $P_H$  to low pressure  $P_L$ . The stream leaving this step is rich in the stronger component(s).

**Light Reflux (LR):** A part of the raffinate stream is refluxed to the column from the light product end during this step in order to improve the purity of the product. Therefore,

the duration of this step is related to the adsorption step through  $t_{LR} \leq t_{ADS}$ . The pressure during this step is kept constant at  $P_L$ .

**Feed pressurization (FP):** In this step the column end at  $z = L$  is closed and the column is pressurized with the feed stream from  $P_L$  to  $P_H$ .

**Pressure equilization (PE):** This step involves two columns, a donor and a receiver. The pressure in the the donor column is reduced from  $P_H$  to intermediate pressure  $P_I$ . On the other hand, the receiver column is pressurized from  $P_L$  to  $P_I$ . Since  $P_H$  is fixed at 100 kPa for all the VSA cycle simulations in this study, in order to satisfy the mass balance constraints, i.e. the mass leaving the donor column should be equal to the mass entering the receiver column,  $P_I$  should be calculated based on the value of  $P_L$  chosen by the optimizer when initiating the simulations.

**Light product pressurization (LPP):** In this step the column end at  $z = 0$  is closed and the column is pressurized with a portion of the raffinate stream from the adsorption step from  $P_I$  to  $P_H$ . The maximum duration of this step is set to  $t_{ADS} - t_{LR}$ . Once the pressure within the column is equal to  $P_H$ , the adsorption step will be initiated. If this stream is not sufficient enough to pressurize the column, the column will go through a feed pressurization step.

**Heavy product pressurization (HPP):** In this step the column end at  $z = L$  is closed and the column is pressurized from  $P_I$  to  $P_H$  with a fraction of the heavy product stream leaving the evacuation step. Therefore, the duration of this step is related to the evacuation step through  $t_{HPP} \leq t_{EVAC}$ . Once the pressure within the column is equal to  $P_H$ , the adsorption step will be initiated. If this stream is not sufficient enough to pressurize the column, the column will go through a feed pressurization step. The main idea here is to avoid losing  $O_2$  in the stream leaving the evacuation step by refluxing a portion of it to the column and hence, increasing  $O_2$  recovery.

#### 4.2.5 Cycle optimization

Non-dominated sorting genetic algorithm II (GA) in MATLAB global optimization toolbox was used to identify the optimal operating conditions for each of the VSA cycles discussed in section 4.3.2. The population size was set to be 24 times the number of decision variables and the GA was set to run up to 50 generations. All optimizations reported in this study were performed on a desktop workstation with two 12-core INTEL Xeon 2.5GHz processors and 128GB RAM. Parallelization toolbox in MATLAB was used to enhance the speed of computations. It is worth noting that for each combination of deci-

sion variables the performance indicators. e.g., purity, recovery, were calculated using the detailed model starting from an initial condition and simulating the transition of a single column from one step to another until cyclic steady state is reached.

The first set of optimizations were conducted to optimize the operating conditions of each of the three cycles to maximize the purity and recovery. The common decision variables between the cycles were the durations of adsorption and evacuation steps ( $t_{\text{ADS}}$ ,  $t_{\text{EVAC}}$ ), pressure at the evacuation step ( $P_{\text{L}}$ ), and velocity of the feed ( $v_{\text{F}}$ ). The bed length ( $L$ ) was considered as a decision variable for a parametric study for the Skarstrom cycle. The duration of the light reflux step ( $t_{\text{LR}}$ ) was considered as one of the decision variables for the Skarstrom and 6-step with PE and LPP cycles. The duration of the pressure equalization step ( $t_{\text{PE}}$ ) was also included in the optimization of the 6-step with PE and LPP and the 6-step cycle with PE and HPP cycles. However, it did not show a significant effect on the optimization of purity and recovery. For the 6-step cycle with PE and HPP, duration of the heavy product pressurization step ( $t_{\text{HPP}}$ ) was also considered as a decision variable. The aim of the purity-recovery optimizations was to minimize the following two objective functions:

$$\begin{aligned} J_1 &= \frac{1}{Pu_{\text{O}_2}}, \\ J_2 &= \frac{1}{Re_{\text{O}_2}} \end{aligned} \tag{4.1}$$

$Pu_{\text{O}_2}$  and  $Re_{\text{O}_2}$  are oxygen purity in the product stream and oxygen recovery of the cycles, respectively and are defined as:

$$\begin{aligned} Pu_{\text{O}_2} &= \frac{n_{\text{O}_2}^{\text{Product}}}{n_{\text{total}}^{\text{Product}}} \\ Re_{\text{O}_2} &= \frac{n_{\text{O}_2}^{\text{Product}}}{n_{\text{O}_2}^{\text{Feed}}} \end{aligned} \tag{4.2}$$

where  $n$  is the number of moles collected in the corresponding stream. The second set of optimization runs were carried out in order to maximize productivity and minimize total energy consumption of the cycles under a certain  $\text{O}_2$  purity. The decision variables were similar to the purity-recovery optimizations. However, in this optimization, the objective functions were defined as the following to ensure purity constraints are met:

$$\begin{aligned}
J_1 &= A \left[ En \right] + B \left[ \max(0, Pu_{\text{const}} - Pu_{\text{O}_2}) \right]^2, \\
J_2 &= \frac{C}{Pr} + D \left[ \max(0, Pu_{\text{const}} - Pu_{\text{O}_2}) \right]^2
\end{aligned}
\tag{4.3}$$

$Pr$  and  $En$  are oxygen productivity and total energy consumption of the VSA cycles, respectively.  $Pu_{\text{const}}$  is the purity constraint for the energy-productivity optimizations. The constraints used in this study were 99.0%, 99.5%, and 99.8%, respectively.  $A$ ,  $B$ ,  $C$ , and  $D$  are the penalty functions to ensure the purity target is achieved. For most of the applications, which require high-purity oxygen, the level of the purity is the major constraint. Therefore, recovery was not set as a restriction for energy-productivity optimizations. Additionally, optimizing the operating conditions for a better productivity will indirectly force the optimizer to achieve higher recoveries.

## 4.3 Results and discussion

### 4.3.1 Experimental cycle demonstration

The dynamic column breakthrough apparatus described in our earlier publication [66] was modified such that simple VSA cycle experiments could be conducted using a single column. The schematic diagram of the apparatus is shown in Figure 4.2. Multiple manual two-way and three-way valves were added in order to switch flow directions between the steps in each cycle. A stainless steel tank (Swagelok, Solon, OH, USA) was added after the column to store part of the stream leaving the adsorption step and reflux the gas stored to the column during the light reflux step (LR). This design assisted in performing the Skarstrom cycle experiments with only one column. The vacuum pump used in this study was an air-operated vacuum pump (McMaster-Carr, Illinois, USA). All other instrumentations and equipments depicted in Figure 4.2 were similar to the ones reported earlier [66]. All the experiments were done at 293.15 K and high pressure during the adsorption step ( $P_{\text{H}}$ ) was fixed at 100 kPa. It is worth noting that all the valve switchings between the steps were done manually and 95.0%  $\text{O}_2$ /5.0% Ar was used as the feed stream for these experiments. This limited our capability to explore faster cycles and more advanced configurations. Hence, the main goals here were first to explore whether Ag-ETS-10 can indeed produce high-purity  $\text{O}_2$  and second and more importantly to verify the model calculation's agreement with the experimental data in a process environment.

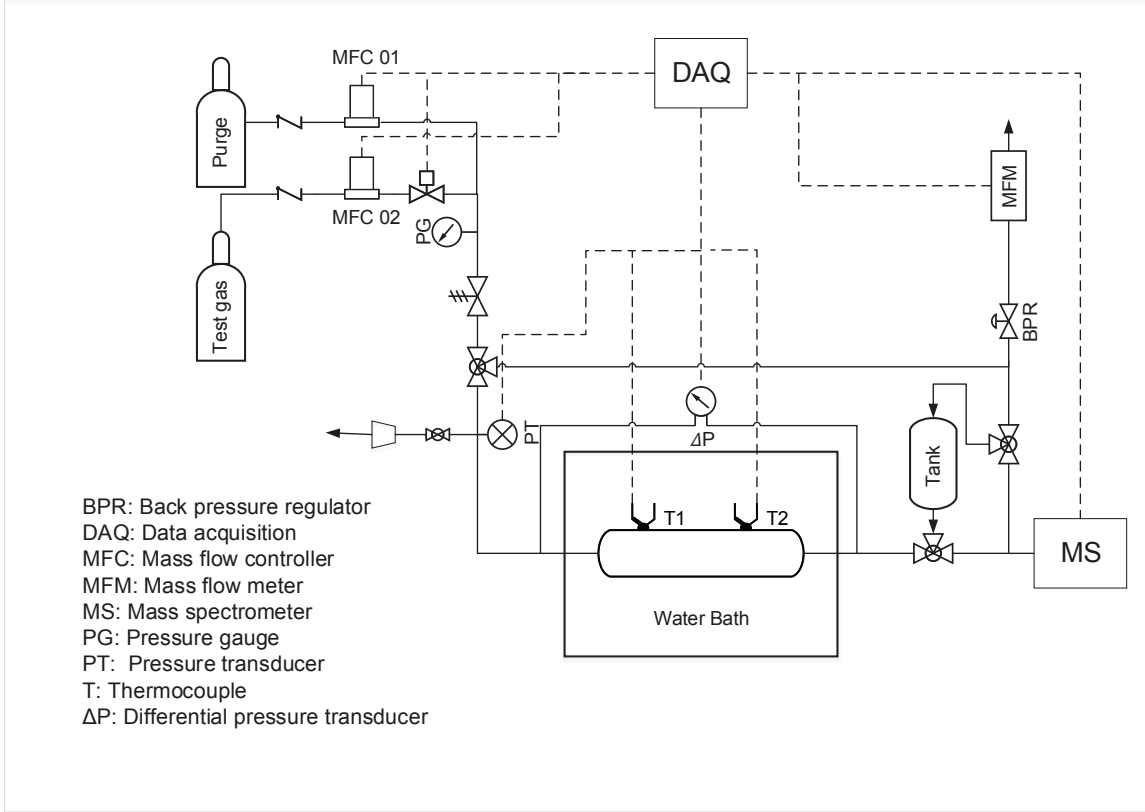


Figure 4.2: Schematic diagram of experimental VSA apparatus.

As the first attempt, a simple 3-step cycle was used to verify the model predictions. This cycle consisted of an adsorption step at  $P_H$ , evacuation step at  $P_L$ , and feed pressurization step to pressurize the column from  $P_L$  to  $P_H$ . All the operating conditions for the cycles are reported in Table 4.1. In order to match the experimental pressure profiles, the pressure profile during the pressurization step at  $Z = 0$  was assumed to follow the following linear form:

$$P_{Z=0} = \frac{(P_H - P_L)}{t_{FP}} t + P_L \quad (4.4)$$

where  $t$  is the time during the pressurization step. The depressurization profile at  $Z = 0$  during the evacuation step was also assumed to follow the following functional from:

$$P_{Z=0} = (P_L + (P_H - P_L)e^{-\lambda t}) \quad (4.5)$$

where  $\lambda$  is a fitting parameter and was fitted to the experimental pressure profiles during the evacuation step. The functions in Eqs 4.4 and 4.5 were used in the simulation. The

model prediction and the experimental pressure profiles for the simple 3-step cycle are shown in Figure 4.3.

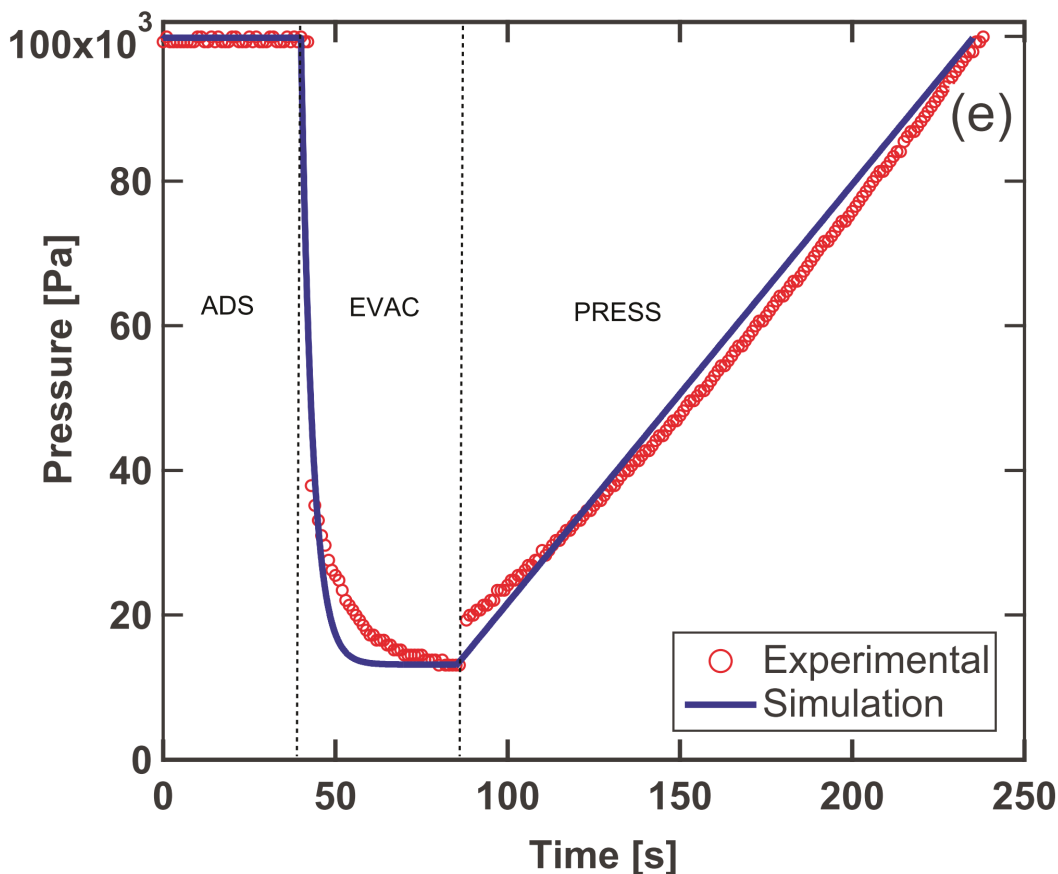


Figure 4.3: Comparison of experimental and simulated pressure profile experiment B. Operating conditions are provided in Table 3. Symbols are experimental values and lines correspond to simulation.

Cycle A and B in Table 4.1 were performed up to 25 cycles and the transient product concentration and axial temperature profiles were monitored in order to ensure cyclic steady-state has been reached. The effect of two different  $P_L$  values on  $O_2$  purity and recovery was investigated. Experimental oxygen purities in the product stream during the adsorption steps in each cycle were measured with a mass spectrometer. Experimental oxygen recovery was calculated by dividing the amount of  $O_2$  in the product stream by the amount of  $O_2$  introduced to the column during the adsorption and pressurization steps according to Eq 4.2. Number of moles of  $O_2$  in each of these streams were calculated for the last cycle, i.e. after reaching cyclic steady state, based on the values of the flow, temperature, pressure, and concentration measured by the instruments in the data acquisition system. The experimental  $O_2$  purity and recovery were later compared with

Table 4.1: Comparison of model results and experimental measurements for processes with 95/5 (O<sub>2</sub>/Ar) as the feed.

Cycle	$t_{\text{ADS}}$ [s]	$t_{\text{EVAC}}$ [s]	$t_{\text{FP}}$ [s]	$t_{\text{LR}}$ [s]	$F_{\text{ADS}}$ [ccm]	$P_{\text{L}}$ [kPa]	$Pu_{\text{O}_2}^{\text{exp}}$ [%]	$Pu_{\text{O}_2}^{\text{sim}}$ [%]	$Re_{\text{O}_2}^{\text{exp}}$ [%]	$Re_{\text{O}_2}^{\text{sim}}$ [%]
A: 3-step	40	45	85	-	150	47	95.5	95.7	15.6	15.6
B: 3-step	40	45	150	-	150	13	96.5	96.5	7.9	8.2
C: Skarstrom	15	45	150	25	150	13	98.7	98.9	4.4	3.1

the values predicted by the model according to Eq 4.2. As it is summarized in Table 4.1, experimental O<sub>2</sub> purity and recovery were closely predicted by the model. The model was further verified by adding a light reflux (LR) step into the cycle as described earlier (experiment C in Table 4.1). All the operating conditions were the same as the ones in experiment B, except the adsorption time which was reduced to 15 seconds and the remaining 25 seconds of the stream leaving the column during the adsorption step was stored in the tank and was later purged back to the column using the vacuum pump (LR step). The first 10 cycles were performed in a similar manner as the simple 3-step and at the eleventh cycle the configuration was switched to the Skarstrom cycle. As it can be seen in Table 4.1, the model was able to closely predict O<sub>2</sub> purity and recovery at cyclic steady-state. Figure 4.4(a) shows transient experimental O<sub>2</sub> purity in the product stream for this experiments and the comparison with the model. Each group of points in this figure correspond to the adsorption step in one cycle. Figure 4.4(b) depicts O<sub>2</sub> purity in the product with higher resolution for 95.0%-100.0% range. It can be concluded from Figure 4.4(a) and (b) that the model was able to describe the transient trend of O<sub>2</sub> purity in the product as well as the purity value at the cyclic steady-state condition. As it can be observed from Figure 4.4(c) and (d), experimental axial temperature profiles at the thermocouple located at 8 cm from the column inlet was also well captured by the simulations and further verified the model capability to predict experimental profiles. Figure 4.4(e) also shows the experimental and simulated pressure profiles for this cycle. It is worth noting that obtaining O<sub>2</sub> purities higher than 99.5% requires shorter cycle time, lower vacuum pressures, and larger fraction of the adsorption stream refluxed to the column, all of which were not feasible due to the limitations of the current experimental design, i.e. manual switching, single-column experiments, and air-operated vacuum pump. Now that the efficiency of the model to describe the experimental results have been verified, we proceed to the demonstration of the potential of the material and more advanced cycle configurations to product high-purity O<sub>2</sub> through the use of modeling and optimization.

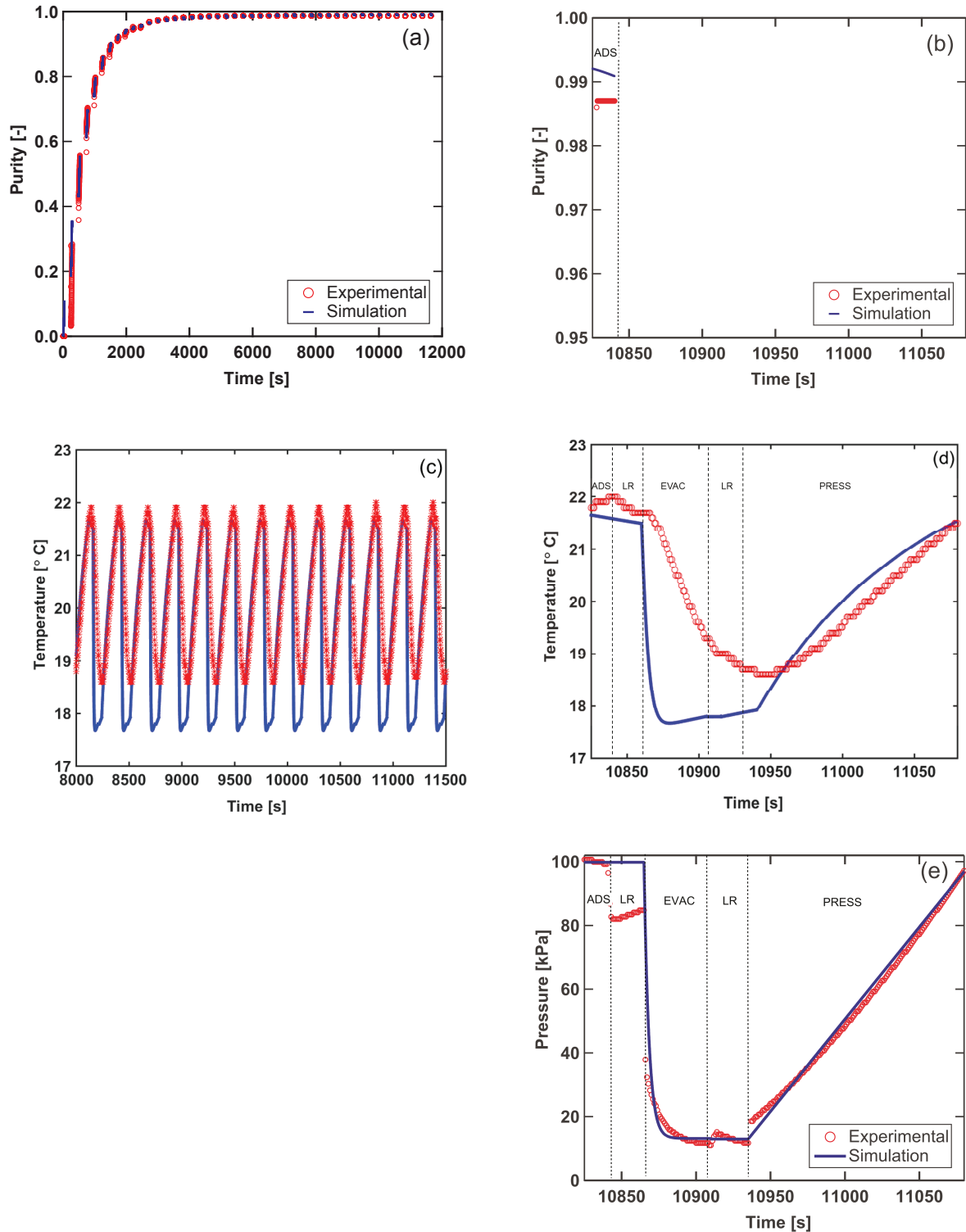


Figure 4.4: Comparison of experiments with model calculations for experiment C. Operating conditions are provided in Table 4.1. Symbols are experimental values and lines correspond to simulation. (a) Transient product purity during the adsorption steps; (b) Axial temperature profile for thermocouple located at 8 cm from the column inlet; (c) Transient product purity during the adsorption step with focus on high-purity range; (d) Axial temperature profile for thermocouple located at 8 cm from the column inlet for one cycle at cyclic steady state; (e) Experimental and simulated pressure profile.

### 4.3.2 Purity-Recovery optimization

#### Skarstrom cycle with 95.0% O<sub>2</sub>/5.0% Ar feed

In our previous study [66], a pre-purification stage was considered to remove all the N<sub>2</sub> and other impurities (CO<sub>2</sub>, H<sub>2</sub>O, etc.). Hence, the oxygen purification unit received a feed containing 95.0% O<sub>2</sub>/5.0% Ar. The purity-recovery Pareto curve was obtained and it was concluded that Ag-ETS-10 adsorbent has the ability to produce high-purity O<sub>2</sub> (> 99.5%) using a simple Skarstrom VSA cycle. In this study, bed length  $L$  was also included as one of the decision variables. The bounds for the decision variables are listed in Table 4.2.  $P_H$  was fixed at 100 kPa and the duration of the pressurization step  $t_{FP}$  was fixed at 5 seconds since this is a realistic time to pressurize a column with the dimensions reported in Table 2.1. The purity-recovery Pareto curve for this cycle is shown in Figure 4.5(a) and is compared with the Pareto curve obtained for the case when the bed length was fixed. Each point on the Pareto curve corresponds to a set of decision variables and the trend between purity and recovery shows the trade-off range between the two objective functions. The Pareto curve indicates that a purity value in excess of 99.0% and 99.5% can be achieved at a recovery of 14.7% and 11.1%, respectively. These values are relatively high compared to the values obtained where  $L$  was fixed at 0.32 m which were 11.35% and 6.9% for 99.0% and 99.5% purity, respectively. In other words, for a fixed value of recovery, higher purity was obtained for the case of variable bed length. It is worth noting that the effect of varying bed length is more pronounced at higher purity values. Figure 4.5(b) shows the recovery against  $\frac{t_{ADS} v_F}{L}$ , also known as bed utilization factor (BUF) [72], corresponding to the Pareto front in Figure 4.5(a). This plot indicates that for a certain value of recovery, the bed utilization factor was larger for a column with fixed  $L$ . This was possibly due to the fact that the Ar front has moved further into the column and could explain the lower purity obtained when  $L$  was set to 0.32 m. This hypothesis was further validated by investigating the axial profiles of O<sub>2</sub> and Ar concentrations during the adsorption step. Figure 4.6(a) shows O<sub>2</sub> gas phase axial profile at the end of the adsorption step against normalized bed length for a fixed and variable  $L$  cases. The operating conditions considered for this case study correspond to the optimal points on the two Pareto curves in Figure 4.5(a) with O<sub>2</sub> recovery fixed at 5.0%. The optimizer had chosen  $L = 1.12$  m for the variable bed length case. As it can be seen, O<sub>2</sub> concentration front has moved further through the column compared to the case of variable  $L$ . Figure 4.6(b) shows Ar solid phase axial profile against normalized bed length for the same condition. This figure implies that Ar concentration front has traveled more towards the product end of the column when the  $L$  was fixed at 0.32 m. Hence, the product stream during the adsorption step was contaminated with Ar which can explain

the lower O<sub>2</sub> purity in the product stream compared to the optimization with variable  $L$ .

Table 4.2: Range of decision variables used in cycle optimizations.

Decision variable	Range
$t_{\text{ADS}}$ [s]	2 – 10
$t_{\text{EVAC}}$ [s]	2 – 10
$t_{\text{LR}}$ [s]*	2 – 10
$t_{\text{HPP}}$ [s]**	0.02 – 9.9
$v_{\text{ADS}}$ [m s <sup>-1</sup> ]	0.005 – 0.2
$P_{\text{L}}$ [kPa]	3.0 – 60.0
$L$ [m]***	0.2 – 2.0

\* Skarstrom and 6-step with PE and LPP

\*\* 6-step with PE and HPP

\*\*\* Skarstrom with  $L$  as the decision variable

In a separate attempt, the effect of bed length on O<sub>2</sub> purity for a constant BUF was investigated and is presented in Figure 4.6(c). In this figure, BUF and  $t_{\text{ADS}}$  were fixed at 1.7 and 9.8 seconds, respectively. Bed length and feed velocity at the adsorption step were changed such that  $\text{BUF} = \frac{t_{\text{ADS}} v_{\text{F}}}{L}$  was constant. All other operating conditions were kept the same for this parametric study. As it can be observed from Figure 4.6(c), O<sub>2</sub> recovery increases for longer beds, i.e. higher  $v_{\text{F}}$  for a constant BUF. However, purity passes through a maximum at values of bed length around 1.3 m. Figures 4.6(a) to (c) further confirm the effect of bed length, as one of the operating conditions, on the performance indicators.

### PSA/PVSA Skarstrom with 95.0% O<sub>2</sub>/5.0% Ar feed

In order to investigate the effect of operating pressure during the adsorption and evacuation step on O<sub>2</sub> purity and recovery, pressure swing adsorption (PSA) and pressure-vacuum swing adsorption (PVSA) Skarstrom cycles were also studied and compared with VSA cycles. Two independent purity-recovery optimizations were performed to investigate the possibility of using PSA and PVSA cycles for high-purity O<sub>2</sub> production. According to Figure 3.1, since N<sub>2</sub> equilibrium selectivity over the other two components decreases significantly at higher pressures, only a feed stream containing 95.0% O<sub>2</sub>/5.0% Ar was considered for this case study. Dual-site Langmuir isotherm parameters, reported in Table 3.1, were used to describe adsorption equilibrium in all the simulations in the section. For PSA cycle optimization,  $P_{\text{L}}$  was fixed at 100 kPa and  $P_{\text{H}}$  was considered as a decision variable with 150.0 kPa and 1500.0 kPa as the lower and the upper bounds, respectively. For PVSA cycle optimization,  $P_{\text{H}}$  was fixed at 500.0 kPa and  $P_{\text{L}}$  was varied between 3.0 to 60.0 kPa. Bed length was fixed at 0.32 m for both of the optimizations. The rest of the

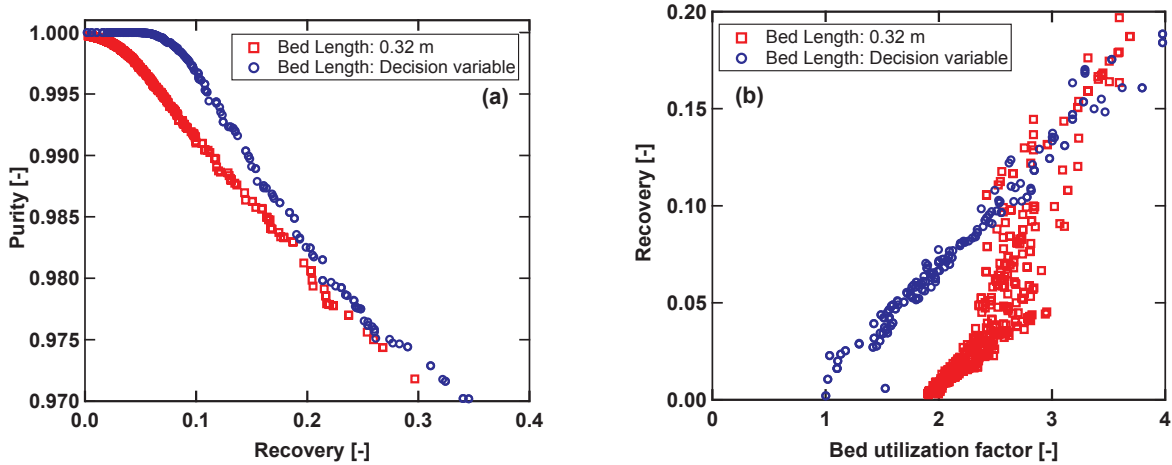


Figure 4.5: Results of process optimization to maximize  $O_2$  purity and recovery for 95.0%  $O_2$  5.0% Ar as the feed using the Skarstrom cycle. (a) Comparison of Pareto curves for the optimization of  $O_2$  purity and recovery with fixed and variable bed lengths; (b) Variation of recovery as a function of bed utilization factor for the Pareto points.

of the bounds for the other decision variables were similar to those reported in Table 4.2. Figure 4.7(a) shows the corresponding purity-recovery Pareto curves for PSA and PVSA Skarstrom cycles. This figure indicates neither PVSA nor PSA cycles were able to meet the purity constraints ( $Pu > 99.0\%$ ) and have no advantage over the VSA cycle with  $P_H$  fixed at 100 kPa. The PSA cycle was able to reach 98.5% but the recovery values were significantly lower compared to the previously studied VSA cycle. Figure 4.7(b) shows the variation of purity against  $P_H$  for the PSA cycle. The points on this figure correspond to the optimal Pareto points in Figure 4.7(a). It can be concluded from this figure that in order to obtain high-purity  $O_2$ , there is no advantage in increasing the pressure during the adsorption step and the optimal value lies somewhere between 200 to 300 kPa and the VSA Skarstrom cycle performed better both in terms of purity and recovery. In a separate attempt, both  $P_H$  and  $P_L$  were considered as decision variables and purity-recovery Pareto curve was obtained as shown in Figure 4.7(a). This Pareto front lies exactly over the VSA Pareto curve with a negligible difference. This further verifies the superiority of the VSA cycle over the PSA/PVSA cycles. It is worth noting that according to the high pressure isotherm measurements shown in Figure 3.1, equilibrium selectivity of Ar over  $O_2$  decreases by increasing the pressure and it implies less advantage in performing PSA/PVSA cycles. Therefore, in this study, only VSA cycles were considered for  $O_2$  purification using Ag-ETS-10.

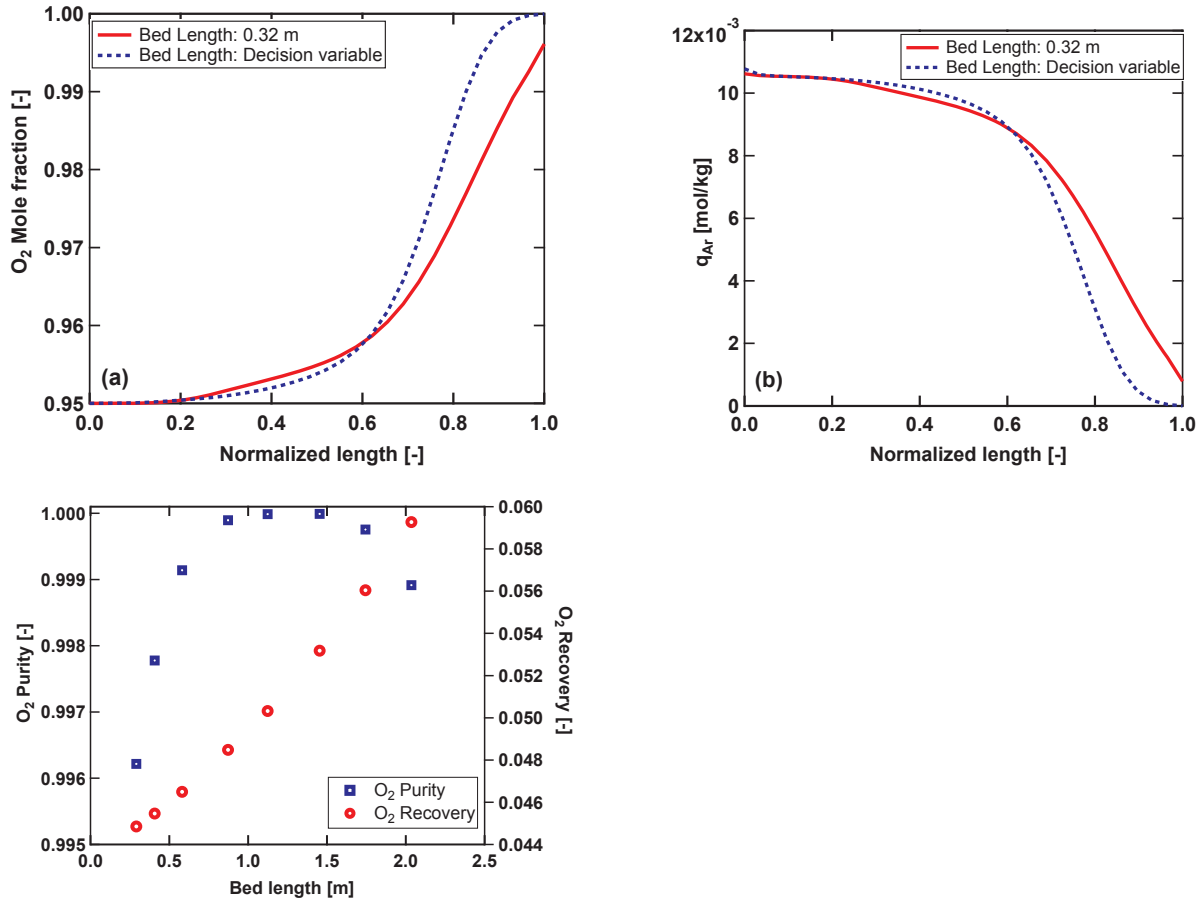


Figure 4.6: Effect of bed length on axial concentration profiles and performance indicators.  $L = 1.12$  m was chosen by the optimizer for the variable bed length optimizations. (a) O<sub>2</sub> gas phase axial concentration profiles at the end of the adsorption step; (b) Ar solid phase axial concentration profiles at the end of the adsorption step; (c) O<sub>2</sub> purity and recovery as a function of  $L$  for a fixed BUF=1.7 and  $t_{ADS}=9.8$  s.

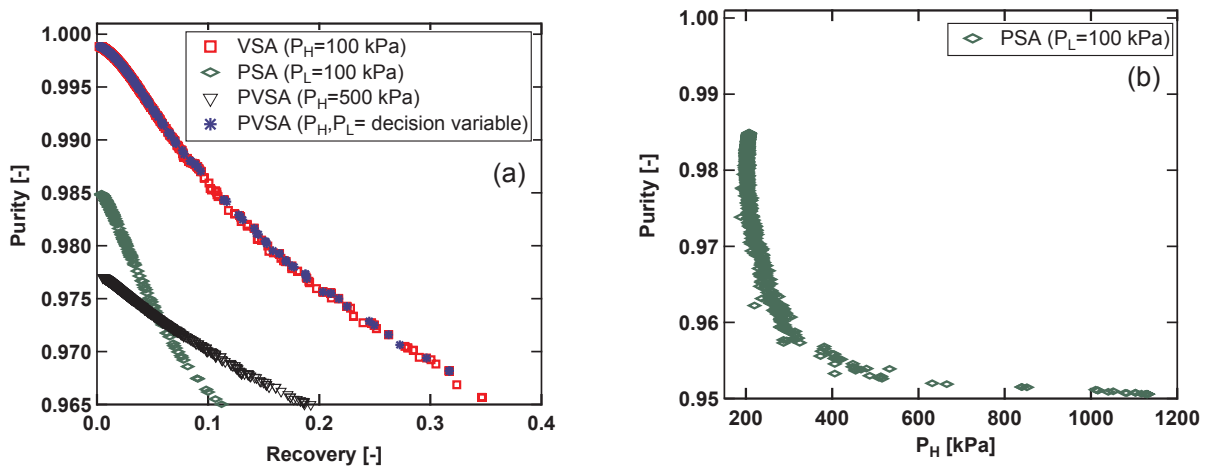


Figure 4.7: Comparison of PSA, VSA, and PVSA Skarstorm cycles for high-purity O<sub>2</sub> production from 95.0% O<sub>2</sub> 5.0% Ar feed. (a) Pareto curve for the optimization of O<sub>2</sub> purity and recovery; (b) Variation of purity as a function of  $P_H$  for the PSA cycle Pareto points.

### 6-step with PE and LPP

In a recent publication, Ferreira et al [1] proposed a VSA cycle which included pressure equalization (PE) and light product pressurization (LPP) steps instead of feed pressurization as in the Skarstrom cycle in order to improve the recovery of  $O_2$  in the raffinate stream (Figure 4.1(b)). The decision variables and the bounds are shown in Table 4.2. Intermediate pressure  $P_I$  was also fixed based on the value of low pressure  $P_L$  in such a way that the mass balance constraints, as discussed earlier in section 4.3.2, are satisfied. The value of  $L$  was fixed at 0.32 m similar to the column available in our laboratory. If during the LPP step, the pressure in the column does not reach  $P_H$ , the column goes through a feed pressurization and  $O_2$  introduced to the column during this step should be also considered in the definition of recovery in Eq.4.2. The purity-recovery Pareto curve for this cycle, shown in Figure 4.9(a) indicates that a purity value in excess of 99.5% and 99.8% can be achieved at a recovery of 27.3% and 23.1%, respectively. These values are higher compared to the simple Skarstrom cycle as discussed in the previous section. Fiererra et al [1] have reported 99.75% purity with 5.6% and 99.51% purity with 14.2% recovery using the same cycle with Ag-LiLSX. Figure 4.9(b) shows axial profile of  $O_2$  gas phase concentration for the adsorption, evacuation, and light reflux steps at cyclic steady state corresponding to the optimal point on the Pareto curve in Figure 4.9(a) with  $O_2$  purity of 99.5%. At the end of light reflux step,  $O_2$  mole fraction leaving the column at  $z = 0$  was around 96.0% and can cause a decrease in the recovered  $O_2$  in the raffinate stream. To overcome this effect, pressurizing with the heavy product might assist in improving the recovery of the cycle and is further discussed in the following section. Optimization of purity-recovery values for Ag-LiLSX and the comparison with Ag-ETS-10, using the column dimensions reported by Ferreira et al [1], is shown in Figure 4.8. Despite the acceptable predictions by the model, the discrepancy between the predicted data and the experimental data was possibly due to the difference in defining the pressure profiles during the evacuation and pressurization steps. It is worth mentioning that the model under predicts the experimental  $O_2$  purity and recovery values.

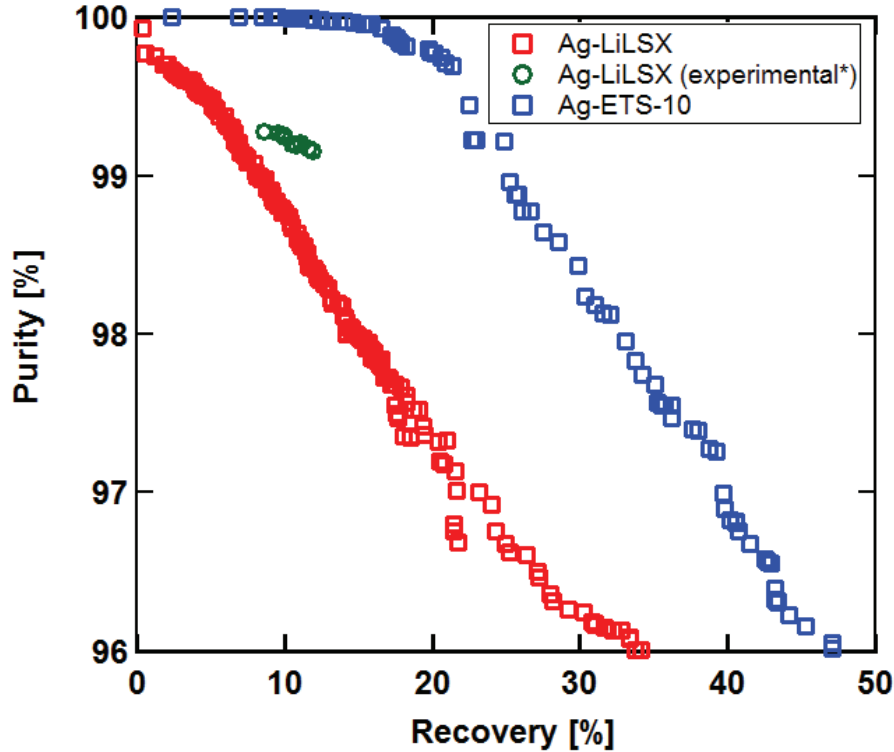


Figure 4.8: Results of process optimization to maximize  $O_2$  purity and recovery for 95.0%  $O_2$ /5.0% Ar as the feed. Experimental data and column dimension for the simulations are obtained from Ferreira et al [1].

### 6-step with PE and HPP

The main objective in designing this cycle, is to improve the recovery of the light product by keeping the benefits of the previous cycles. Large amount of  $O_2$  is lost during the evacuation step in the cycles discussed in the previous sections. Therefore, refluxing part of the extract product from the evacuation step might be helpful in increasing  $O_2$  recovery. This cycle includes a pressure equalization (PE) step and a fraction of the heavy product leaving the evacuation step was used to pressurize the column from  $P_L$  to  $P_H$ . The decision variables and their bounds are shown in Table 4.2. Bed length was fixed at 0.32 m similar to the column available in our laboratory. If the pressure in the column does not reach  $P_H$  during the HPP step, the column will go through a feed pressurization step. Hence,  $O_2$  introduced to the column during this step should be also considered in the definition of recovery in Eq.4.2. Figure 4.9(a) shows the purity-recovery Pareto curve obtained for this cycle. As it can be observed, a significant improvement in the recovery was achieved by introducing the heavy product pressurization step. Purity values in excess of 99.5% and 99.8% can be achieved at a recovery of 91.7% and 89.8%, respectively. To our knowledge, this is the highest value of recovery reported in literature for  $O_2$  product with purity of

99.5% using an equilibrium-based VSA cycle.

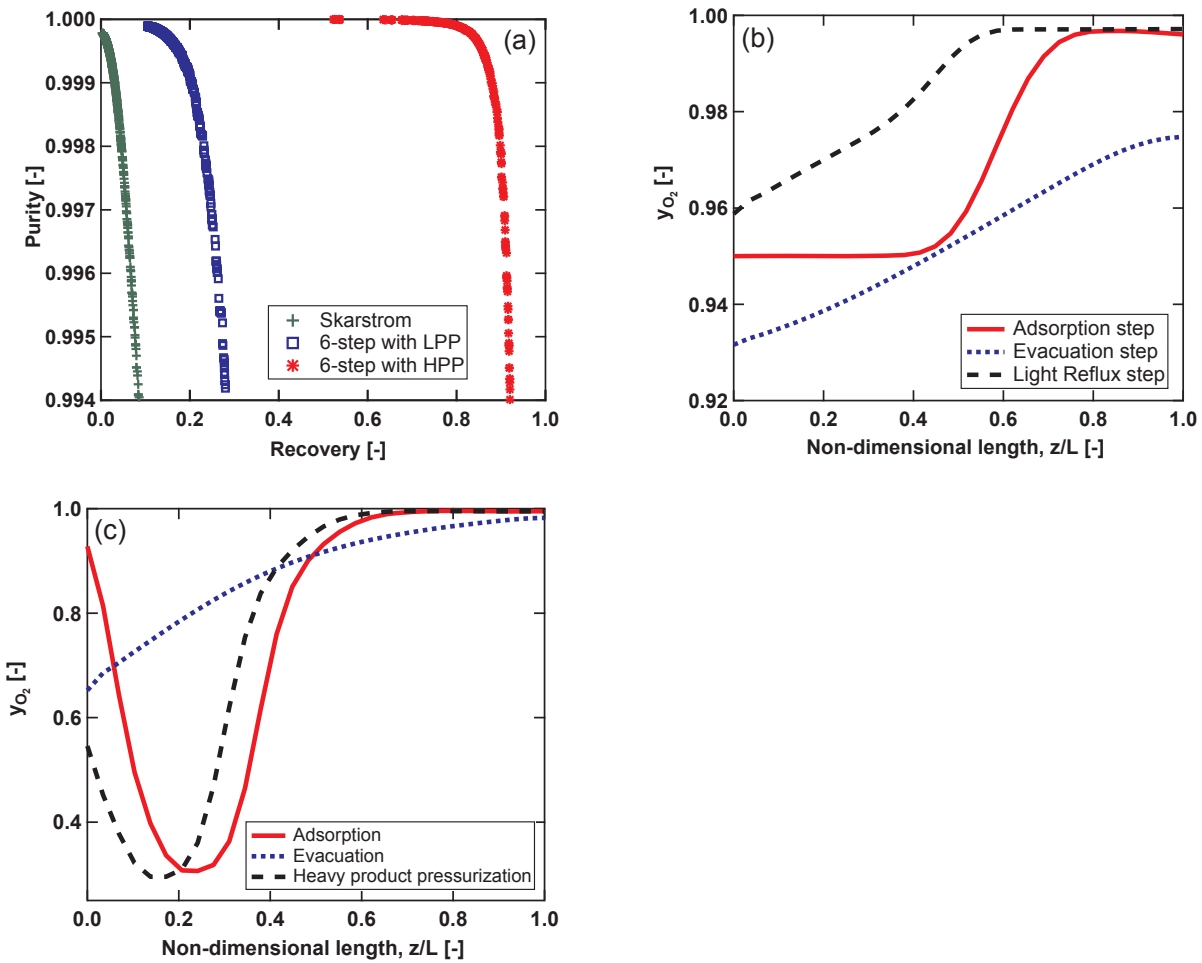


Figure 4.9: Comparison of various cycles for high-purity O<sub>2</sub> production. (a) Results of process optimization to maximize O<sub>2</sub> purity and recovery for the Skarstrom, 6-step with PE and LPP, and 6-step with PE and HPP cycles; (b) Axial profiles of gas phase mole fraction for the adsorption, evacuation, and light reflux steps of the 6-step cycle with PE and LPP; (c) Axial profiles of gas phase mole fraction for the adsorption, evacuation, and heavy product pressurization steps of the 6-step cycle with PE and HPP.

Figure 4.9(c) shows O<sub>2</sub> gas phase mole fraction axial profiles for the adsorption, evacuation, and heavy product pressurization steps corresponding to the optimal point on the Pareto curve in Figure 4.9(a) with O<sub>2</sub> purity of 99.5%. As it can be observed, O<sub>2</sub> composition in the stream leaving the evacuation step was decreased to values around 65.0% and pressurizing with the heavy product has assisted in pushing O<sub>2</sub> front further towards the product end of the column thus improving O<sub>2</sub> recovery in the raffinate. As shown in Figure 4.9(a), by comparing the Pareto curves for all three cycle discussed above, it can be concluded that the 6-step cycle with PE and HPP can be considered as an effective O<sub>2</sub>

purification VSA cycle with high values of recovery for O<sub>2</sub> purities of more than 99.5%.

### 4.3.3 Energy-Productivity optimization

The optimization studies reported here confirmed the capability of Ag-ETS-10 to produce high-purity O<sub>2</sub> at high recoveries. The ultimate test of the process is the energy consumption and its size which determines the cost of the product. A second set of optimizations were conducted in order to maximize the productivity and minimize the total energy consumption of the VSA cycles. The range of decision variables used in this set of optimizations is reported in Table 4.2 and was similar to the purity-recovery optimizations. Since the constraint for on-site O<sub>2</sub> applications is on the purity, three different O<sub>2</sub> purity constraints (99.8%, 99.5%, and 99.0%) were imposed while conducting energy-productivity optimizations. However, no constraint was considered for the recovery of the cycle. The purity constraints were implemented by introducing a penalty function as discussed in Eq. 4.3.

Productivity of each cycle is defined as the total tonnes of O<sub>2</sub> in the product stream divided by the volume of adsorbent per day:

$$Pr = \frac{\text{Total tonnes of O}_2 \text{ in the raffinate product}}{(\text{Total volume of adsorbent})(\text{Cycle time})} \quad (4.6)$$

Total energy consumption of the cycle is a summation of the energy required in each of the steps in one cycle. Since the high pressure during the adsorption step was fixed at 100 kPa and was equal to the feed gas pressure, there is no energy consumed during the feed pressurization step or similar steps such as light and heavy product pressurizations. This argument is also valid for the pressure equalization step (PE) and as a result, adding a PE step should assist in minimizing the total energy consumption of the cycle. The energy consumed during the adsorption step is to overcome the frictional pressure along the column and is described by the following equation:

$$E_{\text{ADS}} = \frac{1}{\eta} \epsilon \pi r_{\text{in}}^2 \frac{\gamma}{\gamma - 1} \int_{t=0}^{t=t_{\text{ADS}}} v_{\text{ADS}} P(t) \left[ \left( \frac{P(t)}{P_{\text{feed}}} \right)^{\frac{\gamma-1}{\gamma}} - 1 \right] dt \quad (4.7)$$

where  $\eta$  is the compression efficiency and is considered to be 0.72 in this study.  $\gamma$  is the adiabatic constant and is equal to 1.4.  $P_{\text{feed}}$  is the feed pressure equal to 100 kPa. During the steps which include a decrease in the column's pressure or are carried out at pressures

lower than vacuum pump's discharge pressure, energy is required to decrease the pressure inside the column from  $P_H$  to  $P_L$  or keep the pressure at  $P_L$ . The delivery pressure of the vacuum pump is assumed to be 100 kPa and the total energy consumption during these steps is calculated as the following:

$$E_{\text{step}} = \frac{1}{\eta} \epsilon \pi r_{\text{in}}^2 \frac{\gamma}{\gamma - 1} \int_{t=0}^{t=t_{\text{step}}} v(t) P(t) \left[ \left( \frac{P_{\text{atm}}}{P(t)} \right)^{\frac{\gamma-1}{\gamma}} - 1 \right] dt \quad (4.8)$$

where  $P_{\text{atm}}$  is the atmospheric pressure. This equation is used when calculating the energy consumed during the evacuation and light reflux steps. Total energy consumption for one cycle will be calculated depending on the steps in each cycle and is reported in terms of kilowatt hours per tonne of  $O_2$  produced.

Total energy consumption for the Skarstrom cycle is calculated using the following equation:

$$E_T = \frac{E_{\text{ADS}} + E_{\text{EVAC}} + E_{\text{LR}}}{\text{Total tonnes of } O_2 \text{ in the raffinate product}} \quad (4.9)$$

Three different purity constraints (99.8%, 99.5 %, and 99.0%) were imposed and the corresponding energy-productivity Pareto curves are shown in Figure 4.10(a). As it can be seen, while maximizing the productivity, more energy was required to reach the higher purity constraints. At a purity of 99.8%, the energy required increases sharply with an increase in the productivity. Total energy consumption for the 6-step cycle with PE and LPP is defined similar to the Skarstrom cycle as in Eq. 4.9. However, since there is no LR step in the 6-step cycle with PE and HPP, the total energy consumption for this cycle is defined as the following:

$$E_T = \frac{E_{\text{ADS}} + E_{\text{EVAC}}}{\text{Total tonnes of } O_2 \text{ in the raffinate product}} \quad (4.10)$$

Figure 4.10(b) and (c) show the energy-productivity Pareto curves for the two cycles. The comparison of all three cycles for a purity constraint of 99.5% is presented in Figure 4.10(d). It can be concluded that both the 6-step with PE and LPP and the 6-step with PE and HPP require less energy compared to the Skarstrom cycle. This can be attributed to the addition of the pressure equalization step that reduces the amount of energy required during the evacuation step. The 6-step cycle with PE and LPP performs slightly better compared to the 6-step cycle with PE and HPP in terms of energy consumption. However,

it should be noted that these Pareto curves were obtained considering 95.0% O<sub>2</sub>/5.0% Ar as the feed and N<sub>2</sub> should be separated prior to this stage of the process. Therefore, recovery of the second stage, studied in this section, is an important parameter when it is combined with the first stage, i.e. N<sub>2</sub> removal stage. In order to identify the most optimized design and combination of single- and dual-stage O<sub>2</sub> separation processes, one needs to calculate the total energy consumption and the productivity of the whole separation process which requires considering the recovery of all the stages. Moreover, introducing dry air as the feed for the two 6-step cycles described above is worth considering. This will be the focus of Chapter 5.

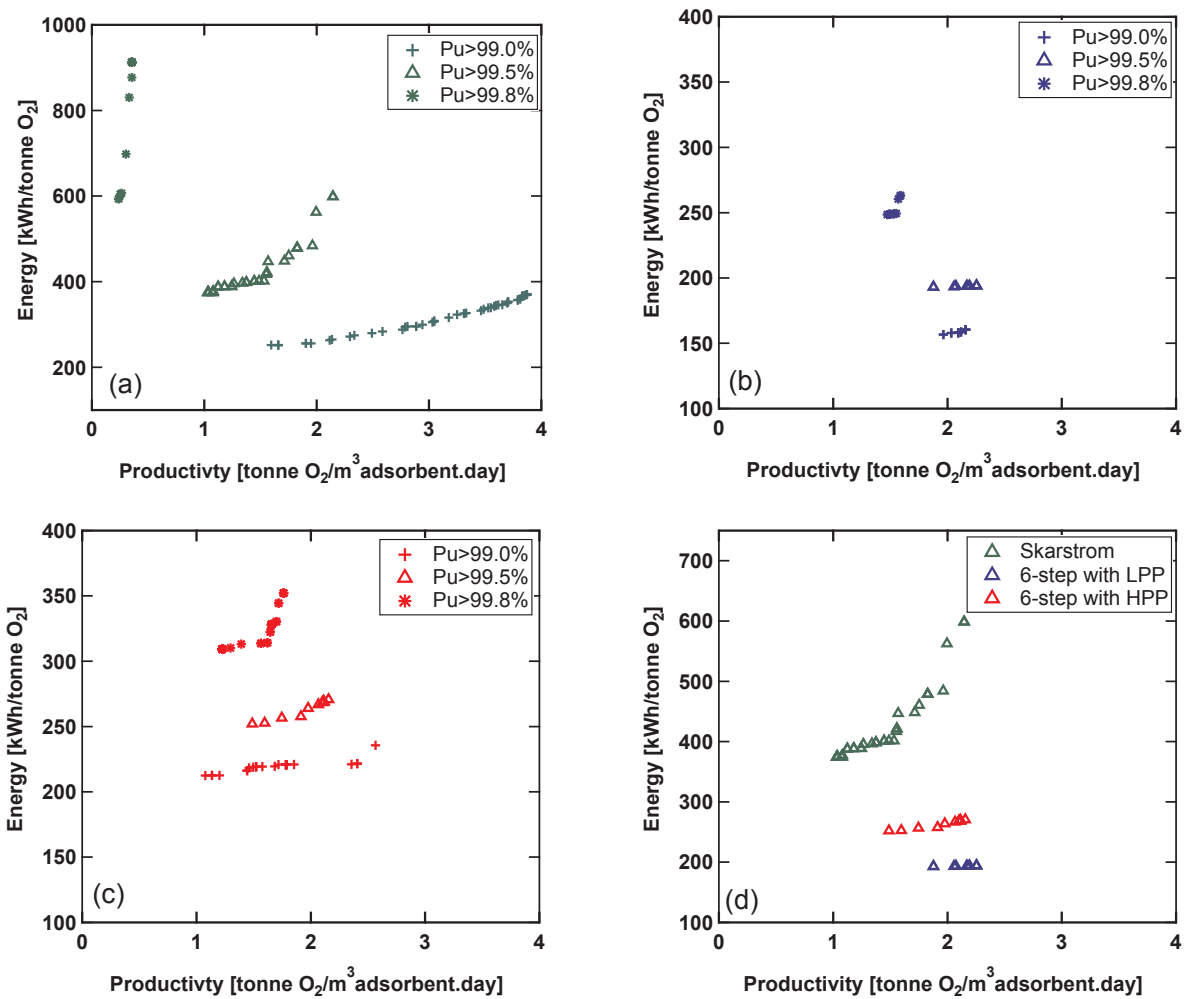


Figure 4.10: Results of process optimization to maximize O<sub>2</sub> productivity and minimize energy consumption for 95.0% O<sub>2</sub>/5.0% Ar as the feed. (a) Skarstrom cycle; (b) 6-step with PE and LPP cycle; (c) 6-step with PE and HPP cycle; (d) comparison of all three cycles for a purity constraint of 99.5% O<sub>2</sub>.

## 4.4 Conclusions

In this study, multiple vacuum swing adsorption (VSA) cycle configurations for high-purity O<sub>2</sub> production were thoroughly studied and optimized to maximize O<sub>2</sub> purity and recovery. A mixture of 95.0%/5.0% O<sub>2</sub>/Ar feed was considered for the Skarstrom cycle. Experimental 3-step and Skarstrom cycle demonstrations verified the simulations. Both experimental purity and recovery plus the axial temperature profiles were well predicted by the model. Considering bed length as the decision variable for the optimizations demonstrated an enhanced recovery of 11.1% for a product stream with 99.5% O<sub>2</sub> purity. In a separate attempt, pressure swing adsorption (PSA) and pressure-vacuum swing adsorption (PVSA) Skarstrom cycles were also studied in addition to VSA cycle and it was concluded that VSA has a better performance compared to the other two cycles. Two more advance cycles, a 6-step with pressure equalization (PE) and light product pressurization (LPP) steps, and a 6-step with pressure equalization (PE) and heavy product pressurization (HPP) steps, were also considered in this study to improve the recovery of the cycle. For the 6-step with PE and LPP, the recovery of O<sub>2</sub> obtained in the product stream for a purity of 99.5% was 27.3%. This value was significantly improved to 91.7% for a 6-step with PE and HPP. The second set of optimizations were conducted to maximize productivity of O<sub>2</sub> and minimize total energy consumption of the VSA cycles. Three different purity constraints were imposed and the Pareto curves were obtained for various cycles. A significant improvement in the performance indicators was obtained through process optimization for the two 6-step cycles. However, more analysis is required to compare single-stage and dual-stage O<sub>2</sub> VSA cycles and to identify the best design with the lowest energy consumption and the highest productivity while meeting the purity constraints.

## Chapter 5

# Optimal process design: single-stage vs. dual-stage

Producing high-purity oxygen with purities higher than 99.5% is challenging. Oxygen at this level of purity is required in the military and aerospace industries. In this study, the possibility of producing high-purity O<sub>2</sub> with silver-exchanged titanosilicates (Ag-ETS-10) using multiple single-stage and dual-stage vacuum swing adsorption (VSA) cycle configurations was investigated through cycle experiments, process simulation, and optimization. Oxygen purity-recovery Pareto fronts for the Skarstrom cycle and 6-step cycle with pressure equalization (PE) and heavy product pressurization (HPP) with dry air as the feed was obtained. The simulations predicted 82.0% recovery for a product with 99.5% purity for a 6-step cycle with PE and HPP and dry air feed stream. The effect of bed length and nitrogen content in the feed on the performance indicators was also studied. Operating conditions for various cycle configurations were optimized through non-dominated sorting genetic algorithm technique to achieve lower total energy consumption and higher overall productivity and the Pareto fronts were compared against each other in order to choose the best possible design. The results indicated that the single-stage 6-step cycle with PE and HPP presents a better performance compared to the other single-stage and dual-stage approaches. A simple graphical scheduling study was also conducted in order to calculate the number of columns required for a continuous process using the better performing configurations.

## 5.1 Introduction

In Chapter 4, multiple vacuum swing adsorption cycles were studied for O<sub>2</sub> purification from a N<sub>2</sub> free feed containing 95% O<sub>2</sub>/5% Ar using Ag-ETS-10. Three cycle configurations, namely 4-step Skarstrom, 6-step with pressure equalization (PE) and light product pressurization (LPP), and 6-step with PE and heavy product pressurization (HPP), were considered and it was concluded that the two 6-step cycles provide a higher O<sub>2</sub> recovery compared to the Skarstrom cycle. The 6-step with PE and LPP showed a 27.3% O<sub>2</sub> recovery for a product containing 99.5% O<sub>2</sub>. This value was significantly improved to 91.7% for the 6-step with PE and HPP. The energy-productivity optimizations in Chapter 4 indicated a lower energy consumption for the same level of productivity for the two 6-step cycles compared to the Skarstrom cycle and it was concluded that for a better comparison between the configurations, N<sub>2</sub> removal stage should be also explored.

Silver exchanged titanosilicates (Ag-ETS-10) have a very high thermodynamic selectivity compared to the other sorbents reported for O<sub>2</sub>/Ar separation [21]. Therefore, the possibility of producing high-purity O<sub>2</sub> in a single-stage adsorption process using this material is worth investigating. The purpose of this study is to explore the possibility of O<sub>2</sub> purification from air using a single-stage separation process through experiments and simulations and later compare the performance indicators with the possible dual-stage O<sub>2</sub> purification configurations. The strategy of this work in exploring multiple options is summarized as a block diagram in Figure 5.1.

As the first step, single-stage O<sub>2</sub> purification was studied using the Skarstrom and the 6-step with PE and HPP cycles. Simple single-column Skarstrom cycle experiments were compared with the model predictions and the two cycles were optimized both to obtain high O<sub>2</sub> purity and recovery and also to minimize total energy consumption and maximize O<sub>2</sub> productivity. Cycle configuration and pressure profiles for these two cycles are shown in Figure 4.1(a) and (c), respectively.

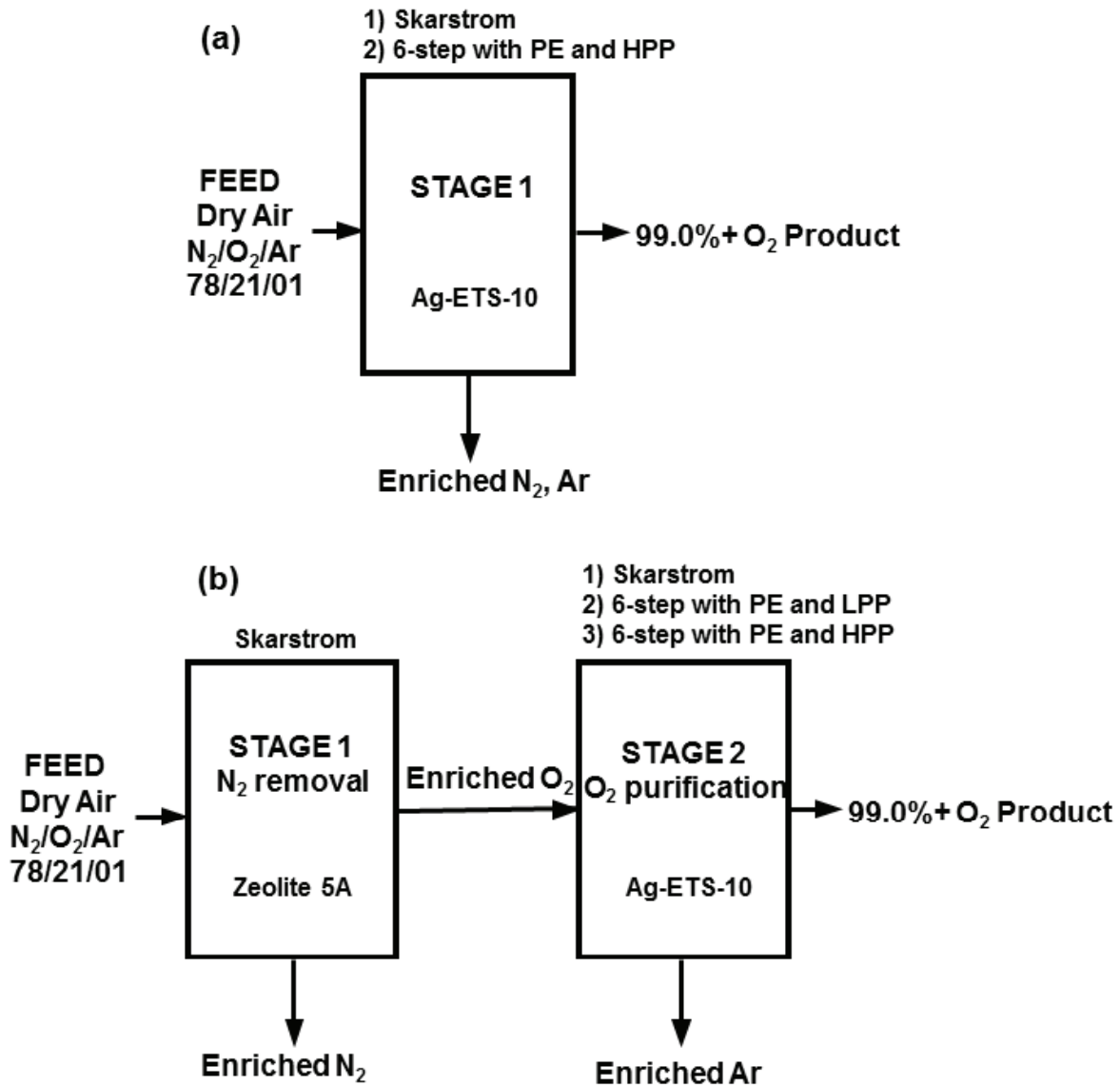


Figure 5.1: Strategy of this study for high-purity O<sub>2</sub> production: (a) single-stage O<sub>2</sub> production. (b) Dual-stage O<sub>2</sub> production.

The Skarstrom cycle is a simple four step cycle with the technology already available on the market. It contains an adsorption step at high pressure  $P_H$ , evacuation at low pressure  $P_L$ , light reflux at  $P_L$ , and pressurization from  $P_L$  to  $P_H$ . Due to the simplicity of this cycle, the possibility of single-stage  $O_2$  purification using this cycle was further explored experimentally and is discussed in section 5.3.1. In addition to the experimental demonstrations, the operating conditions for the Skarstrom cycle with dry air feed were optimized through process simulation and optimization to maximize  $O_2$  purity,  $O_2$  recovery, and productivity, and to minimize total energy consumption of the cycle. Skarstrom cycle has its own advantages such as the simplicity and availability of the technology on the market. However, as discussed in Chapter 4, to enhance  $O_2$  recovery, more advanced cycles should be considered. The 6-step cycle with PE and HPP showed a significant improvement in the process performance indicators when 95%  $O_2$ /5% Ar was introduced as the feed. In this study, dry air feed was also considered as the feed for this cycle and the operating conditions were optimized both to maximize  $O_2$  purity and recovery and to minimize total energy consumption and maximize productivity of the cycle while meeting the purity constraint of 99.5%  $O_2$ .

The other possible approach to produce high-purity  $O_2$ , as shown in Figure 4.1(b), is to perform a dual-stage process where in the first stage,  $N_2$  removal occurs with a product rich in Ar and  $O_2$  (and some  $N_2$ ). This product is introduced to the second stage, where  $O_2$  is purified to high-purity range. Multiple sorbents such as zeolite 5A, LiLSX, and Na-ETS-10 can be used for  $N_2$  removal stage. Once the majority of  $N_2$  in the air is captured in the first stage, the product is introduced to the second stage in order to further purify  $O_2$ . In this study, Ag-ETS-10 was considered as the sorbent for this stage. Multiple cycle configurations can be considered for the  $O_2$  purification stage. In this study, three configurations namely, the Skarstrom, 6-step with PE and LPP, and 6-step with PE and HPP were studied. These results, from the single-stage and the dual-stage energy-productivity optimizations, were later compared with each other and a simple graphical scheduling study was conducted in order to find the minimum number of columns required for a continuous process in each of the configurations.

## 5.2 Materials and methods

### 5.2.1 Materials

In this study, the Skarstrom cycle using zeolite 5A was considered for the first stage due to the availability of the experimental isotherm data for N<sub>2</sub> and O<sub>2</sub> at multiple temperatures [73]. The fitted dual-site Langmuir adsorption isotherm model parameters for N<sub>2</sub> and O<sub>2</sub> adsorption on zeolite 5A are shown in Table 5.1. It is worth noting that adsorption isotherm model parameters for Ar were considered to be identical to the ones for O<sub>2</sub> since zeolite 5A has no thermodynamic selectivity for Ar over O<sub>2</sub>. The optimization of the operating conditions of this stage to maximize productivity and minimize total energy consumption for different levels of N<sub>2</sub> content in the product of this stage is presented in section 5.3.1.

Table 5.1: Fitted Langmuir adsorption parameters for N<sub>2</sub> and O<sub>2</sub> on zeolite 5A.

Parameter	N <sub>2</sub>	O <sub>2</sub>
$b_0$ (m <sup>3</sup> mol <sup>-1</sup> )	$6.81 \times 10^{-7}$	$1.55 \times 10^{-6}$
$q_s$ (mol kg <sup>-1</sup> )	2.7	2.72
$-\Delta U_i$ (kJ mol <sup>-1</sup> )	20.83	16.69

The Ag-ETS-10 extrudates used in this study were similar to the ones reported earlier [66] made by using the hydrothermal method [22, 55] to synthesize Na-ETS-10 and later exchanged with silver nitrate to form Ag-ETS-10. The physical properties of the samples used in the simulations were similar to the ones reported in our earlier publication [66]. Adsorption isotherms of N<sub>2</sub>, O<sub>2</sub>, and Ar at 303.15 K, 323.15 K, and 343.15 up to 115 kPa were measured using the volumetric technique and are shown in Figure 2.2. The single-site Langmuir model parameters are also reported in Table 2.2.

### 5.2.2 Cycle configurations

The first design investigated in this study was the Skarstrom cycle. Multiple feed streams, i.e. product streams from the first stage, with various N<sub>2</sub> concentrations were used for the energy-productivity optimization. The results of this optimization was later combined with the N<sub>2</sub> removal stage optimization to calculate the overall energy-productivity values and is discussed in the result and discussion section. The other two possible cycle configurations explored in this study for the second stage, were the 6-step cycle with PE and LPP and

the 6-step cycle with PE and HPP. The cycle configurations and pressure profiles of these two cycles are shown in Figure 4.1(b) and (c), respectively. It was assumed that these two cycles receive a nitrogen free feed containing 95% O<sub>2</sub>/5% Ar. The energy-productivity optimization results for these two cycles were presented in Chapter 4 and is used to calculate the overall energy-productivity values for the dual-stage processes. The column dimensions and adsorbent properties used in the simulation were identical to those reported earlier [66] and are summarized in Table 2.1.

### 5.2.3 Cycle optimization

Similar to our previous study, the purity-recovery and energy-productivity optimizations were performed by implementing the non-dominated sorting genetic algorithm II (GA) in MATLAB global optimization toolbox. Fifty generations, with a population size equal to 24 times of the number of decision variables, were created by the GA. The initial population was created using latin hypercube sampling (LHS) to prevent bias towards the bounds of the decision variables. A desktop workstation with two 12-core INTEL Xeon 2.5 GHz processors and 128 GB RAM was used to conduct the parallelized optimizations. Two sets of optimization were conducted in this study. The first set was the optimization of the operating conditions for the Skarstrom cycle and the 6-step cycle with PE and HPP to maximize O<sub>2</sub> purity and recovery for the single-stage adsorption processes. The second optimization analysis was conducted to minimize total energy consumption and maximize productivity of each of the cycles. The objective functions and the decision variables used in the optimization were similar to Chapter 4. The bounds for the decision variables are listed in Table 5.3. High pressure during the adsorption step  $P_H$  was fixed at 100 kPa and the duration of the pressurization step  $t_{FP}$  was fixed at 5 seconds since this is the realistic time to pressurize a column with the dimensions reported in Table 2.1. The purity constraint for the energy-productivity optimizations was fixed at 99.5% O<sub>2</sub>.

## 5.3 Results and discussion

### 5.3.1 Single-stage production of high-purity oxygen

Single-stage O<sub>2</sub> purification from air is preferred over a two-stage process due to its simplicity and the reduction in the number of fluid movers that are required in the process. In this study, the possibility of producing high-purity O<sub>2</sub> in a single stage using Ag-ETS-10 was explored experimentally and later two cycle configurations, namely the Skarstrom

and 6-step with PE and HPP cycles were optimized both for O<sub>2</sub> purity-recovery and energy-productivity values and were compared against each other.

## Experimental demonstration

A modified version of the dynamic column breakthrough apparatus described in our earlier publication [66] was used to run simple VSA cycle experiments using only one column. The schematic diagram of the apparatus is shown in Figure 4.2. Flow directions were controlled by manual switchings of the valves and a tank was used to store the exit stream during the adsorption step and was used later for the light reflux step. All the experiments were done at 293.15 K and 100 kPa with dry air (78.0% N<sub>2</sub>, 21.0% O<sub>2</sub>, and 1.0% Ar) as the feed.

The simple 4-step Skarstrom cycle experiments were conducted and the results were compared with the model predictions. Adsorption (ADS) and evacuation (EVAC) steps were performed at  $P_H$  and  $P_L$ , respectively. The light reflux step (LR) was conducted at  $P_L$  and the pressurization (PRESS) step with the feed stream was performed to pressurize the column from  $P_L$  to  $P_H$ . Two experiments with the operating conditions reported in Table 5.2 were conducted in this study. Cycle A and B in Table 5.2 were performed up to 55 cycles, with the first 11 cycles being a simple 3-step without the light reflux step. At the twelfth cycle, the configuration was switched to the Skarstrom cycle and the transient product concentration and axial temperature profiles were monitored in order to ensure cyclic steady-state has been reached. The effect of two different durations of the light reflux step ( $t_{LR}$ ) on O<sub>2</sub> purity was investigated while the other operating conditions were kept constant between the two experiments. As it is summarized in Table 5.2, experimental O<sub>2</sub> purity was closely predicted by the model for experiment B. However for experiment A, a difference of 0.8% in the purity values was observed. This was believed to be due to the limitations in the current experimental apparatus design such as the manual switching, single-column experiments, and air-operated vacuum pump. For instance, although the single-column design assisted in mimicking the two-column Skarstrom configuration, but it caused an uncertainty in the O<sub>2</sub> concentration filling the reflux tank. Once the product stream was directed to the tank during the adsorption step as shown in Figure 4.2, since the tank was already under vacuum from the previous light reflux step in the prior cycle, a sudden drop in the pressure ( $\sim 10$  kPa) inside the adsorption column was noticed due to the pressure equilibration between the column and the tank. This might possibly result in a decrease in the purity of the O<sub>2</sub> heading to the reflux tank, i.e. later used during the LR step, and might effect the O<sub>2</sub> purity in the product. However, it should be noted that the high purities obtained using the simple Skarstrom cycle verified the capability

of Ag-ETS-10 for high-purity O<sub>2</sub> production in a single-stage process. It is also worth noting that calculating the experimental recovery of the cycles was not possible because the outlet flow rates were over the measurement range of the flow meter at the exit of the column.

Figure 5.2(a) shows the transient experimental O<sub>2</sub> purity in the product stream for experiment A and the predictions from the model. The points on this figure corresponds to the purity of the stream leaving the adsorption step in each of the 55 cycles. Figure 5.2(c) shows the O<sub>2</sub> purity in the product with more focus on the high-purity range. Figures 5.2(a) and (c) indicate that except the first initial cycles, the model was able to predict the transient trend of O<sub>2</sub> purity in the product. The discrepancy in the initial cycles might be due to the atmospheric air already present in the tubings and valves since the mass spectrometer detected N<sub>2</sub> presence in the stream for the first few cycles. Experimental temperature profiles were also fairly well described by the simulations as shown in Figure 5.2(b) and (d). Conducting rapid VSA cycles were limited in this study due to the manual switching of the valves and the power of the vacuum pump used for the evacuation step. In order to evacuate the column used in this study with the air-driven pump, minimum time of the evacuation step had to be 60 seconds which limited the implementation of rapid cycles. More experiments with a stronger vacuum pump, two adsorption columns, and shorter adsorption times should be conducted in order to further explore the possibility of high-purity O<sub>2</sub> production in a single-stage process.

Table 5.2: Operating conditions for the experimental cycle demonstrations.

Cycle	$t_{\text{ADS}}$ [s]	$t_{\text{EVAC}}$ [s]	$t_{\text{FP}}$ [s]	$t_{\text{LR}}$ [s]	$F_{\text{ADS}}$ [ccm]	$P_{\text{L}}$ [kPa]	$Pu_{\text{O}_2}^{\text{exp}}$ [%]	$Pu_{\text{O}_2}^{\text{sim}}$ [%]
A: Skarstrom	20	60	90	15	900	14	98.6±0.2	99.4
B: Skarstrom	20	60	90	8	900	14	97.2±0.2	97.4

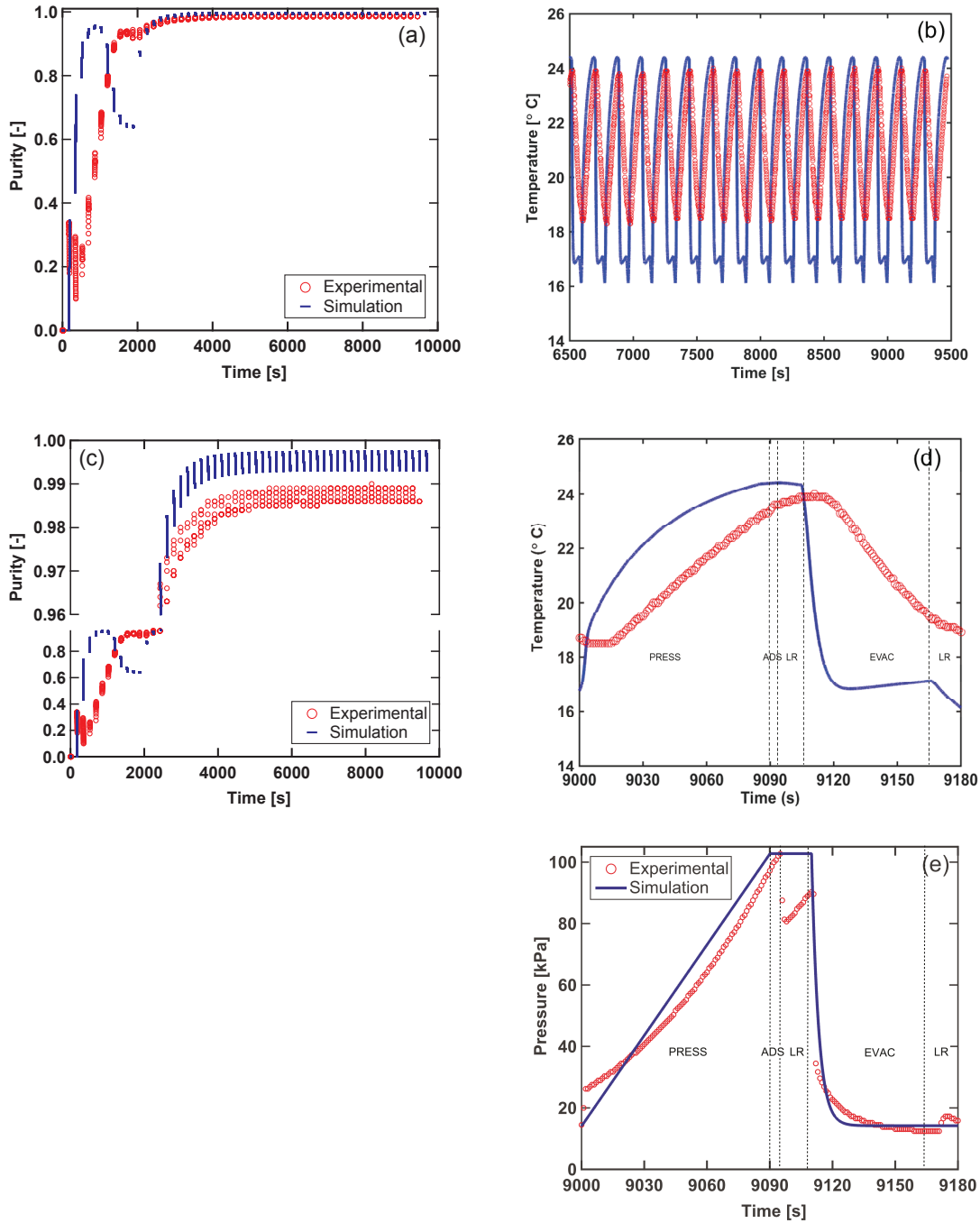


Figure 5.2: Skarstrom VSA cycle experiments. Symbols are experimental values and lines correspond to simulation. (a) transient product purity during the adsorption steps; (b) axial temperature profile for thermocouple located at 8 cm from the column inlet; (c) transient product purity during the adsorption steps with focus on high-purity range; (d) axial temperature profile for thermocouple located at 8 cm from the column inlet for one cycle at cyclic steady state; (e) Experimental and simulated pressure profile.

## Purity-recovery optimization

As stated in the introduction, in this study a dry air feed (78.0% N<sub>2</sub>, 21.0% O<sub>2</sub>, 1.0% Ar) was introduced to the column and the operating conditions were optimized for higher purities and recoveries. The bounds for the decision variables are listed in Table 5.3. Bed length was fixed at 0.32 *m* similar to the column available in our laboratory and  $P_H$  was fixed at 100 kPa. Two cycle configurations, the Skarstrom and the 6-step with PE and HPP were considered for the single-stage O<sub>2</sub> purifications. Purity and recovery of the Skarstrom cycle is defined as:

$$Pu_{O_2} = \frac{n_{O_2}^{ADS\ out} - n_{O_2}^{LR\ in}}{n_{total}^{ADS\ out} - n_{total}^{LR\ in}} \quad (5.1)$$

$$Re_{O_2} = \frac{n_{O_2}^{ADS\ out} - n_{O_2}^{LR\ in}}{n_{O_2}^{ADS\ in} + n_{O_2}^{FP\ in}}$$

where  $n$  is the number of moles collected during the corresponding step. Figure 5.3 shows the purity recovery Pareto front for the Skarstrom cycle which indicates 99.5% O<sub>2</sub> purity can be obtained at 11.7% recovery. This shows the ability of Ag-ETS-10 to produce high-purity O<sub>2</sub> from air in one stage due to its higher Ar/O<sub>2</sub> selectivity compared to other selective sorbents. However, it should be noted that according to Figure 5.3, it is not possible to obtain ultra high-purity O<sub>2</sub> ( $Pu_{O_2} > 99.9\%$ ) with the Skarstrom cycle. As presented in Chapter 4, the 6-step VSA cycle with PE and HPP improved O<sub>2</sub> recovery since part of the stream leaving the evacuation step is refluxed to the column to pressurize the column. This cycle showed a promising O<sub>2</sub> recovery of 91.7% for a 99.5% O<sub>2</sub> purity for a feed stream containing 95% O<sub>2</sub>/5% Ar. In this study, a single-stage O<sub>2</sub> purification using the same cycle was studied. The decision variables and their bounds are shown in Table 5.3. In order to calculate the intermediate pressure  $P_1$ , the amount of mass leaving the donor column during the PE step should be the same as the amount introduced to the receiver column. This value depends on the  $P_L$  and the ratio of  $\theta = \frac{t_{HPP}}{t_{ADS}}$  chosen by the optimizer. To satisfy this condition,  $P_1$  was calculated prior to each cycle simulation by a 3-dimensional interpolation based on the values of  $P_L$  and  $\theta$  chosen by the optimizer for every set of decision variables. The 3-dimensional space was created prior to starting the

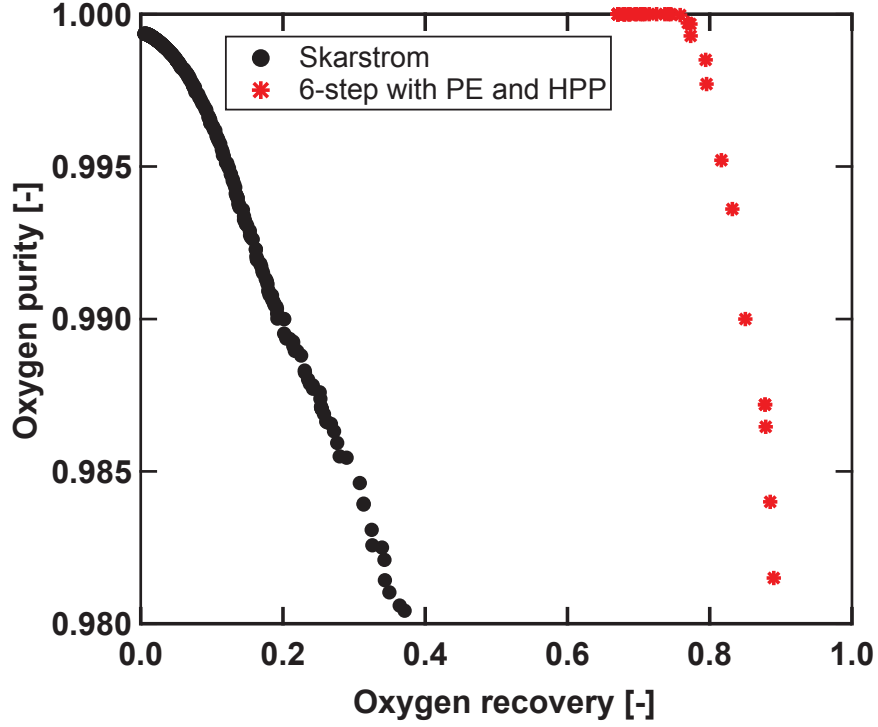


Figure 5.3: Results of process optimization to maximize O<sub>2</sub> purity and recovery for 6-step cycle with PE and HPP VSA and dry air feed.

optimization. Oxygen purity and recovery in this cycle were calculated as the following:

$$Pu_{O_2} = \frac{n_{O_2}^{ADS \text{ out}}}{n_{total}^{ADS \text{ out}}} \quad (5.2)$$

$$Re_{O_2} = \frac{n_{O_2}^{ADS \text{ out}}}{n_{O_2}^{ADS \text{ in}}}$$

Table 5.3: Range of decision variables used in VSA cycle purity-recovery and energy-productivity optimizations.

Decision variable	Range
$t_{ADS}$ [s]	2 – 10
$t_{EVAC}$ [s]	2 – 10
$t_{LR}$ [s]*	2 – 10
$t_{HPP}$ [s]**	0.02 – 9.9
$v_{ADS}$ [m s <sup>-1</sup> ]	0.005 – 0.2
$P_L$ [kPa]	3.0 – 60.0

\* Skarstrom and 6-step with PE and LPP

\*\* 6-step with PE and HPP

The HPP step was followed with a feed pressurization step if the pressure in the column did not reach  $P_H$  during the HPP step and the  $O_2$  introduced to the column during this step should be also added to the denominator of the definition of recovery in Eq. 5.2. Figure 5.3 shows the purity-recovery Pareto curve obtained for this cycle. As it can be observed, purity values in excess of 99.5% and 99.8% can be achieved at a recovery of 82.0% and 79.5%, respectively. To our knowledge, this is the highest value of recovery reported in literature for  $O_2$  product with purity of 99.5% using a single-stage equilibrium-based VSA cycle with dry air as the feed. It is worth mentioning that for on-site applications, similar to the ones for 99.5%  $O_2$ , equipment size is an important design parameter and although the feed for this separation, i.e. atmospheric air, is abundant, higher value of recovery reduces the size of the unit. In addition to this, other impurities in the air such as  $CO_2$  and  $H_2O$  should be also removed prior to  $O_2$  purification unit and the higher the recovery of the unit, the lesser energy is consumed to remove the impurities. Energy-productivity optimization with  $O_2$  purity constraint of 99.5% for this cycle is discussed in detail in the following section.

### Energy-productivity optimization

A second set of optimizations were conducted on the operating conditions to minimize total energy consumption and maximize the productivity of the cycles. These optimizations were used to compare different possible approaches to purify  $O_2$ . The range of decision variables used were similar to the purity-recovery optimizations reported in Table 5.3. Oxygen purity constraint of 99.5%  $O_2$  was implemented by introducing a penalty function. Productivity is defined as the total tonnes of  $O_2$  in the product stream divided by the volume of adsorbent per day:

$$Pr = \frac{\text{Total tonnes of } O_2 \text{ in the raffinate product}}{(\text{Total volume of Ag} - \text{ETS} - 10)(\text{Cycle time})} \quad (5.3)$$

Total energy consumption for one cycle is calculated depending on the type of steps in each cycle and is reported in terms of kilowatt hours per tonne of  $O_2$  produced per cycle. Similar approach to the one in Chapter 4 was used in this study to calculate total energy consumption in each of the cycles discussed above and is summarized in Table 5.4.

A rigorous optimization was conducted to minimize the total energy consumption and maximize  $O_2$  in the single-stage Skarstrom and 6-step with PE and HPP cycles and the energy-productivity Pareto fronts are shown in Figure 5.4(d). This figure indicates

that the single-stage 6-step cycle with PE and HPP showed a significantly lower energy consumption for the same level of O<sub>2</sub> productivity compared to the single-stage Skarstrom cycle. As it was explained earlier, this configuration enhances O<sub>2</sub> recovery since part of the extract product is used to pressurize the column and saves power with the addition of the pressure equalization (PE) step. These results were compared with the dual-stage configurations and is discussed in the next section.

Table 5.4: Equations used for the calculation of total energy consumption in the VSA cycles.

Adsorption step	$E_{\text{ADS}} = \frac{1}{\eta} \epsilon \pi r_{\text{in}}^2 \frac{\gamma}{\gamma - 1} \int_{t=0}^{t=t_{\text{ADS}}} v_{\text{ADS}} P(t) \left[ \left( \frac{P(t)}{P_{\text{feed}}} \right)^{\frac{\gamma-1}{\gamma}} - 1 \right] dt$	(5.4)
Evacuation and light reflux steps	$E_{\text{step}} = \frac{1}{\eta} \epsilon \pi r_{\text{in}}^2 \frac{\gamma}{\gamma - 1} \int_{t=0}^{t=t_{\text{step}}} v(t) P(t) \left[ \left( \frac{P_{\text{atm}}}{P(t)} \right)^{\frac{\gamma-1}{\gamma}} - 1 \right] dt$	(5.5)
Skarstrom and 6-step with PE and LPP cycles	$E_{\text{T}} = \frac{E_{\text{ADS}} + E_{\text{EVAC}} + E_{\text{LR}}}{\text{Total tonnes of O}_2 \text{ in the raffinate product}}$	(5.6)
6-step with PE and HPP cycle	$E_{\text{T}} = \frac{E_{\text{ADS}} + E_{\text{EVAC}}}{\text{Total tonnes of O}_2 \text{ in the raffinate product}}$	(5.7)

### 5.3.2 Dual-stage production of high-purity oxygen

The possibility of producing high-purity O<sub>2</sub> in a dual-stage process was also studied in this work. In this approach, as shown in Figure 5.1(b), air feed undergoes a N<sub>2</sub> removal stage (stage 1) where the majority of nitrogen is captured from the air. The product stream, which is rich in Ar and O<sub>2</sub> is introduced to the O<sub>2</sub> purification stage (stage 2) to reach the desired purity of O<sub>2</sub>. In this section, each of these two stages were optimized independently and were later combined using an analytical approach to calculate the overall performance indicators of the process. The results are later compared with the performance of the single-stage processes described earlier.

#### Optimization of nitrogen removal stage

The approach discussed in section 5.2.2 was used to conduct the energy-productivity optimization for the N<sub>2</sub> removal stage using the Skarstrom cycle with zeolite 5A. The values of total energy consumption  $En_1$ , and productivity  $Pr_1$  of this stage will be later used for the overall energy-productivity calculation. The maximum O<sub>2</sub> purity that can be obtained from dry air using zeolite 5A is 95.0% since zeolite 5A has no selectivity for Ar/O<sub>2</sub>. In addition to the product containing 95.0% O<sub>2</sub>/5.0% Ar, three product streams with different nitrogen content varied between 30.0% to 70.0% and the rest balanced with O<sub>2</sub> and Ar were considered in the optimization. The ratio of  $\frac{y_{\text{O}_2}}{y_{\text{Ar}}}$  was kept equal to 21.0 (i.e. same ratio of O<sub>2</sub>/Ar in air) for all the product streams. Each of these four

$N_2$  purity concentrations in the product stream was set as a constraint for the simulation and the corresponding energy-productivity Pareto curves were obtained by optimizing the operating parameters within the bounds shown in Table 4.2 and the results are shown in Figure 5.4(a). This figure indicates total energy consumption of the  $N_2$  stage ( $En_1$ ) increases while the productivity ( $Pr_1$ ) drops by tightening the purity constraint on the  $N_2$  content in the product stream of this stage, i.e. smaller  $N_2$  concentration. The product of this stage is directed to the  $O_2$  purification stage discussed in the next section.

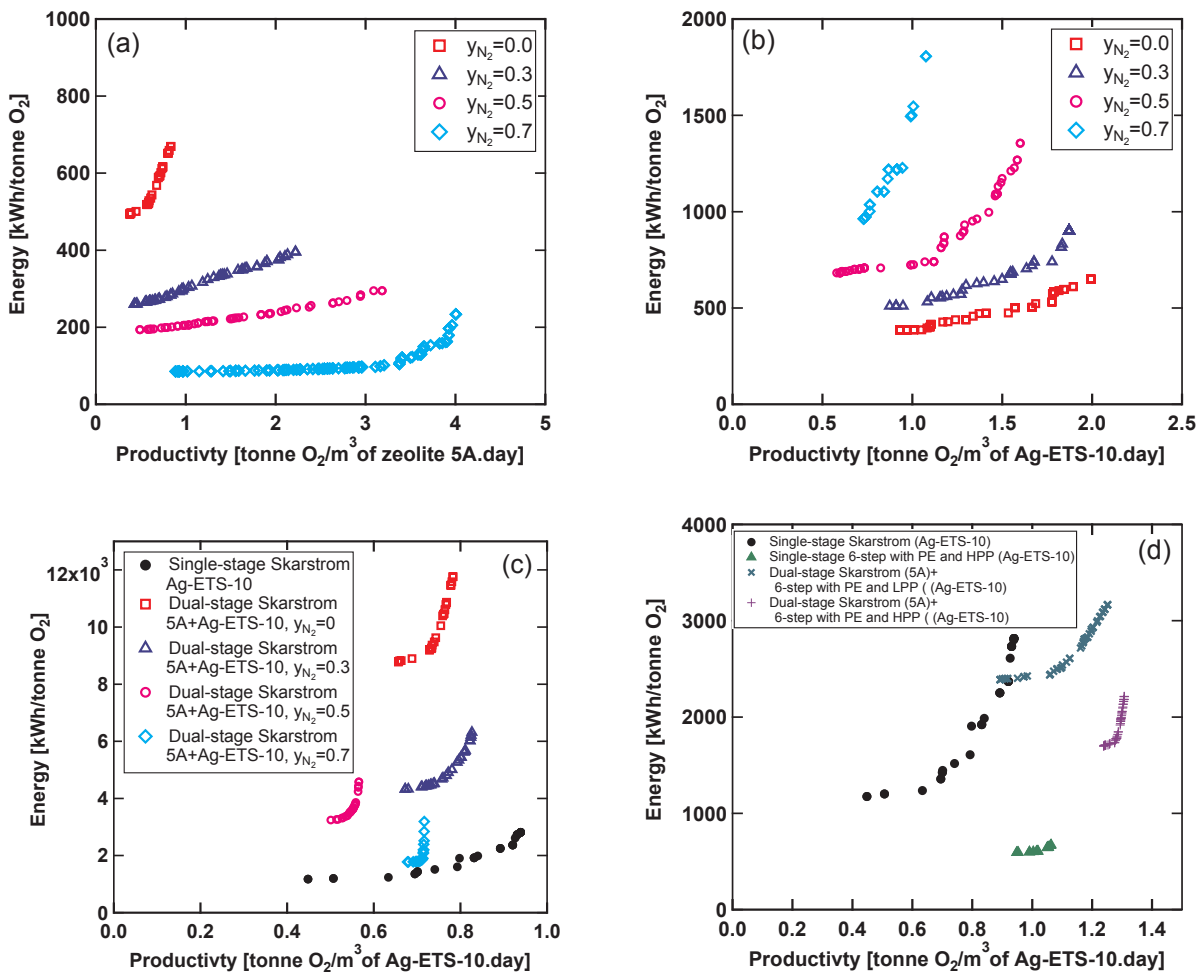


Figure 5.4: Results of process optimization to maximize  $O_2$  productivity and minimize energy consumption for dry air feed delivering 99.5%  $O_2$  product. (a) first stage: Skarstrom cycle with zeolite 5A delivering product with different levels of  $N_2$  content; (b) second stage: Skarstrom cycle with Ag-ETS-10 with different levels of  $N_2$  content in the feed; (c) comparison of multiple dual-stage  $O_2$  purification approaches with the single-stage Skarstrom. Volume of adsorbent in the productivity values for the dual-stage configurations is the cost normalized volume of Ag-ETS-10; (d) comparison of four possible cycle designs for  $O_2$  purification.

## Optimization of oxygen purification stage

Similar to the previous section, in addition to the feed containing 95.0% O<sub>2</sub>/5.0% Ar, four feed streams with different nitrogen content varied between 30.0% to 78.0% (i.e.  $y_{N_2}$  in the air, already presented in section 5.3.1) and the rest balanced with O<sub>2</sub> and Ar were introduced to the column. These concentrations were identical to the ones presented in Figure 5.4(a). Each of these five different feed compositions were set as an input for the simulation and the corresponding purity-recovery Pareto curves were obtained by optimizing the operating parameters within the bounds shown in Table 4.2. The Pareto curves for purity-recovery optimization are shown in Figure 5.5. Interestingly, it can be observed that except for the ultra high-purity region ( $Pu_{O_2} > 99.9\%$ ), the recovery of O<sub>2</sub> in the product stream for a particular value of oxygen purity increases with an increase in the N<sub>2</sub> content in the feed stream. For instance, O<sub>2</sub> recovery for a raffinate stream containing 99.5% O<sub>2</sub> reaches 11.7% when air (78.0% N<sub>2</sub>) is fed into the column during the adsorption step compared to 7.0% recovery when the feed contains no N<sub>2</sub>. This effect can be further explained by comparing the axial concentration profiles of N<sub>2</sub> and O<sub>2</sub> for the conditions at which a purity of 99.5% is achieved, as shown in Figure 5.6. In this figure, gas phase axial concentration profiles of N<sub>2</sub> at the end of the evacuation step at cyclic steady state normalized against  $y_{N_2}$  in the feed, and O<sub>2</sub> solid phase axial concentration profiles for the same step is plotted for three different compositions of N<sub>2</sub> in the feed. As it can be observed in Figure 5.6(a), increasing N<sub>2</sub> content in the feed stream saturates the feed end of the column with nitrogen since it is the heavier component, and N<sub>2</sub> front moves further towards the product end for higher values of  $y_{N_2}$  in the feed. This results in pushing the O<sub>2</sub> front to the product end and avoids losing O<sub>2</sub> during the evacuation step. This effect is clearly visible in Figure 5.6(b) and can explain the improvement in O<sub>2</sub> recovery for higher N<sub>2</sub> content as discussed earlier in Figure 5.5. However, additional N<sub>2</sub> content in the feed stream results in higher energy consumption during the evacuation step and lower oxygen productivity for that cycle. Hence, a detailed comparison should be made in order to compare a single-stage with a two-stage oxygen separation process. This effect is extensively discussed in the next section.

Similar approach to the one for the first stage was applied for the energy-productivity optimization of the second stage, i.e. O<sub>2</sub> purification using the Skarstrom cycle with Ag-ETS-10, and the results are shown in Figure 5.4(b). The purity constraint in the product stream for this set of optimization was 99.5% O<sub>2</sub> and multiple feed streams with N<sub>2</sub> concentrations, similar to those reported in Figures 5.5 and 5.4(a), were introduced to the second stage. As it can be observed from Figure 5.4(b), to obtain 99.5% O<sub>2</sub> in the product, more energy ( $En_2$ ) was required to purify a feed containing more N<sub>2</sub>. However,

the productivity of the second stage ( $Pr_2$ ) stays within the same range in spite of  $N_2$  concentration level in the feed stream (product of the first stage). The results presented in Figures 5.4(a) and (b) were combined using an analytical approach to calculate the overall energy-productivity values and are further discussed in the next section.

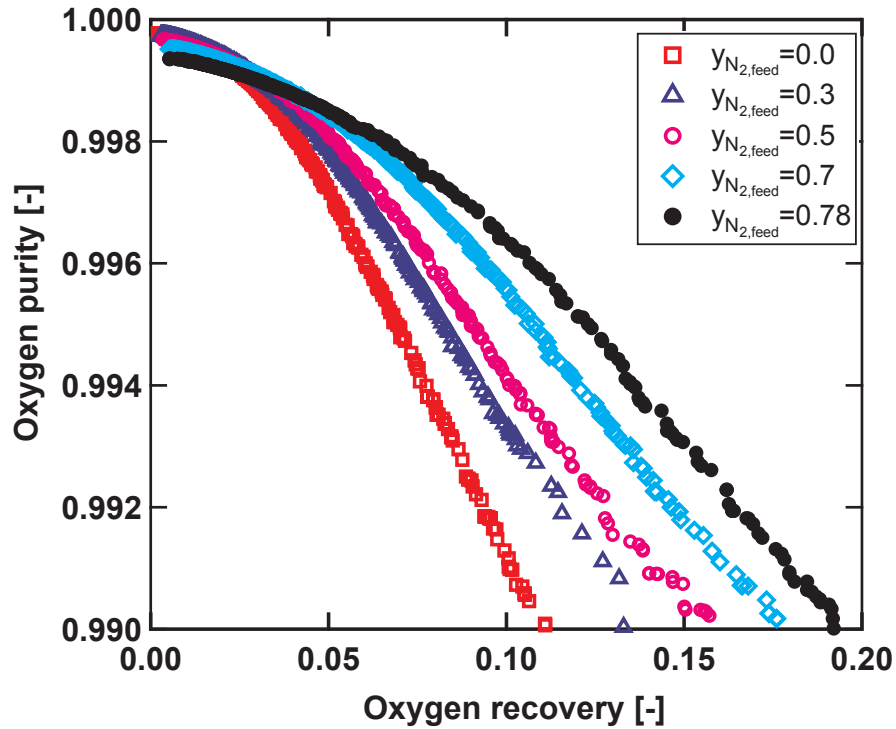


Figure 5.5: Results of process optimization to maximize  $O_2$  purity and recovery for Skarstrom VSA cycle with different  $N_2$  content in the feed.

### Optimal design

An analytical approach was used in order to calculate the overall productivity and total energy consumption of the dual-stage separation processes introduced in the previous sections. Productivity is defined as the total tonnes of  $O_2$  in the product stream divided by the total volume of adsorbent per day. Therefore, overall productivity for a dual-stage process can be calculated as:

$$Pr_{\text{total}} = \frac{Pr_2}{1 + \frac{Pr_2 \alpha}{Pr_1 Re_2}} \quad (5.8)$$

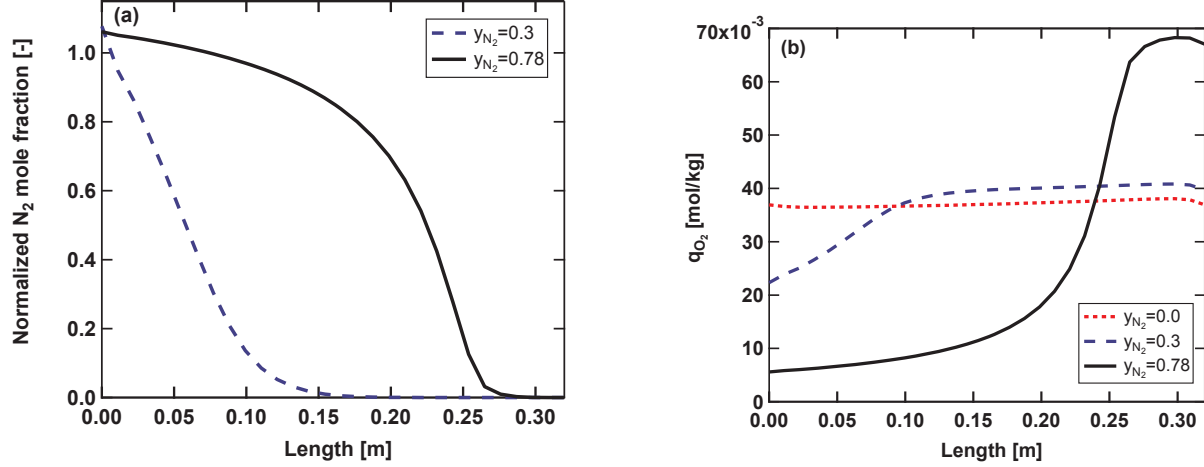


Figure 5.6: Effect of N<sub>2</sub> content in the feed on the concentration profiles: (a) Normalized N<sub>2</sub> gas phase axial concentration profiles of the Evacuation step (normalized against  $y_{N_2}$  in the feed); (b) O<sub>2</sub> solid phase axial concentration profiles of the Evacuation step in the Skarstrom cycle.

where 1 and 2 correspond to the first and second stages, respectively. Since productivity is defined per unit volume of the adsorbent and different materials were used in each of the two stages, volume of the sorbent used in the first stage was correlated to the volume of the sorbent used in the second stage through parameter  $\alpha$ . This constant is defined as the ratio of the cost of unit volume of the sorbent used in the first stage (N<sub>2</sub> removal) over the cost of unit volume of the material used in the second stage (O<sub>2</sub> purification). This assisted in normalizing the volumes based on the price of the adsorbent in the market and offered a proxy for the capital cost involved using different configurations. In this study,  $\alpha$  for zeolite 5A over Ag-ETS-10 was considered to be equal to 0.05 based on the prices available in the market [74]. Therefore, all the overall productivity values reported are in tonne of O<sub>2</sub> produced per cost normalized volume (CNV) of Ag-ETS-10 per day.

Total energy consumption is reported in terms of kilowatt hours per tonne of O<sub>2</sub> produced per cycle. Hence, overall energy consumption of a dual-stage process is defined as:

$$En_{\text{total}} = \frac{En_1}{Re_2} + En_2 \quad (5.9)$$

where  $En_1$  and  $En_2$  correspond to the total energy consumption of the first and the second stage, respectively. It is worth noting from Eqs. 5.8 and 5.9 that the recovery of the second stage plays an important role in the overall productivity and total energy consumption. In other words, the higher the recovery of the second stage, the lesser energy should be

spent in the first stage since the product of the  $N_2$  removal stage is introduced to the  $O_2$  purification stage.

The method introduced through Eqs. 5.8 and 5.9 was used to calculate the overall productivity and energy consumption of the process by combining the values in Figures 5.4(a) and (b). The values used for  $En_2$  and  $Pr_2$  in Eqs. 5.8 and 5.9 correspond to the points with lowest energy consumption in Figure 5.4(b). Figure 5.4(c) shows the overall energy-productivity fronts for different concentrations of  $N_2$  entering the second stage and the comparison with the single-stage Skarstrom  $O_2$  purification with dry air as the feed discussed in section 5.3.1. This figure clearly presents the advantage of the single-stage process over the dual-stage options in terms of total energy consumption. Overall energy consumption decreases by increasing the  $N_2$  content in the middle product stream from the nitrogen removal stage. According to Eq. 5.9, this could be due to the low  $O_2$  recovery in the Skarstrom cycle and therefore, it was concluded that there was no advantage in using the Skarstrom cycle configuration for the  $O_2$  purification stage in a dual-stage process.

As discussed in the previous chapter, the 6-step with PE and LPP and the 6-step with PE and HPP cycles could deliver 99.5%  $O_2$  at 27.3% and 91.7% recovery, respectively and considering these two cycles as the second stage might be more beneficial compared to the Skarstrom cycle. It is worth noting that since recovery was not imposed as a constraint for the energy-purity optimizations, the points on the energy-productivity Pareto fronts do not necessarily have the same recovery as the ones on the purity-recovery Pareto fronts. However, the chances of achieving a higher recovery in the energy-productivity optimization for a cycle which performed better in the purity-recovery optimization, is still higher. Therefore, the possibility of using the other two 6-step cycles was investigated through Eqs. 5.8 and 5.9 and the results are shown in Figure 5.4(d). The points with the lowest energy consumption reported in Figure 4.10(d) were used for  $Pr_2$  and  $En_2$  and the values for the Skarstrom cycle delivering 95.0%  $O_2$  and 5.0% Ar with zeolite 5A was considered for  $Pr_1$  and  $En_1$  in Eqs. 5.8 and 5.9.

Figure 5.4(d) indicates that compared to the single-stage Skarstrom design, higher productivity was obtained at the same level of energy consumption using the 6-step with PE and LPP or the 6-step with PE and HPP cycles. The energy consumption was lower for the 6-step cycle with PE and HPP which was predominantly due to higher recoveries achieved in this configuration according to Eq.5.9. As it can be observed, the single-stage  $O_2$  purification using the 6-step cycle with PE and HPP presents a better performance compared to the other approaches with significantly lower energy consumption for the same range of productivity. The final comparison between the four possible approaches presented in Figure 5.4(d) was to conduct a graphical scheduling for the optimal points

on the energy-productivity Pareto fronts and is discussed in the next section.

### 5.3.3 Cycle scheduling

PSA scheduling is an important step for practical implementation of various cycle configurations and it becomes complicated to ensure the continuity of the feed stream due to the many constraints of the cycle configurations. In this study, the strategy employed to optimize the cycles in the energy-productivity optimizations, does not necessarily link up into a continuous process and idle times should be added between various stages to achieve a continuous process. It is also impractical to have too many beds to achieve a continuous cycle for an on-site oxygen purification unit. Therefore, the scheduling of the stages should be performed such that the optimal idle time and minimum number of columns are obtained. In addition to the stated limitations, the other challenge is to find the best position to add the idle times. Given the wide range of operating conditions and the constraints mentioned above, it is necessary to develop a standard method for scheduling of the cycles to ensure all the constraints are met.

For the cycle configurations that were discussed in this study, more constraints should be considered, such as the pressure equalization donor and receiver beds must align and the light reflux (LR) step should start while the adsorption (ADS) step is happening in another column. A simple algorithm was written based on the graphical methodology proposed by Mehrotra et al [75] and programmed with all such constraints as an inputs. The optimal operating times of the steps for the points on Figure 5.4 were introduced to the algorithm. This program added idle times at certain positions in-between the steps to make the cycle continuous while also keeping the idle times small. The operating conditions with the shortest idle times for the least number of beds is then chosen for the scheduling and is shown in Figures 5.7 and 5.8.

Scheduling the optimized Skarstrom cycles, reported in Figure 5.4, for both zeolite 5A and Ag-ETS-10 were performed with the two constraints of having a continuous feed and the alignment of the adsorption and the light reflux steps. The idle times were added between the evacuation and light reflux steps to meet the latter constraint. The Skarstrom configuration with the least number of beds is shown in Figure 5.8(a) and Figure 5.7(a) for zeolite 5A and Ag-ETS-10, respectively. The duration of the adsorption steps are shown on the top left hand side of the figures. As it can be seen, a minimum of four columns are required to achieve a continuous process for both. However, the configuration in Figure 5.8(a) (zeolite 5A) should be followed by a second stage to purify O<sub>2</sub> to 99.5% whereas the configuration in Figure 5.7(a) is a single-stage process using Ag-ETS-10. As discussed earlier, two other cycles, the 6-step with PE and LPP and the 6-step with PE and HPP

were considered for the O<sub>2</sub> purification stage in the dual-stage process. The points with the lowest energy consumption reported in Figure 4.10(d) were used for the scheduling of these two cycles because according to Eqs. 5.8 and 5.9, these points offer the lowest energy consumption for the two stages together. Scheduling of the 6-step cycle with PE and LPP was done similarly with the constraints mentioned for the Skarstrom cycle plus the full alignment of the pressure equalizations donor (PE-D) and receiver (PE-R) columns. The light product pressurization steps (LPP) was implemented so that it always started after the LR step while aligned with the adsorption step. The idle times were added in-between the LR step and the PE to achieve the aforementioned goals. Figure 5.8(b) shows the corresponding results for this cycle. This figure indicates four columns of Ag-ETS-10 are required in addition to the four columns of zeolite 5A in the first step shown in Figure 5.8(a). Scheduling of the 6-step cycle with PE and HPP, was performed such that the heavy product pressurization step was aligned with the evacuation step in addition to the constraint for the PE-D and PE-R steps. The corresponding configuration is shown in Figure 5.8(c) and Figure 5.7(b) for the dual-stage and single-stage configurations, respectively. As observed, only three columns with a very short idle time are required when the 6-step cycle with PE and HPP is used for the O<sub>2</sub> purification stage. This is in addition to the four columns of zeolite 5A required for the N<sub>2</sub> removal stage as shown in Figure 5.8(a) and further verifies the advantage of this cycle over the 6-step cycle with PE and LPP (Figure 5.8(b)). According to Figure 5.7(b), minimum eight columns are required for a continuous single-stage O<sub>2</sub> purification to 99.5% using the 6-step cycle with PE and HPP. This might add complication in terms of performing an on-site O<sub>2</sub> purification from air due to the more number of column required in this cycle compared the four column single-stage Skarstrom cycle shown in Figure 5.7(a). However, as discussed earlier, higher O<sub>2</sub> recoveries can be obtained using the 6-step cycle with PE and HPP with lower total energy consumption. More detailed optimization taking into account the scheduling and the minimum number of columns can also assist in better identifying the optimal design.

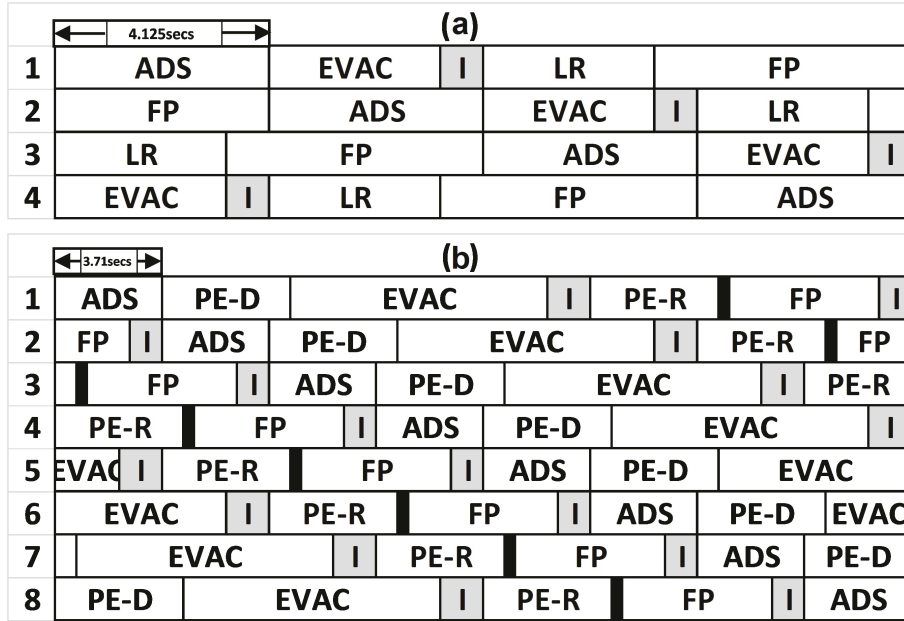


Figure 5.7: Cycle scheduling for the optimal operating conditions. Idle times are shown in gray blocks: (a) single-stage Skarstrom cycle using Ag-ETS-10 for O<sub>2</sub> purification. (b) single-stage 6-step cycle with PE and HPP using Ag-ETS-10 for O<sub>2</sub> purification. The black blocks indicate the HPP step.

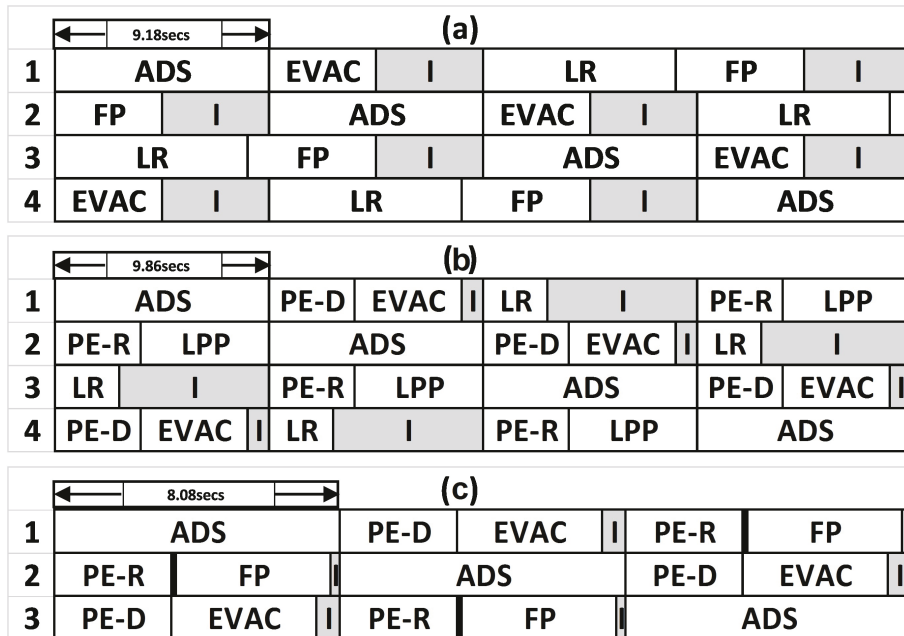


Figure 5.8: Cycle scheduling for the optimal operating conditions. Idle times are shown in gray blocks: (a) Skarstrom cycle using zeolite 5A for N<sub>2</sub> removal (stage 1). (b) 6-step cycle with PE and LPP using Ag-ETS-10 for O<sub>2</sub> purification (stage 2)(c) 6-step cycle with PE and HPP using Ag-ETS-10 for O<sub>2</sub> purification (stage 2). The black blocks indicate the HPP step.

## 5.4 Conclusions

In this study, the possibility of producing O<sub>2</sub> with 99.5% purity from dry air in a single-stage VSA cycle was explored. Simple single-column Skarstrom cycle experiments were performed and O<sub>2</sub> with purity of 98.6% was obtained from a dry air feed stream. Although the purity values were lower than the model predictions, possibly due to the experimental limitations in this study, the high purities obtained using the simple Skarstrom cycle verified the capability of Ag-ETS-10 for high-purity O<sub>2</sub> production in a single-stage process. The effect of N<sub>2</sub> content in the feed on the product purity and recovery was studied and it was concluded that increasing N<sub>2</sub> content in the feed stream saturates the feed end of the column with nitrogen. This results in pushing the O<sub>2</sub> front to the product end and avoids losing O<sub>2</sub> during the evacuation step. Thus, O<sub>2</sub> recovery was slightly higher when N<sub>2</sub> concentration in the feed was larger. The simulations predicted 82.0% recovery for a product with 99.5% O<sub>2</sub> purity for a 6-step cycle with PE and HPP and dry air feed stream which verified the advantage of this cycle over the other possible designs.

The second set of optimizations were conducted in order to minimize total energy consumption and maximize overall productivity of multiple single-stage and dual-stage O<sub>2</sub> purification approaches. A detailed comparison was performed between a group of cycles with zeolite 5A as the adsorbent used for N<sub>2</sub> removal stage while delivering various levels of N<sub>2</sub> concentration in the product. This product stream was later fed to the O<sub>2</sub> purification stage where Ag-ETS-10 was used and the energy-productivity optimization results were compared with the single-stage Skarstrom cycle using Ag-ETS-10. The comparison presented no advantage in performing a dual-stage O<sub>2</sub> purification when the Skarstrom cycle was used for both of the stages. However, using the 6-step cycle with PE and LPP or the 6-step cycle with PE and HPP for the O<sub>2</sub> purification stage showed a higher productivity compared to the single-stage Skarstrom cycle. A rigorous energy-productivity optimization was conducted for the single-stage O<sub>2</sub> purification using the 6-step cycle with PE and HPP and it was concluded that this approach presents a better performance compared to the other cycle configurations with significantly lower energy consumption for the same values of productivity. A simple graphical scheduling was also conducted for the optimal points for the better performing designs. The minimum number of columns required for a continuous process was 4 for the single-stage Skarstrom and 8 for the single-stage 6-step cycle with PE and HPP. This value was 8 (i.e. 4+4) for a dual-stage process with the Skarstrom cycle for the N<sub>2</sub> removal stage plus the 6-step cycle with PE and LPP for the O<sub>2</sub> purification stage. When the 6-step cycle with PE and HPP was used as the second stage, the minimum number of columns were 7 (i.e. 4+3).

# Chapter 6

## Concluding remarks

### 6.1 Conclusions

In this thesis, the capability of silver-exchanged titanosilicates (Ag-ETS-10) for high-purity O<sub>2</sub> production was investigated through material characterization, detailed dynamic lab-scale experiments, process modeling and simulation, process optimization, and experimental validation of vacuum swing adsorption (VSA) cycles. Despite the challenges in O<sub>2</sub> purification, such as the similar boiling points and molecular sizes of O<sub>2</sub> and Ar, Ag-ETS-10 has shown the capability to separate these two components based on their thermodynamics affinities. Since O<sub>2</sub> is the lightest component on this material, i.e. with the lowest adsorption affinity, Ag-ETS-10 has a great potential for high-purity O<sub>2</sub> production with the current adsorption technologies available and possibly with newly designed adsorption cycle configurations. The main objective of this study was to evaluate this potential at larger scales and design adsorption processes with optimized operating parameters in order to improve performance indicators such as O<sub>2</sub> purity and recovery, O<sub>2</sub> productivity and total energy consumption of the cycles. To achieve this goal, a reliable lab-scale adsorption apparatus, a generic mathematical model that includes all possible transport effects, and a powerful optimization toolbox, all of which was developed as a part of this study, was required.

In the first chapter, an introduction on the current technologies available for high-purity O<sub>2</sub> production was provided. Basics of adsorption separation processes was elaborated and an overview on the simulation and optimization of pressure swing adsorption (PSA) processes and the objectives of this thesis were provided. In Chapter 2, low-pressure adsorption isotherms of N<sub>2</sub>, O<sub>2</sub>, and Ar on Ag-ETS-10 extrudates at 303.15 K, 323.15 K, and 343.15 K were obtained and fitted to single-site Langmuir model. Experimental

breakthrough profiles of various gas mixtures were measured using a laboratory scale dynamic column breakthrough apparatus, constructed as a part of this study, to validate the large-scale performance of the adsorbent. These profiles were modeled by writing detailed mass and energy balances and solve the resulting partial differential equations using finite volume technique. The model was able to predict experimental profiles of mole fraction and temperature well. Binary equilibrium of Ar/O<sub>2</sub> was also well predicted by single-site extended Langmuir model. The validated model was later extended to develop the simple Skarstrom vacuum swing adsorption cycle to further explore the capability of Ag-ETS-10 for high-purity O<sub>2</sub> production from a feed containing 95% O<sub>2</sub>/5% Ar. A parametric study on the effect of the low pressure  $P_L$  on the cycle performance suggested multi-objective optimization of the cycle to satisfy objective functions. This cycle was optimized and purity-recovery Pareto curves were obtained by using genetic algorithm. The results verifies the ability of Ag-ETS-10 to produce high-purity O<sub>2</sub> in excess of 99.0% with recovery of 11.35% using the simple Skarstrom VSA cycle.

In Chapter 3, high-pressure adsorption isotherms of N<sub>2</sub>, O<sub>2</sub>, and Ar on Ag-ETS-10 at 303.15 K, 323.15 K, and 343.15 K were obtained and fitted to dual-site Langmuir model. The effects of flow rate, temperature, pressure, and particle size on the breakthrough profiles of N<sub>2</sub>, O<sub>2</sub>, and Ar and their mixtures on Ag-ETS-10 extrudates and granules were investigated using the laboratory scale dynamic column breakthrough apparatus. The model developed earlier was used to predict the experimental temperature and concentration profiles. Using fundamentals of fluid dynamics and mass transfer, it was concluded that the sharper profiles obtained at higher inlet velocities were likely due the change in the hydrodynamics of the system (i.e. larger Peclet numbers) rather than external film resistance. The effect of temperature on the breakthrough profiles was also studied and the result indicated that the shape of the concentration fronts were governed by the equilibrium rather than mass transfer effects. The same conclusion was reached by exploring the effect of pressure on N<sub>2</sub> breakthrough profiles. In a separate attempt, N<sub>2</sub> concentration profiles on two columns filled with Ag-ETS-10 extrudates and granules with two different sizes were obtained. Although a minor effect of particle size was observed, it was concluded that mass transfer through Ag-ETS-10 particle is less likely to dominate the separation process and Ag-ETS-10 has the potential for high-purity O<sub>2</sub> production at larger scales under rapid adsorption cycles since mass transfer resistance is almost negligible.

The experiments in Chapter 2 and 3 verified large-scale performance of Ag-ETS-10 as well as the model developed to describe experiments. In Chapter 4, this model was extended to simulate multiple vacuum swing adsorption (VSA) cycle configurations for high-purity O<sub>2</sub> production and optimize them to maximize O<sub>2</sub> purity and recovery. A mixture of

95.0%/5.0% O<sub>2</sub>/Ar feed was considered for the Skarstrom cycle. Experimental 3-step and Skarstrom cycle demonstrations were conducted to verify the simulations. Both experimental purity and recovery plus the axial temperature profiles were well predicted by the model. Considering bed length as the decision variable for the optimizations demonstrated an enhanced recovery of 11.1% for a product stream with 99.5% O<sub>2</sub> purity. In a separate attempt, pressure swing adsorption (PSA) and pressure-vacuum swing adsorption (PVSA) Skarstrom cycles were also studied in addition to VSA cycle and it was concluded that VSA has a better performance compared to the other two cycles. Two more advance cycles, a 6-step with pressure equalization (PE) and light product pressurization (LPP) steps, and a 6-step with pressure equalization (PE) and heavy product pressurization (HPP) steps, were also considered in this chapter to improve the recovery of the cycle. For the 6-step with PE and LPP, the recovery of O<sub>2</sub> obtained in the product stream for a purity of 99.5% was 27.3%. This value was significantly improved to 91.7% for a 6-step with PE and HPP. To our knowledge, this is the highest reported value of recovery for this level of O<sub>2</sub> purity using an equilibrium-based adsorption process. The second set of optimizations were conducted to maximize productivity of O<sub>2</sub> and minimize total energy consumption of the VSA cycles. Three different purity constraints were imposed and the Pareto curves were obtained for various cycles. A significant improvement in the performance indicators was obtained through process optimization for the two 6-step cycles.

Although Ag-ETS-10 was well characterized and new cycles with enhanced performance indicators were developed and optimized in Chapters 2 to 4, the separation process was further explored from a broader perspective in Chapter 5. In this chapter, the possibility of producing O<sub>2</sub> with 99.5% purity from dry air in a single-stage VSA cycle was explored. Simple single-column Skarstrom cycle experiments were performed and O<sub>2</sub> with purity of 98.6% was obtained from a dry air feed stream. Although the purity values were lower than the model predictions, which was possibly due to the experimental limitations in this study, the high purities obtained using the simple Skarstrom cycle verified the capability of Ag-ETS-10 for high-purity O<sub>2</sub> production in a single-stage process. The effect of N<sub>2</sub> content in the feed on the product purity and recovery was studied and it was concluded that increasing N<sub>2</sub> content in the feed stream saturates the feed end of the column with nitrogen. When considering bed length as one of the decision variables in the purity-recovery optimization, a higher recovery was obtained for a product with 99.5% O<sub>2</sub> purity compared to the case when bed length was a fixed value. The simulations predicted 82.0% recovery for a product with 99.5% O<sub>2</sub> purity for a 6-step cycle with PE and HPP and dry air feed stream which verified the advantage of this cycle over the other possible designs. The second set of optimizations were conducted in order to minimize

total energy consumption and maximize overall productivity of multiple single-stage and dual-stage O<sub>2</sub> purification approaches. A detailed comparison was performed between a group of cycles with zeolite 5A as the adsorbent used for N<sub>2</sub> removal stage while delivering various levels of N<sub>2</sub> concentration in the product. This product stream was later fed to the O<sub>2</sub> purification stage where Ag-ETS-10 was used and the energy-productivity optimization results were compared with the single-stage Skarstrom cycle using Ag-ETS-10. The comparison presented no advantage in performing a dual-stage O<sub>2</sub> purification when the Skarstrom cycle was used for both of the stages. However, using the 6-step cycle with PE and LPP or the 6-step cycle with PE and HPP for the O<sub>2</sub> purification stage showed a higher productivity compared to the single-stage Skarstrom cycle. At the end, a rigorous energy-productivity optimization was conducted for the single-stage O<sub>2</sub> purification using the 6-step cycle with PE and HPP and it was concluded that this approach presents a better performance compared to the other cycle configurations with significantly lower energy consumption for the same values of productivity. A simple graphical scheduling was also conducted for the optimal points for the better performing designs. The minimum number of columns required for a continuous process was 4 for the single-stage Skarstrom and 8 for the single-stage 6-step cycle with PE and HPP. This value was 8 (i.e. 4+4) for the dual-stage process with the Skarstrom cycle for the N<sub>2</sub> removal stage plus the 6-step cycle with PE and LPP for the O<sub>2</sub> purification stage. When the 6-step cycle with PE and HPP was used as the second stage, the minimum number of columns were 7 (i.e. 4+3).

## 6.2 Outlook

This work has provided a detailed insight of O<sub>2</sub> purification using Ag-ETS-10 from material characterization to large-scale performance validation and process simulation and optimization. As per characterization, both low-pressure and high-pressure isotherm measurements were reported and later used as an input to the model. This model was validated through dynamic column breakthrough experiments and suggested the extended Langmuir model as the appropriate model to describe the competition between N<sub>2</sub>, O<sub>2</sub>, and Ar. However, obtaining binary and ternary adsorption isotherms through an independent technique such as the gravimetric method is worth studying. This can be used to further verify the credibility of the extended Langmuir model at a broader range of operating conditions which were beyond the limit of the current dynamic column breakthrough apparatus.

The other possible study on the characterization of Ag-ETS-10 could be obtaining single-component and binary adsorption isotherms for a pre-exchanged Na-ETS-10 batch and

repeating the same measurements for the same silver-exchanged batch (Ag-ETS-10). Investigating properties such as the isosteric heat of adsorption for each of the components and the competition between the components for the two cases may potentially provide feedback for the synthesis step and open the path to achieve higher equilibrium selectivities for Ar over O<sub>2</sub>. It is worth mentioning the even a small improvement in the selectivity can have a significant positive effect on the performance indicators.

Investigating the possibility of using layered bed for single-stage O<sub>2</sub> purification from air is worth studying to further explore the cycles proposed in the area of process simulation of this thesis. In this approach, N<sub>2</sub> will be removed in the first layer of the bed using a common air separation adsorbent and O<sub>2</sub> will be purified in the second layer of the bed using Ag-ETS-10. In addition to N<sub>2</sub>, impurities in air such as water and CO<sub>2</sub> can be also removed prior to O<sub>2</sub> purification in a layered bed approach. To simulate this configuration, one needs to define new boundary conditions and develop an optimal approach to link the two layers of the bed in the model.

In this study, experimental VSA cycle performance of Ag-ETS-10 was verified for the simple 3-step and the Skarstrom cycles. The other two cycles, the 6-step with PE and LPP and the 6-step with PE and HPP, were not explored experimentally. In addition to this, rapid VSA cycles were not studied due to the limitations in the current apparatus such as the manual switching and the air-driven pump used for the evacuation steps. Further studies, requires the modification of the current experimental apparatus in order to include a second adsorption column, automation of the valve switchings between different steps in the cycles, and implementation of a stronger vacuum pump. This can be considered as a potential extension of this thesis to experimentally verify the significant improvements obtained through the process simulation and optimization in this study.

The other possible extension of this work could be a detailed cost analysis based on the energy-productivity optimization results provided in this study. To achieve this, one needs to implement the cycle scheduling technique proposed in Chapter 5 along with other typical economic analysis approaches available or by manipulating the objective functions in the optimization routine in order to include cost of producing high-purity O<sub>2</sub> in addition to the other constraints.

# Bibliography

- [1] D. Ferreira, M. Boaventura, P. Barcia, R. D. Whitley, and A. Mendes, “Two-stage vacuum pressure swing adsorption using AgLiLSX zeolite for producing 99.5+% oxygen from air,” *Ind. Eng. Chem. Res.*, vol. 55, no. 3, pp. 722–736, 2016.
- [2] R. T. Yang, *Gas separation by adsorption processes*. Series on chemical engineering: v. 1, London: Imperial College Press, 1997.
- [3] D. M. Ruthven, S. Farooq, and K. S. Knaebel, *Pressure swing adsorption*. New York, N.Y.: VCH Publishers, 1994.
- [4] “Public health parts 1 to 399,” tech. rep., Office of the Federal Register USA, 2010.
- [5] European Industrial Gases Association Homepage. <http://www.eiga.eu>, (accessed March 2016).
- [6] “Performance specification, oxygen, aviator’s breathing, liquid and gas,” Tech. Rep. MIL-PRF-27210H, Department of Defense USA, 2009.
- [7] T. L. Reynolds, D. B. Bailey, D. F. Lewinski, C. M. Roseburg, and B. Palaszewski, “Onboard inert gas generation system/onboard oxygen gas generation system (obiggs/obogs) study. part 1; aircraft system requirements,” tech. rep., Boeing Commercial Airplane Group, Seattle, WA United States, 2001.
- [8] J. G. Jee, M. B. Kim, and C. H. Lee, “Pressure swing adsorption processes to purify oxygen using a carbon molecular sieve,” *Chem. Eng. Sci.*, vol. 60, no. 3, pp. 869 – 882, 2005.
- [9] R. Kumar, “Vacuum swing adsorption process for oxygen production-a historical perspective,” *Sep. Sci. Technol.*, vol. 31, no. 7, pp. 877–893, 1996.
- [10] S. U. Rege and R. T. Yang, “Kinetic separation of oxygen and argon using molecular sieve carbon,” *Adsorption*, vol. 6, no. 1, pp. 15–22, 2000.
- [11] T. R. Gaffney, “Porous solids for air separation,” *Curr. Opin. Solid State Mater. Sci.*, vol. 1, no. 1, pp. 69 – 75, 1996.
- [12] D. W. Breck, *Zeolite molecular sieves: structure, chemistry, and use*. Wiley-Interscience Publication, New York: Wiley, 1973.
- [13] C. G. Coe and S. M. Kuznicki, “Polyvalent ion exchanged adsorbent for air separation,” Nov. 6 1984. US Patent 4,481,018.
- [14] C. G. Coe, J. F. Kirner, R. Pierantozzi, and T. R. White, “Nitrogen adsorption with a Ca and/or Sr exchanged lithium X-zeolite,” Oct. 6 1992. US Patent 5,152,813.
- [15] C. G. Coe, J. E. Macdougall, and S. J. Weigel, “Magnesium A-zeolite for nitrogen adsorption,” July 20 1994. EP Patent App. EP19,940,100,112.

- [16] C. R. Reid, I. P. O’koy, and K. M. Thomas, “Adsorption of gases on carbon molecular sieves used for air separation. spherical adsorptives as probes for kinetic selectivity,” *Langmuir*, vol. 14, no. 9, pp. 2415–2425, 1998.
- [17] X. Jin, A. Malek, and S. Farooq, “Production of argon from an oxygenargon mixture by pressure swing adsorption,” *Ind. Eng. Chem. Res.*, vol. 45, no. 16, pp. 5775–5787, 2006.
- [18] R. Afonso, A. Mendes, and L. Gales, “Hydrophobic dipeptide crystals: A promising ag-free class of ultramicroporous materials showing argon/oxygen adsorption selectivity,” *Phys. Chem. Chem. Phys.*, vol. 16, no. 36, pp. 19386–19393, 2014.
- [19] J. Sebastian and R. V. Jasra, “Sorption of nitrogen, oxygen, and argon in silver-exchanged zeolites,” *Ind. Eng. Chem. Res.*, vol. 44, no. 21, pp. 8014–8024, 2005.
- [20] D. Ferreira, R. Magalhes, J. Bessa, P. Taveira, J. Sousa, R. D. Whitley, and A. Mendes, “Study of AgLiLSX for single-stage high-purity oxygen production,” *Ind. Eng. Chem. Res.*, vol. 53, no. 40, pp. 15508–15516, 2014.
- [21] A. Anson, S. M. Kuznicki, T. Kuznicki, T. Haastrup, Y. Wang, C. C. Lin, J. A. Sawada, E. M. Eyring, and D. Hunter, “Adsorption of argon, oxygen, and nitrogen on silver exchanged ETS-10 molecular sieve,” *Micropor. Mesopor. Mater.*, vol. 109, no. 13, pp. 577 – 580, 2008.
- [22] M. Shi, J. Kim, J. A. Sawada, J. Lam, S. Sarabadan, T. M. Kuznicki, and S. M. Kuznicki, “Production of argon free oxygen by adsorptive air separation on Ag-ETS-10,” *AIChE J.*, vol. 59, no. 3, pp. 982–987, 2013.
- [23] K. S. Knaebel and A. I. Kandybin, “Pressure swing adsorption system to purify oxygen,” July 13 1993. US Patent 5,226,933.
- [24] N. D. Hutson, S. U. Rege, and R. T. Yang, “Mixed cation zeolites:  $\text{Li}_x\text{Ag}_y - \text{X}$  as a superior adsorbent for air separation,” *AIChE J.*, vol. 45, no. 4, pp. 724–734, 1999.
- [25] A. I. Kandybin, R. A. Anderson, and D. L. Reichley, “System for separation of oxygen from argon/oxygen mixture,” Nov. 28 1995. US Patent 5,470,378.
- [26] J. C. Santos, P. Cruz, T. Regala, F. D. Magalhes, and A. Mendes, “High-purity oxygen production by pressure swing adsorption,” *Ind. Eng. Chem. Res.*, vol. 46, no. 2, pp. 591–599, 2007.
- [27] R. L. Chiang, R. D. Whitley, J. E. Ostroski, and D. P. Dee, “Argon/oxygen selective X-zeolite,” Aug. 13 2002. US Patent 6,432,170.
- [28] S. Sircar, “Preparation of high purity oxygen,” July 12 1988. US Patent 4,756,723.
- [29] J. G. Jee, S. J. Lee, M. B. Kim, and C. H. L. Lee, “Three-bed pvsas process for high-purity  $\text{O}_2$  generation from ambient air,” *AIChE J.*, vol. 51, no. 11, pp. 2988–2999, 2005.
- [30] D. P. Dee, R. L. Chiang, E. J. Miller, and R. D. Whitley, “High purity oxygen production by pressure swing adsorption,” Apr. 8 2003. US Patent 6,544,318.
- [31] D. Ferreira, P. Barcia, R. D. Whitley, and A. Mendes, “Single-stage vacuum pressure swing adsorption for producing high-purity oxygen from air,” *Ind. Eng. Chem. Res.*, vol. 54, no. 39, pp. 9591–9604, 2015.
- [32] D. Ruthven, *Principles of Adsorption and Adsorption Processes*. A Wiley-Interscience publication, Wiley, 1984.

- [33] Y. Belmabkhout, M. Frre, and G. D. Weireld, “High-pressure adsorption measurements. a comparative study of the volumetric and gravimetric methods,” *Meas. Sci. Technol.*, vol. 15, no. 5, p. 848, 2004.
- [34] O. Talu, “Needs, status, techniques and problems with binary gas adsorption experiments,” *Adv. Colloid Interface Sci.*, vol. 7677, pp. 227 – 269, 1998.
- [35] M. Eic and D. M. Ruthven, “A new experimental technique for measurement of intracrystalline diffusivity,” *Zeolites*, vol. 8, no. 1, pp. 40 – 45, 1988.
- [36] D. Do, *Adsorption Analysis: Equilibria and Kinetics*. Chemical Engineer Series, Volume 2, Imperial College Press, 1998.
- [37] R. T. Yang, *Adsorbents: fundamentals and applications*. Hoboken, N.J.: Wiley-Interscience, 2003.
- [38] C. Skarstrom, “Method and apparatus for fractionating gaseous mixtures by adsorption,” Jul. 1960. US Patent 2944627.
- [39] N. H. Berlin, “Method for providing an oxygen-enriched environment,” Oct. 25 1966. US Patent 3,280,536.
- [40] A. Rajagopalan, A. Avila, and A. Rajendran, “Do adsorbent screening metrics predict process performance? a process optimisation based study for post-combustion capture of CO<sub>2</sub>,” *Int. J. Greenhouse Gas Control*, vol. 46, pp. 76–85, 2016.
- [41] K. S. Knaebel and F. B. Hill, “Pressure swing adsorption: Development of an equilibrium theory for gas separations,” *Chem. Eng. Sci.*, vol. 40, no. 12, pp. 2351 – 2360, 1985.
- [42] B. Maring and P. Webley, “A new simplified pressure/vacuum swing adsorption model for rapid adsorbent screening for CO<sub>2</sub> capture applications,” *Int. J. Greenhouse Gas Control*, vol. 15, pp. 16–31, 2013.
- [43] I. Langmuir, “The constitution and fundamental properties of solids and liquids. part i. solids,” *J. Am. Chem. Soc.*, vol. 38, no. 11, pp. 2221–2295, 1916.
- [44] S. J. Doong and R. T. Yang, “Bidisperse pore diffusion model for zeolite pressure swing adsorption,” *AIChE J.*, vol. 33, no. 6, pp. 1045–1049, 1987.
- [45] S. Farooq and D. Ruthven, “A comparison of linear driving force and pore diffusion models for a pressure swing adsorption bulk separation process,” *Chem. Eng. Sci.*, vol. 45, no. 1, pp. 107 – 115, 1990.
- [46] O. J. Smith and A. W. Westerberg, “The optimal design of pressure swing adsorption systems,” *Chem. Eng. Sci.*, vol. 46, no. 12, pp. 2967 – 2976, 1991.
- [47] S. Nilchan and C. Pantelides, “On the optimisation of periodic adsorption processes,” *Adsorption*, vol. 4, no. 2, pp. 113–147, 1998.
- [48] D. Ko, R. Siriwardane, and L. T. Biegler, “Optimization of pressure swing adsorption and fractionated vacuum pressure swing adsorption processes for CO<sub>2</sub> capture,” *Ind. Eng. Chem. Res.*, vol. 44, no. 21, pp. 8084–8094, 2005.
- [49] A. Agarwal, L. T. Biegler, and S. E. Zitney, “Superstructure-based optimal synthesis of pressure swing adsorption cycles for precombustion CO<sub>2</sub> capture,” *Ind. Eng. Chem. Res.*, vol. 49, no. 11, pp. 5066–5079, 2010.
- [50] M. M. F. Hasan, R. C. Baliban, J. A. Elia, and C. A. Floudas, “Modeling, simulation, and optimization of postcombustion CO<sub>2</sub> capture for variable feed concentration and

- flow rate. 2. pressure swing adsorption and vacuum swing adsorption processes,” *Ind. Eng. Chem. Res.*, vol. 51, no. 48, pp. 15665–15682, 2012.
- [51] K. Deb, A. Pratap, S. Agarwal, and T. Meyarivan, “A fast and elitist multiobjective genetic algorithm: NSGA-II,” *IEEE Trans. Evol. Comput.*, vol. 6, pp. 182–197, Apr 2002.
- [52] S. Krishnamurthy, V. Rao, S. Guntuka, P. Sharratt, R. Haghpanah, A. Rajendran, M. Amanullah, I. Karimi, and S. Farooq, “CO<sub>2</sub> capture from dry flue gas by vacuum swing adsorption: A pilot plant study,” *AIChE J.*, vol. 60, no. 5, pp. 1830–1842, 2014.
- [53] Y. Wang, B. Helvensteijn, N. Nizamidin, A. M. Erion, L. A. Steiner, L. M. Mulloth, B. Luna, and M. D. LeVan, “High pressure excess isotherms for adsorption of oxygen and nitrogen in zeolites,” *Langmuir*, vol. 27, no. 17, pp. 10648–10656, 2011.
- [54] Onsite Oxygen & Nitrogen Gas Generators OXYMAT Homepage. <http://www.oxymat.com>, (accessed March 2016).
- [55] S. M. Kuznicki, “Large-pored crystalline titanium molecular sieve zeolites,” Aug. 1 1989. US Patent 4,853,202.
- [56] A. Rajendran, V. Kariwala, and S. Farooq, “Correction procedures for extra-column effects in dynamic column breakthrough experiments,” *Chem. Eng. Sci.*, vol. 63, no. 10, pp. 2696 – 2706, 2008.
- [57] R. B. Bird, W. E. Stewart, and E. N. Lightfoot, *Transport Phenomena*. Wiley International edition, New York: Wiley, 2007.
- [58] R. Haghpanah, A. Majumder, R. Nilam, A. Rajendran, S. Farooq, I. A. Karimi, and M. Amanullah, “Multiobjective optimization of a four-step adsorption process for postcombustion CO<sub>2</sub> capture via finite volume simulation,” *Ind. Eng. Chem. Res.*, vol. 52, no. 11, pp. 4249–4265, 2013.
- [59] S. Guntuka, S. Farooq, and A. Rajendran, “A- and b-site substituted lanthanum cobaltite perovskite as high temperature oxygen sorbent. 2. column dynamics study,” *Ind. Eng. Chem. Res.*, vol. 47, no. 1, pp. 163–170, 2008.
- [60] D. Green and R. Perry, *Perry’s Chemical Engineers’ Handbook, Eighth Edition*. McGraw Hill professional, McGraw-Hill Education, 2007.
- [61] J. M. Pinheiro, A. A. Valente, S. Salstio, N. Ferreira, J. Rocha, and C. M. Silva, “Application of the novel ets-10/water pair in cyclic adsorption heating processes: Measurement of equilibrium and kinetics properties and simulation studies,” *Appl. Therm. Eng.*, vol. 87, pp. 412 – 423, 2015.
- [62] M. Mazzotti and A. Rajendran, “Equilibrium theory - based analysis of nonlinear waves in separation processes,” *Annu. Rev. Chem. Biomol. Eng.*, vol. 4, pp. 119–141, 2013.
- [63] R. Haghpanah, R. Nilam, A. Rajendran, S. Farooq, and I. Karimi, “Cycle synthesis and optimization of a vsa process for postcombustion CO<sub>2</sub> capture,” *AIChE J.*, vol. 59, no. 12, pp. 4735–4748, 2013.
- [64] V. R. Rao and S. Farooq, “Experimental study of a pulsed-pressure-swing-adsorption process with very small 5A zeolite particles for oxygen enrichment,” *Ind. Eng. Chem. Res.*, vol. 53, no. 33, pp. 13157–13170, 2014.
- [65] S. W. Chai, *Experimental Simulation of Rapid Pressure Swing Adsorption for Medical Oxygen Concentrator and Numerical Simulation of the Critical Desorption-by-Purge Step*. PhD thesis, Lehigh University, 2011.

- [66] S. Hosseinzadeh Hejazi, A. Rajendran, J. Sawada, and S. Kuznicki, "Dynamic column breakthrough and process studies of high-purity oxygen production using silver-exchanged titanosilicates," *Ind. Eng. Chem. Res.*, vol. 55, no. 20, pp. 5993–6005, 2016.
- [67] R. R. Vemula, M. V. Kothare, and S. Sircar, "Lumped heat and mass transfer coefficient for simulation of a pressure swing adsorption process," *Sep. Sci. Technol.*, vol. 0, no. 0, pp. 1–7, 0.
- [68] J. C. Knox, A. D. Ebner, M. D. LeVan, R. F. Coker, and J. A. Ritter, "Limitations of breakthrough curve analysis in fixed-bed adsorption," *Ind. Eng. Chem. Res.*, vol. 55, no. 16, pp. 4734–4748, 2016.
- [69] R. R. Vemula, M. V. Kothare, and S. Sircar, "Anatomy of a rapid pressure swing adsorption process performance," *AIChE J.*, vol. 61, no. 6, pp. 2008–2015, 2015.
- [70] N. Wakao and T. Funazkri, "Effect of fluid dispersion coefficients on particle-to-fluid mass transfer coefficients in packed beds: Correlation of sherwood numbers," *Chem. Eng. Sci.*, vol. 33, no. 10, pp. 1375 – 1384, 1978.
- [71] M. Giese, K. Rottschfer, and D. Vortmeyer, "Measured and modeled superficial flow profiles in packed beds with liquid flow," *AIChE J.*, vol. 44, no. 2, pp. 484–490, 1998.
- [72] E. S. Kikkinides and R. T. Yang, "Simultaneous SO<sub>2</sub>/NO<sub>x</sub> removal and SO<sub>2</sub> recovery from flue gas by pressure swing adsorption," *Ind. Eng. Chem. Res.*, vol. 30, no. 8, pp. 1981–1989, 1991.
- [73] M. Mofarahi, J. Towfighi, and L. Fathi, "Oxygen separation from air by four-bed pressure swing adsorption," *Ind. Eng. Chem. Res.*, vol. 48, no. 11, pp. 5439–5444, 2009.
- [74] Delta Adsorbents Homepage. <http://www.deltaadsorbents.com>, (accessed January 2017).
- [75] A. Mehrotra, A. D. Ebner, and J. A. Ritter, "Simplified graphical approach for complex psa cycle scheduling," *Adsorption*, vol. 17, no. 2, pp. 337–345, 2011.